THERMAL RADIATIVE PROPERTIES OF DISORDERED MEDIA AND DEEP METAL GRATINGS

A Dissertation
Presented to
The Academic Faculty

by

Peiyan Yang

In Partial Fulfillment
of the Requirements for the Degree
Doctor of Philosophy in the
George W. Woodruff School of Mechanical Engineering

Georgia Institute of Technology
August 2019

THERMAL RADIATIVE PROPERTIES OF DISORDERED MEDIA AND DEEP METAL GRATINGS

Approved by:

Dr. Zhuomin Zhang, Advisor
George W. Woodruff School of
Mechanical Engineering
Georgia Institute of Technology

Dr. Peter Hesketh
George W. Woodruff School of
Mechanical Engineering
Georgia Institute of Technology

Dr. Peter Loutzenhiser
George W. Woodruff School of
Mechanical Engineering
Georgia Institute of Technology

Dr. Michael Filler
School of Chemical & Biomolecular
Engineering
Georgia Institute of Technology

Dr. Jud Ready
School of Materials Science &
Engineering
Georgia Institute of Technology

Date Approved: June 13, 2019

To my parents

ACKNOWLEDGEMENTS

I'd like to express my wholehearted thanks to my Ph.D. advisor, Dr. Zhuomin Zhang, for offering me this opportunity to do research under his guidance five years ago. Throughout this journey, he has been a patient, inspiring and insightful advisor, as well as a caring, loving and encouraging mentor. I appreciate all the time, thoughts and passion he has contributed to make my Ph.D. experience productive and stimulating. In addition, I am grateful to Dr. Peter Hesketh, Dr. Peter Loutzenhiser, Dr. Michael Filler and Dr. Jud Ready, for taking the time to serve on my dissertation reading committee and for sharing their breadth of expertise and knowledge. I'd like to thank National Science Foundation and Department of Energy for their funding support.

Sincere appreciation is also expressed to my former and current group members. I would like to thank Dr. Richard Zihao Zhang and Dr. Jesse Watjen for sharing their suggestions and wisdom; Dr. Xiaohu Wu, Dr. Zhaolong Wang, Shiquan Shan, Eric Tervo, Chuyang Chen and Dudong Feng for their help in research and life. Much appreciation goes to Dr. Bo Zhao, Dr. Xianglei Liu and Dr. Qiang Cheng for the fruitful discussions and tutoring during the early stage of my Ph.D. to help transition to the research topic. In particular, I thank Dr. Leonard Hanssen during my internship at National Institute of Standards and Technology (NIST) for his mentorship and sharing expertise in spectroscopy. I'd like to thank to all my friends during my stay in Atlanta for their friendship.

Finally, I wish to express my deepest love and appreciation to my parents for their support and love. Those bedtime stories when I was a kid helped me grow and have brought me where I am now.

TABLE OF CONTENTS

LIST OF TABLES

LIST OF FIGURES

NOMENCLATURE

A	area, m^2
b	trench width, m
C	capacitance, F
c_0	speed of light in vacuum, 299 792 458 $m \cdot s^{-1}$
d	sample thickness, m
E	electric field, $V \cdot m^{-1}$
h	trench depth (grating height), m
H	magnetic field, $A \cdot m^{-1}$
i	$\sqrt{-1}$; order
I	radiance or intensity, $W \cdot m^{-2} \cdot sr^{-1}$
j	order
k	wavevector, m^{-1}
k_0	wavevector in vacuum, m^{-1}
L	inductance, H
l	length, m
g	asymmetry factor
m	order
n	refractive index; order

$\mathbf{n}$	unit vector of the microfacet normal
N	number
p	probability density function
P	power, W
Q	scattering/absorption efficiency
R	(directional-hemispherical) reflectance
Ra	surface roughness, m
R_1	uniform random number from 0 to 1
$\mathbf{s}$	unit directional vector
T	(directional-hemispherical) transmittance; temperature
w	root-mean-square microfacet slope; width, m
x,y,z	spatial coordinates, m
Z	impedance, Ω

Greek symbols

α	absorption coefficient, m^{-1}
γ	scattering rate, rad/s
δ	penetration depth, m
ζ	slope of the microfacet

ε_0	vacuum permittivity, 8.854×10^{-12} F·m^{-1}
ε	dielectric function (relative permittivity)
ε'	real part of relative permittivity
ε''	imaginary part of relative permittivity
θ	incidence/zenith angle, rad
Θ	scattering angle, rad
κ	imaginary part of optical constant
λ	wavelength, m
Λ	grating period, m
μ_0	permeability of vacuum, $4\pi \times 10^{-7}$ H·m^{-1}
ν	wavenumber, cm^{-1}
ρ	reflectivity at the surface
σ	scattering coefficient, m^{-1}
σ_{rms}	root-mean-square surface roughness, m
τ	autocorrelation length, m; optical thickness
ϕ	azimuthal angle, rad; porosity
Φ	scattering phase function
ψ	polarization angle, rad
ω	angular frequency, rad·s^{-1}; solid angle, sr

ω_s	scattering albedo
Ω	solid angle, sr

Subscripts

abs	absorptance
amb	ambient
AM1.5	air mass 1.5
coll	collimated
dd	directional-directional
dh	directional-hemispherical
emi	emittance
ext	extinction
i	incident
max	maximum
MP	magnetic polariton
o	observation
r	reflection
re	re-striking

ref	reference
rms	root mean square
s	surface
sca	scattering
sp	specular
SPP	surface plasma polariton
sum	summation
tot	total
TE	transverse electric
TM	transverse magnetic

ACRONMYS

1D	one dimensional
2D	two dimensional
3D	three dimensional
AD	adding-doubling
BRDF	bidirectional-reflectance distribution function
BTDF	bidirectional-transmittance distribution function
BSSRDF	bidirectional scattering-surface reflectance distribution function
d-d	directional-directional
d-h	directional-hemispherical
DTGS	deuterated triglycine sulfate
EM	electromagnetic
FTIR	Fourier transform infrared spectrometer
GOA	geometric optics approximation
IAD	inverse adding-doubling
LC	inductor-capacitor
MCRT	Monte Carlo ray-tracing
MCT	mercury cadmium telluride, HgCdTe
MIR	mid-infrared
MP	magnetic polariton

MP1	first order of magnetic polariton
MSM	microfacet slope method
NIR	near-infrared
PTFE	polytetrafluoroethylene
RTE	radiative transfer equation
rms	root mean square
SEE	standard error of estimate
SEM	scanning electron microscopy
SPP	surface plasmon polariton
s,*p*	s- or p-polarization
TAAS	three-axis automated scatterometer
TE	transverse electric
TM	transverse magnetic
RCWA	rigorous coupled-wave analysis
WPDF	weighted probability density function

SUMMARY

Controlling thermal radiation is desired for energy harvesting and saving, thermal management and aerospace applications. Thermal radiative properties of materials can be tuned by the surface roughness, volumetric inhomogeneity and periodic micro/nanostructures. The present dissertation investigates the spectral radiative properties of various materials and micro/nanostructures by performing three research tasks. (1) Measurement and investigation of the radiative properties of sintered ceramic plates, modeling the dielectric function and scattering process of the samples; (2) Design, fabrication and measurement of an efficient solar reflector based on a highly scattering thin film atop a sliver film, development of a physical model for simulation of the light transport process; (3) Microfabrication and demonstration of magnetic polaritons (MPs) in deep metallic gratings for tailoring spectral radiative properties.

Radiative properties of dense ceramic Al_2O_3, AlN, and Si_3N_4 plates are investigated from the visible to the mid-infrared region at room temperature. Directional-hemispherical and specular transmittance and reflectance were measured, from which the regions dominated by either volumetric or surface scattering can be distinguished. The scattering and absorption coefficient of Al_2O_3 and AlN are obtained using an inverse method based on the measurement, and also predicted using Mie theory for comparison. The Lorentz oscillator model is applied to fit the reflectance spectra in the phonon vibration bands where scattering is insignificant. The observed phonon modes for Si_3N_4 are much stronger in the polycrystalline sample studied here than in amorphous films.

A diffusive solar reflector with record-high reflectance is presented, consisting of a polytetrafluoroethylene (PTFE) sheet on top of a silver film. This design demonstrates a

weighted solar reflectance of over 0.99, highest value ever reported. The underlying mechanism of the high reflectance is explained by comparing the calculation from a Monte Carlo ray-tracing method and a modified two-flux model with the experiments. In addition, the measurements suggest a high emittance in the mid-infrared region. Therefore, the proposed structure holds promise for passive daytime radiative cooling.

The bidirectional radiative properties of the structure were measured at the wavelength of 635 nm, to understand if the mirror-like reflector at the back of PTFE will alter the diffuse reflecting nature of the material. The Monte Carlo ray-tracing method is modified to incorporate both surface and volumetric scattering of the structure and to elucidate the underlying mechanism. It also provides insights on the critical thickness at which the structure becomes specular.

The excitation of magnetic polaritons is experimentally demonstrated in several microfabricated grating samples by measuring the specular reflectance in the near-to mid-infrared region. The results are compared with the calculation from the rigorous coupled wave analysis and an LC-circuit model. The influence of incidence angle, plane of incidence, polarization, and the trench depth on the spectral reflectance is also investigated. The MP dispersion for off-plane layout has been studied and demonstrated for the first time.

Fundamental knowledge and understanding of the radiative properties of randomly and periodically structured solid materials (including ceramics, polymer and metal) are gained through this theoretical and experimental research. The findings are expected to impact practical applications such as radiometric devices, passive radiative cooling, design of nanostructures for thermal management, waste heat recovery as well as solar energy harvesting.

CHAPTER 1

INTRODUCTION

The ability to tailor optical/radiative properties of materials has attracted tremendous interest from the scientific community, with promising applications in photonic and energy conversion systems, such as thermophotovoltaic (TPV) and solar devices [1-3], cloaking [4], sensing and imaging [5, 6], etc. To engineer materials with desired optical/radiative properties, two main approaches are used. The bottom-up approach focuses on the unique optical response at subwavelength scale: by patterning periodic structures such as one-dimensional (1D) gratings, two-dimensional (2D) nanowires and nanoholes, and three-dimensional (3D) nanodots, the radiative properties of the materials are altered. The top-down approach, on the other hand, examines the correlation of the optical response with its macroscopic properties, such as crystallinity, purity, porosity and surface roughness, etc. This chapter will give the background for the two types of methods and the scenarios in which they are applied.

1.1 Tuning Radiative Properties from Randomness

Thermal radiative properties of materials refer to the reflectance, transmittance and absorptance/emittance. In the simplest case, the reflectance can be calculated as a mirror-like reflection from the interface of two materials based on Fresnel's equation [7], and a certain amount of transmittance is produced when the sample is semitransparent. Based on Kirchhoff's law, spectral-emittance of the material equals to spectral-absorptance, which is obtained by subtracting the reflectance and transmittance from unity. The discussion of thermal radiative properties of materials becomes more involved if inhomogeneity is present, either from surface roughness, porosity or impurity. Their radiative properties are

quite distinct from single crystals and cannot be rigorously predicted due to the stochastic nature of randomness. By embracing this randomness which is prevalent in everyday life and understanding how it can alter the radiative properties, it is possible to find an economically viable and simple way to engineer new materials.

Refractory ceramic materials are widely applied in industry, because they are capable of maintaining physical and chemical stabilities at high temperatures. Thermal radiative properties of them play an important role in performing heat-transfer analysis, temperature measurements, system design and monitoring. It remains a daunting challenge to fully understand and interpret the radiative properties of ceramic materials due to the presence of rough surfaces, porosity, different crystalline structures and impurities. Three dense and relatively pure ceramic plates, Al_2O_3, AlN and Si_3N_4, are characterized and studied in this thesis, from visible to mid-infrared range at room temperature.

The optical properties of crystalline hexagonal α-$A1_2O_3$ have been extensively studied and summarized for both polycrystalline [8] and single crystals considering anisotropy [9]. Several studies have measured or modeled the radiative properties of alumina (ceramic $A1_2O_3$) with different densities and inner porous structures in the near- and mid-infrared regions [10-12]. Some researchers have demonstrated collimated visible light transmission in alumina with high density and purity, and fine grains [13]. Ceramic polycrystalline AlN can be made by tape casting followed by sintering and is a promising substrate material for high-power microelectronics due to its high thermal conductivity, electrical resistance, and mechanical hardness. Due to its wurtzite structure, the AlN crystal is inherently anisotropic and has polarization-dependent vibrational frequencies and dielectric responses in the mid-infrared range [14, 15]. The visible and near-infrared optical

properties of AlN crystals or crystalline thin films have been determined and summarized in Refs. [16, 17]; however, little work has been done on the optical properties of sintered AlN ceramics. Dense Si_3N_4 ceramics have been used in applications such as cutting tools, high-temperature engines, and microelectronic devices. In microelectronic devices and microelectromechanical systems, Si_3N_4 is often made as an amorphous or nanocrystalline film formed by chemical vapor deposition. Therefore, most of the available optical and infrared studies of Si_3N_4 are for amorphous films [18-20]. However, sintered ceramic materials are typically polycrystalline with varying degrees of inhomogeneity, grain size distribution, and surface irregularity. Both the trigonal α-Si_3N_4 and hexagonal β-Si_3N_4 crystalline phases may be present in the hot-pressed ceramic depending on the processing conditions, although the most stable phase is β-Si_3N_4, and at sufficiently high temperatures when a liquid phase is present, the α-phase will transform into the β-phase [21]. As for AlN, very few studies have investigated the optical properties of hot-pressed Si_3N_4 ceramics [22].

It is necessary to know that the discussion in this thesis typically focuses on directional-hemispherical (d-h) properties, meaning the incidence is a collimated beam of radiation from a certain direction, and the reflectance and transmittance are collected hemispherically. Based on d-h properties, hemispherical-hemispherical (h-h) properties can be obtained through integration [7]. In the study of thermal radiative properties, reflectance and transmittance are usually measured and modeled directly, while the absorptance and emittance is calculated based on indirect method from Kirchhoff's law. Due to reciprocity, the emittance obtained from d-h reflectance and transmittance is hemispherical-directional emittance, and equals to d-h absorptance [23]. The d-h

reflectance and transmittance of a material is denoted as R_{dh} and T_{dh}, respectively. The bidirectional (d-d) radiative properties are defined as the hemispherical distribution of the reflectance/transmittance, which helps reveal the specularity of the surface and will be detailed in Chapter 2.

1.2 Tuning Radiative Properties from Periodic Structures

When the feature size of the material is comparable to the wavelength, the radiative properties often possess quite distinctive features. Numerous studies have reported fascinating radiative and optical properties originating from nanostructured materials that could significantly impact areas such as energy harvesting, plasmonic and photonic devices, sensing and imaging, etc. [24]. These artificially structured materials, often referred to as electromagnetic (EM) metamaterials, can manipulate EM wave propagation mostly through various resonance modes or surface waves supported by the micro/nano structure. Among them are surface phonon polaritons (SPhPs), surface plasmon polaritons (SPPs) [24], magnetic polaritons (MPs) [25], hyperbolic modes formed by hyperbolic metamaterials [26] and epsilon-near-zero materials [27]. Meanwhile, non-resonant unique radiative properties can be found in photonic crystals [28] and nanowire arrays [29]. Plasmonic metamaterials refer to those that exploit the coupling of incident photons to plasmons, a collection of oscillation charges, to achieve unique absorption or transmission behavior.

In the aforementioned top-down approach, which tailors the radiative properties by macroscopic features that are much larger than characteristic wavelength, the polarization and phase information of the electromagnetic waves can be neglected. The problem can be described by the radiative transfer equation (RTE), a scalar equation that can be derived

from Maxwell's equations [30]. Modeling the radiative properties of the materials reduces to solving the RTE with proper boundary conditions[23, 31]. Unlike the top-down approach, plasmonic materials exhibits unique radiative properties only when the feature size is comparable to the incident wavelength. Specifically, for thermal radiation which has a typical wavelength of one to a few microns, the feature size must be several microns or below one micron. In this length scale, the polarization and phase properties of the electromagnetic waves becomes crucial, and the wave nature of light is dominant. Maxwell's equations have to be solved to fully consider the vector and polarizations of the electromagnetic waves. Some counterintuitive phenomena happen at this dimension due to the wave nature of light, including negative refraction [32], enhanced absorption of particles [33], photon-tunneling and near-field radiation [7].

SPPs and MPs are the two main types of resonances that involves the coupling of plasmons. SPPs are guided surface waves which travel along a metal-dielectric interface and exponentially decay into both sides of the interface [24]. It involves both the charge motion in the metal and the electromagnetic waves in the dielectric. It typically has subwavelength-scale confinement and intensity enhancement near the interface, which give rises to a variety of applications such as microscopy and subwavelength optics [34], biosensing, nonlinear optics and solar absorption, etc. [2, 24]. MPs are bulk magnetic resonance modes that can be understood from Lenz's law, which states that the induced current from a magnetic field will oppose the change of magnetic flux. At certain frequencies, such interaction becomes resonant and the material exhibits an effective magnetic permeability that can be tuned to a wide range of values not accessible in natural materials [35]. Previously, they have been extensively studied in visible or microwave

wavelength regions. More recently, they are studied in infrared region for coherent thermal emitters [36, 37], extraordinary optical transmission [38, 39] and enhanced absorption when coupled with two-dimensional materials [40]. They have been researched and demonstrated by earlier students in this group [25, 41], and the study will be continued in the thermal radiation range in this thesis, with an emphasize on the experimental demonstration in deep metal gratings.

1.3 Objectives

The objective of this dissertation is to characterize and investigate the thermal radiative properties of selected dispersed medium and periodic nanostructures. For the study of random material, dense ceramic plates and highly scattering polymer sheet are chosen to examine the effect of crystallinity, surface roughness, volumetric scattering, impurity and porosity on their radiative properties. Interpretations are made both qualitatively and quantitatively based on suitable models. The highly scattering polymer sheet is also used to build a highly efficient solar reflector. For the periodic structure, the effect of MPs will be experimentally demonstrated in deep metal gratings for the first time.

The dissertation is organized as follows. Chapter 2 presents the theoretical background and the calculation methods of radiative transfer equation, as well as a review of the concept of magnetic polariton and a semi-analytical solution of the Maxwell's equation adopted in the modeling. Chapter 3 introduces the different optical spectrometers and scatterometers used in this work to measure the radiative properties of the materials, including the principles, usage and limitation. Chapter 4 presents an experimental study of selected thin ceramic plates, and quantitatively interprets their distinctive radiative properties based on volumetric scattering and phonon band structure. Chapter 5 focuses on

the demonstration of a record-high solar reflector based on a dual-layer structure consisting of a highly scattering polymer atop a metal layer. Both the directional-hemispherical and bidirectional radiative properties are measured. This structure also holds promise for radiative cooling applications. The modeling work is introduced in Chapter 6, in which a Monte Carlo method that incorporates both volumetric and surface scattering effects are implemented and the results of which are compared with measurement. The radiative properties of micro-fabricated deep metallic gratings are experimentally investigated in Chapter 7, in which the off-plane dispersion of MP modes is studied for the first time. Finally, Chapter 8 summarizes the major findings and conclusions of this dissertation, then gives suggestions for some future research topics.

CHAPTER 2

THEORETICAL BACKGROUND

This chapter provides the theoretical background for some of the calculation work in the thesis. The radiative transfer equation (RTE) is introduced first, with a focus on its origin and physical interpretation. Then various ways to solve the RTE are briefly introduced. The emphasis will then be put on adding-doubling (AD) method and Mie scattering theory, which helps to predict the scattering and absorption coefficients. Afterwards, the idea and principles of radiative cooling will be covered, with an introduction of several featured research work. The Maxwell's equation solved in periodic structures using rigorous-coupled wave analysis (RCWA) will then be briefly introduced. The resonant modes in metallic gratings will be covered, focusing on the study of magnetic polaritons.

2.1 Light Transport in Dispersed Medium

When the light is incidence on a smooth, semi-infinite or lossy surface, the reflectance is calculated using Fresnel's equation and the angle of reflection equals to the angle of incidence [7]. When the thickness of the substrate is considered, multiple reflections between both surfaces alter the reflectance by either constructive or destructive interference. The interference effect is dropped when the surface is rough, and the diffuse reflectance is present. The specular reflectance is the component at the retroreflection direction while the diffuse component is the component in all other directions. Note that sometimes the specular component has a certain spatial span instead of falling in a cone

with an infinitely small solid angle. When only diffuse component is present and uniform radiance is observed at various observation angles, the surface is called a Lambertian surface [7]. The radiant intensity follows the Lambertian cosine law. A typical diffuse surface is frosted glass, the surface of which is intentionally roughened.

In addition to the surface roughness, the volumetric inhomogeneity can also be a contributor to the diffuse component. Instead of using a clear crystal, when the material is porous or has certain impurities, the contrast of refractive indices leads to electromagnetic waves scattering inside the medium. The magnitude of the scattering depends on the contrast of refractive indices as well as the ratio of the wavelength and characteristic length of the scatterers. Eventually the volumetric scattering leads to a diffuse reflecting surface, such as smart glass made of suspended particles. For light transport in dispersed medium, surface roughness and volumetric inhomogeneity are oftentimes both present, and they are both dealt with in the present work.

To measure the surface characteristics and quantify the diffuse reflectance and transmittance, the bidirectional-reflectance distribution function (BRDF) and bidirectional-transmittance distribution function (BTDF) are defined. It was proposed by Nicodemus et al. [42] for measuring from a surface that was neither completely specular nor perfectly diffuse. Note that a more generic form is the bidirectional scattering distribution function (BSDF), which is the superset of BRDF and BTDF. Another term is bidirectional scattering-surface reflectance distribution function (BSSRDF), which includes subsurface scattering beneath the interface. In this work, the BRDF and BSSRDF is not differentiated.

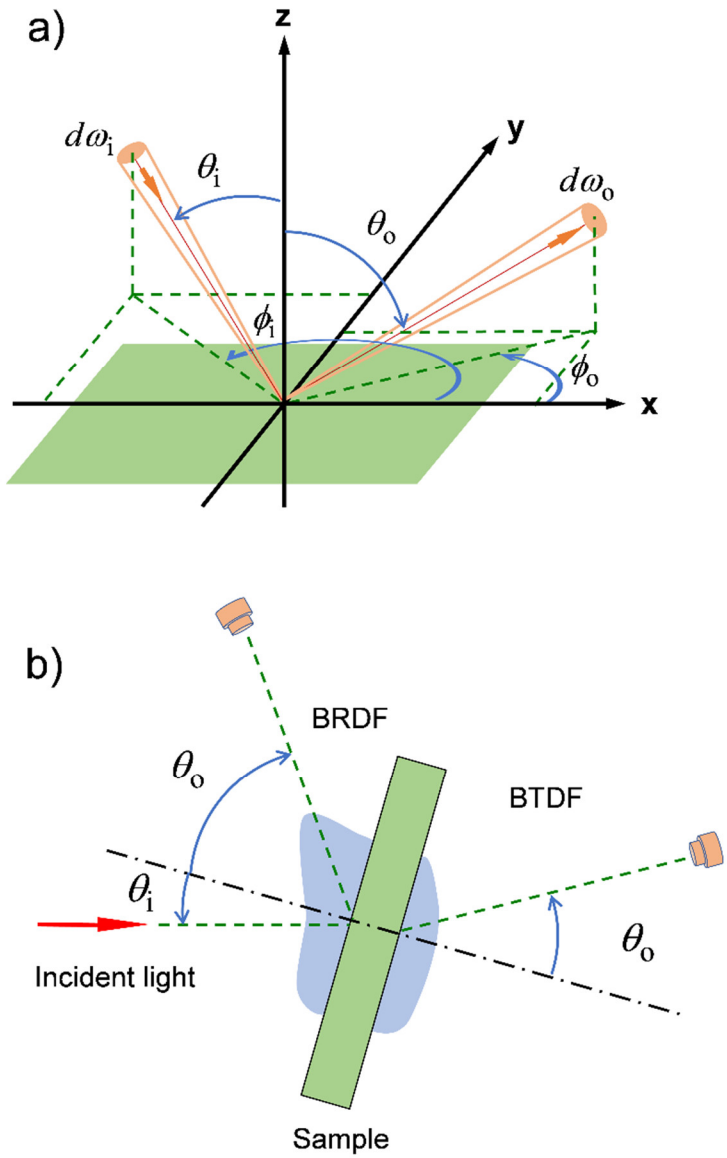

Figure 2.1 Schematic of (a) definition of BRDF and (b) the in-plane BRDF and BTDF measurement setup, the arrows indicate the direction in which these angles increase. Note that the observation angle θ_o is defined separately for BRDF and BTDF. One detector is rotated to capture the signal at various observation angles.

In radiometric terms, BRDF is defined as the ratio of the reflected radiance to the incident irradiance [43]:

$$\mathrm{BRDF} = \frac{dI_{\mathrm{o}}}{I_{\mathrm{i}} \cos\theta_{\mathrm{i}} d\omega_{\mathrm{i}}} \tag{2.1}$$

where I_{i} and I_{o} are the incident and reflected radiance, respectively, and $d\omega_{\mathrm{i}}$ is the solid angle of the incident beam at an incidence angle θ_{i}, as shown in Figure 2.1(a). The denominator $I_{\mathrm{i}} \cos\theta_{\mathrm{i}} d\omega_{\mathrm{i}}$ is the incident irradiance (power per unit projected area), while radiance is defined as power per unit solid angle per unit projected area. It should be mentioned that in Eq. (2.1), the subscript i stands for incidence, while the subscript o stands for observation. This allows the same equation to be used to define BTDF. The observation angle θ_{o} is defined separately for BRDF and BTDF, as shown in Figure 2.1(b). The measurement method will be covered in Chapter 3. The unit of BRDF and BTDF is sr^{-1}, and oftentimes they are spectral properties that depends on frequency. For a perfectly diffuse surface, BRDF is a constant equal to R/π, where R is the d-h reflectance. Note that the value of BRDF and BTDF can exceed unity, for highly specular surfaces or collimated transmittance. By integrating the BRDF and BTDF over the hemisphere, d-h radiative properties R_{dh} and T_{dh} can be obtained, respectively. Analytical BRDF models are also widely used in computer graphics for rendering translucent materials [44, 45].

Rigorously speaking, the light transport in dispersed medium should be described using Maxwell's equation and solved using computational electromagnetics methods such as FDTD, FEM, etc. However, when the polarization state of wave is neglected and considers only short wavelengths, the radiative transfer theory is valid and has been used

extensively in biomedical imaging, remote sensing, astrophysics and radiative heat transfer. The fundamental quantity that describes a field of radiation is radiance I, which is governed by the following radiative transfer equation (RTE) [23]:

$$\frac{\partial I(\hat{\mathbf{s}},t)}{c_0 \partial t} + \frac{\partial I(\hat{\mathbf{s}},t)}{\partial s} = \alpha I_b(\hat{\mathbf{s}},t) - (\sigma+\alpha) I(\hat{\mathbf{s}},t) + \frac{\sigma}{4\pi} \int_{4\pi} I(\hat{\mathbf{s}}_\mathbf{i},t)\Phi(\hat{\mathbf{s}}_\mathbf{i},\hat{\mathbf{s}}) d\Omega_i \quad (2.2)$$

where $\hat{\mathbf{s}}$ is the direction vector of the scattering radiance, c_0 is the speed of light, the subscript 'i' indicates the in-scattering; I_b is the blackbody emittance from medium, often neglected for non-gain medium; σ and α are the scattering and absorption coefficient, respectively, and the physical meaning is the average number of scattering/absorption events that happen per unit propagation length, essentially the inverse of mean free path, usually has a unit of mm^{-1}; the solid angle is represented by Ω , and Φ is the scattering phase function, a measure of the amount of radiating energy propagating in $\hat{\mathbf{s}}_i$ that is redirected into $\hat{\mathbf{s}}$. It can be shown that Φ is the scattered intensity in a direction divided by the average intensity scattered in all directions [23], and is equal to unity for isotropic scattering. Highly scattering medium can often be adequately approximated by isotropic scattering. Note that the above equation is the transient form of RTE, a partial intergro-differential equation w.r.t. time and space. The first term is only significant in ultrafast processes when local equilibrium is not satisfied. It is dropped in the scope of the current work, written as:

$$\frac{dI(\hat{\mathbf{s}})}{ds} = \alpha I_b(\hat{\mathbf{s}}) - (\sigma+\alpha) I(\hat{\mathbf{s}}) + \frac{\sigma}{4\pi} \int_{4\pi} I(\hat{\mathbf{s}}_\mathbf{i})\Phi(\hat{\mathbf{s}}_\mathbf{i},\hat{\mathbf{s}}) d\Omega_i \quad (2.3)$$

For more than a century, the RTE has been used without solid proof of its physical basis. The equation was interpreted from an energy balance point of view: the change in radiative energy on the left-hand side equals to the gain due to emission of the medium, minus the loss due to absorption and scattering, plus the gain due to in-scattering, which is the scattered energy from other directions. This is an analogy of energy balance equation often observed in heat conduction/convection problems. Recently, it has been proved that RTE can be derived from Maxwell's equations under certain assumptions [30], unifying the RTE with classical Maxwell's electromagnetics.

Maxwell's equations provide a mathematical model for phenomena such as diffraction, reflection, polarization, interference, etc., which leads to the inventions of polarizers, gratings, waveguides and the design of complicated optical systems that shaped the modern world. These phenomena emphasize on the wave nature of electromagnetic radiation, and sometimes named wave optics. On the other hand, the discussion of imaging formation, such as lens design, optical aberrations are considered in the geometric optics regime, in which the light is described as propagating rays and does not contain phase information or intensity. RTE falls in the region between these two domains, where phase information of light is dropped but the intensity is retained. It cannot predict resonant phenomena or interference effect, but can handle scattering and absorption, and is widely used in areas where the intensity of light is important.

2.2 Solution to Radiative Transfer Equation

As presented in Eq. (2.3), the RTE is an integro-differential equation that cannot be solved analytically unless certain assumptions are made. Indeed, a significant effect in developing various solutions to the RTE has been made in the past century. Although it is

not the focus of the current work to implement solutions to the RTE, a brief review of selected methods is presented below without heavily involving mathematical equations, but with an emphasize on those adopted in the present work.

2.2.1 Methods Used in Solving RTE

Solving RTE means to obtain the spatial distribution of radiance $I(\hat{\mathbf{s}})$ at an arbitrary location within the medium. Oftentimes the internal energy fluence rate is not critical and only the ratios of the boundary values are needed, which gives the reflectance R and transmittance T. It is also possible to obtain the constants of the RTE, namely σ and α, from a given set of R and T values, known as the inverse problem.

RTE can be solved analytically when the source term on the right-hand side of Eq. (2.3), viz., the absorption and in-scattering component, is known. There are a few cases when this becomes possible, including a non-scattering medium, a cold medium or a purely scattering medium. Boundary conditions are needed to solve RTE. Detailed analysis of these scenarios are found in Ref. [23, 31].

When the medium is mostly scattering, a useful and practical approximate method is the diffusion theory or diffusion approximation [46]. This method expresses the radiance as the sum of a coherent intensity I_{c} and a diffuse intensity I_{d}. The coherent intensity I_{c} exponentially decays from incident surface due to scattering. When the medium is highly scattering, the diffuse intensity I_{d} tends to be almost isotropic, which can be expanded in a series of spherical harmonics. Taking the first two terms of the series and plugging into RTE leads to a diffusion equation, which can be solved analytically with appropriate boundary conditions [46, 47]. Note that the boundary conditions for I_{d} and I_{c} are

different, and the total radiance is their sum. Diffusion approximation has been widely used in bio-optical imaging since tissues are highly scattering and lasers can be used as the optical source. It is simpler and faster compared to solving the full RTE but fails near the surface when first-order scattering becomes more dominant.

Instead of dividing the radiance into collimated and diffuse component, another approach is to assume the energy transfer is one-directional and intensity is isotropic for all positive and negative directions, with a different value [23]. Thus, the radiative transfer reduces to two fluxes of light, one forward and the other backward. This method was originally proposed by Schuster when studying the light through foggy atmosphere, and named two-flux model [48]. The model is further simplified by dropping the emission term, which leads to the Kubelka-Munk model [49], one of the most popular models in textile, paint, color industries. The system of differential equations of Kubelka-Munk is:

$$-di = -(S+K)idx + Sjdx \tag{2.4}$$

$$dj = -(S+K)jdx + Sidx \tag{2.5}$$

where i and j are fluxes of light travelling forward and backward, S and K are Kubelka-Munk scattering and absorption coefficient, which is distinct from σ and α, and x is the distance traveled. As expected, this set of equations can be solved easily, leading to an explicit expression of reflectance R [49, 50]. Note that this method assumes semi-isotropic scattering, while the scattering of large particles is highly anisotropic, as can be shown from Mie theory to be introduced. The two-flux model also could not deal with collimated light, and a three-flux model was developed by adding a collimated component similar to the diffusion approximation [50]. Still, the reflectance at the mismatched boundary cannot be handled in this method. Various revised models have been proposed to extend the

applicability of the two-flux model. For instance, Dombrovsky et al. [51] proposed a modified two-flux model which incorporates boundary reflection, total internal reflection and is capable of dealing with anisotropic scattering. This method has been used in the work in Chapter 5 and 6 [52].

Discrete ordinates method, also known as multi-flux method or S_N-method, is an extension of the two-flux model. Chandrasekhar [53] extended the two-flux model to anisotropic scattering and multidimensions for stellar and atmospheric radiation. Instead of dividing the flux into two, it is discretized into a number of (N) solid angles, transforming the integro-differential equation into N linear differential equations, one for each solid angle. The integral involving the phase function is usually replaced by a Gaussian quadrature. The system of equations can be solved based on matrix eigenproblem approach. Detailed tutorial can be found in Ref. [23, 31]. This method provides much more flexibility in handling anisotropic scattering and radiative heat transfer in enclosures. The idea of angular discretization has also inspired other discretized approaches that offer simpler integrations, such as discrete transfer method, finite volume method, etc [23, 31].

Monte Carlo method provides an alternative method to solve RTE stochastically [23, 31], rather than purely analytically. This method traces the photons from their point of emission to the point of absorption or exiting from the enclosure or medium. The radiative transfer processes are modeled physically, including scattering, reflection, refraction, etc. The desired quantities such as R_{dh} and T_{dh} can be obtained from the total energy of reflected/transmitted photons. In addition, the bidirectional radiative properties, internal fluences and even transient process can also be easily obtained from the model. This method offers great flexibility and can be applied to various radiative transfer problems,

including blackbody emitters [54], mapping of integrating spheres [55] and the photon transport inside highly scattering materials such as silica aerogel, bio-tissues and polymers [56-58]. It has also been adopted in the current work to model a solar reflector [52], and a more detailed discussion of the method will be presented in Chapter 6.

RTE is inherently difficult to solve due to its integro-differential nature. To date, no truly satisfactory RTE solution method has emerged. Nevertheless, various methods have been developed in the past century with distinctive advantages and drawbacks. Selecting the proper ones based on the requirement and the characteristics of the system is crucial.

2.2.2 Forward and Inverse Adding-doubling (AD) Method

For a homogeneous medium with known scattering and absorption coefficients, the directional-hemispherical reflectance R_{dh} and transmittance T_{dh} can be obtained using the forward adding-doubling (AD) method. Introduced by van de Hulst [59] to solve the RTE in a parallel slab, this method considers the incident and exiting radiance on a single thin layer. By juxtaposing two identical slabs and summing the contributions from each slab, R_{dh} and T_{dh} of the double layer slab can be obtained from those of single slab. This process is performed repeatedly until the desired thickness is reached. The detailed mathematics can be found in Ref. [60]. Obviously, this method requires the knowledge of the R_{dh} and T_{dh} of the initial thin layer, which can only be obtained from σ and α by diamond initialization method [50, 60]. Note that this method treats surface as a flat boundary and uses Fresnel reflection to calculate the reflectivity at the boundary, thus it is only valid when the directional hemispherical reflectance and transmittance are not affected by

surface roughness. It is also possible to find internal radiance, simulate media with different layers and internal reflection at boundaries.

Based on the AD method, an inverse adding-doubling (IAD) method was proposed by Prahl [61], which has demonstrated its relatively high converging speed and flexibility in dealing with layered media with anisotropic scattering and absorption, as well as boundary reflection [57]. The IAD method uses the following steps to solve the inverse problem: (1) Guess a set of optical parameters to be determined; (2) Calculate the transmittance and reflectance of the starting thin slab using diamond initialization; (3) Calculate R_{dh} and T_{dh} using AD method and the values from Step 2; (4) Compare the measured R_{dh} and T_{dh} with the calculated ones, calculate the difference and compare with the defined tolerance; (5) If the error is larger than the tolerance, go to Step 1 with an updated set of parameters; otherwise the problem is considered solved.

The set of parameters includes the scattering albedo ω_s, asymmetric factor g, and optical thickness τ. From ω_s and τ, one can retrieve σ and α using the value of the plate thickness d based on the following relations:

$$\omega_s = \frac{\sigma}{\sigma + \alpha} \tag{2.6}$$

$$\tau = (\sigma + \alpha)d \tag{2.7}$$

The asymmetric factor g is the average cosine of the scattering angle, given by [31]:

$$g = \frac{1}{4\pi}\int_{4\pi} \Phi(\theta)\cos\theta d\theta \tag{2.8}$$

where θ is the scattering angle formed by the incident and scattered vector. The value of g provides a simple representation of the directional scattering behavior without involving

complex scattering phase functions. It ranges from -1 to 1, where a positive g implies a highly forward scattering pattern and a negative g indicates backward scattering. For g = 0, the scattering is isotropic.

Ideally, all three of g, α and σ are needed to solve RTE, with g replacing the integral on the right-hand side of Eq. (2.3). For the inverse problem, R_{dh} and T_{dh} provide only two values per wavelength, insufficient to solve for three unknowns. An additional measurement of the collimated transmittance T_{coll} is needed from the IAD program, but the collimated signal is proportional to $\exp(-(\alpha+\sigma)d)$, requiring a much thinner sample for a highly scattering/absorbing medium. An alternative is to use reduced scattering coefficient $\sigma' = (1-g)\sigma$, which reduces the number of unknowns to two and allows for the solving the problem with only R_{dh} and $T_{dh.}$ This process, sometimes called "isotropic scaling" [51], has proved to be valid in the calculation involving directional-hemispherical properties [50]. In this work, the scattering is assumed to be isotropic by setting g = 0, and then the scattering and absorption coefficient are obtained from the IAD method.

2.2.3 Scattering from Single Particles

A bottom-up approach in solving the RTE is to obtain the scattering function from the scatterers, such as the impurities or pores of the medium, which often have irregular shapes, and the size is comparable to or larger than the wavelength of the electromagnetic waves. The concentration of the scatters is needed to obtain scattering and absorption coefficient from the scattering function of a single scatter. Then R_{dh} and T_{dh} of the slab can be solved by numerical integration of the RTE, or simply using the forward AD method introduced above.

The simplest scattering event is the scattering of a plane parallel electromagnetic wave by a small spherical particle, which is described in the Mie theory by rigorously solving Maxwell's equations. Scattering from other shapes also can be obtained using T-matrix method [62], but it is found that non-spherical particles have quite similar scattering profile to their equivalent spheres by averaging over orientation or sizes [23], which saves the effort of digging into the data base of T-matrix results. The two critical parameters are the normalized complex index of refraction $m = (n + i\kappa)/n_0$ and the size parameter $x = \pi d / \lambda$. Here n and κ are the real and imaginary part of the optical constants of the sphere, respectively; n_0 is the refractive index of the medium; d is the diameter of the sphere and λ is the incident wavelength. Then the scattering and absorption efficiency is given by [63]:

$$Q_{\text{sca}} = \frac{2}{x^2}\sum_{n=1}^{\infty}(2n+1)(|a_n|^2 + |b_n|^2) \tag{2.9}$$

$$Q_{\text{ext}} = \frac{2}{x^2}\sum_{n=1}^{\infty}(2n+1)\,\text{Re}(a_n + b_n) \tag{2.10}$$

where a_n and b_n are:

$$a_n = \frac{m\psi_n(mx)\psi_n'(x) - \psi_n(x)\psi_n'(mx)}{m\psi_n(mx)\xi_n'(x) - \xi_n(x)\psi_n'(mx)} \tag{2.11}$$

$$b_n = \frac{\psi_n(mx)\psi_n'(x) - m\psi_n(x)\psi_n'(mx)}{\psi_n(mx)\xi_n'(x) - m\xi_n(x)\psi_n'(mx)} \tag{2.12}$$

$$\psi_n(z) = \sqrt{\frac{\pi z}{2}}J_{n+1/2}(z) \tag{2.13}$$

$$\psi_n(z) = \sqrt{\frac{\pi z}{2}}H^{(1)}_{n+1/2}(z) \tag{2.14}$$

Here ψ_n and ξ_n are the Riccati-Bessel functions which are related to Bessel function of the first kind J_n and the Hankel function of the first kind $H_n^{(1)}$. The number of terms needed for convergence of the efficiencies in Eq. (2.9) and (2.10) is given as $n_{\max} = x + 4x^{1/3} + 2$ by Bohren et al. [63]. The difference of scattering and extinction efficiency is the absorption efficiency:

$$Q_{\text{abs}} = Q_{\text{ext}} - Q_{\text{sca}} \tag{2.15}$$

The efficiencies are related to the scattering and absorption cross-section by:

$$Q_i = \frac{\sigma_i}{\pi d^2 / 4} \tag{2.16}$$

For a particle system with various sizes, the total absorption and scattering coefficients could be determined by the following rule:

$$\sigma = \sum_{i=1}^{n} f_i \frac{Q_{\text{sca},i} A}{V}, \qquad \alpha = \sum_{i=1}^{n} f_i \frac{Q_{\text{abs},i} A}{V} \tag{2.17}$$

where A and V is the cross-sectional area and volume of a single particle, respectively, f_i is the volume concentration of the i-th particle. Note that the α value calculated in Eq. (2.17) accounts for the absorption of particles, but not the loss in the medium. For a lossy medium α should be determined by the optical constants of the medium, as to be shown in Chapter 4. When monodisperse system of particles is considered, the equation reduces to:

$$\sigma = \frac{3 f Q_{\text{sca}}}{2d}, \qquad \alpha = \frac{3 f Q_{\text{abs}}}{2d} \tag{2.18}$$

It is worth mentioning that for this method to be valid, it is crucial that the scattering should be independent. When two particles are in close proximity, scattering can differ

from Mie theory due to constructive or destructive interference of scattered radiation, as well as the interaction of evanescent fields. These effects become less dominant when the distance between particles increases, known as the "independent scattering". There are plenty of research on the validity domain of independent and dependent scattering [23, 64], and the current work only focus on independent scattering. It is claimed, though, that all scattering events are essentially "dependent" regardless of how far away the two particles are separated, thus the concept of "independent scattering" has little heuristic value [30]. The reasoning is that the forward scattering interference and coherent backscattering effect (also known as weak localization) are ubiquitous and cannot be predicted by the scattering pattern of individual particle. We argue that these effects are extremely narrow and hard to observe in the systems studied and the individual scattering properties of the particles still provide insights to solving the multiple scattering problem. More efficient mathematical tools that can solve multiple scattering with consideration of dependent scattering are yet to be developed.

2.3 Radiative Cooling: Principles and Examples

The practice of radiative cooling dates back to ancient time, when people found radiation to clear night sky could greatly enhance the heat dissipation of buildings. But it was not systematically studied until the twentieth century [65, 66]. It is known that the atmosphere exhibits spectrally selective absorption lines or bands due to gas molecules and aerosol particles. Yet, for a cloudless day with relatively low humidity, the sky could be largely transparent to electromagnetic waves from about 8 μm to 13 μm, which is referred as the infrared atmospheric window [67]. A significant portion (around 35%) of radiation emitted from a blackbody at ambient temperature (about 300 K) falls in this window,

equivalent to a cooling power of 160 W/m^2. Figure 2.2 plots the atmospheric transmittance obtained from Gemini observatory [68], from 0.9 to 15 μm (the transmittance data is available up to 26 μm). The solar irradiance is also plotted using data from Air Mass 1.5: ASTM G-173-03 [69], which defines a standard direct normal spectral irradiance and a standard total (global, hemispherical, within 2-π steradian field of view of the tilted plane) spectral irradiance from 0.28 μm to 4 μm.

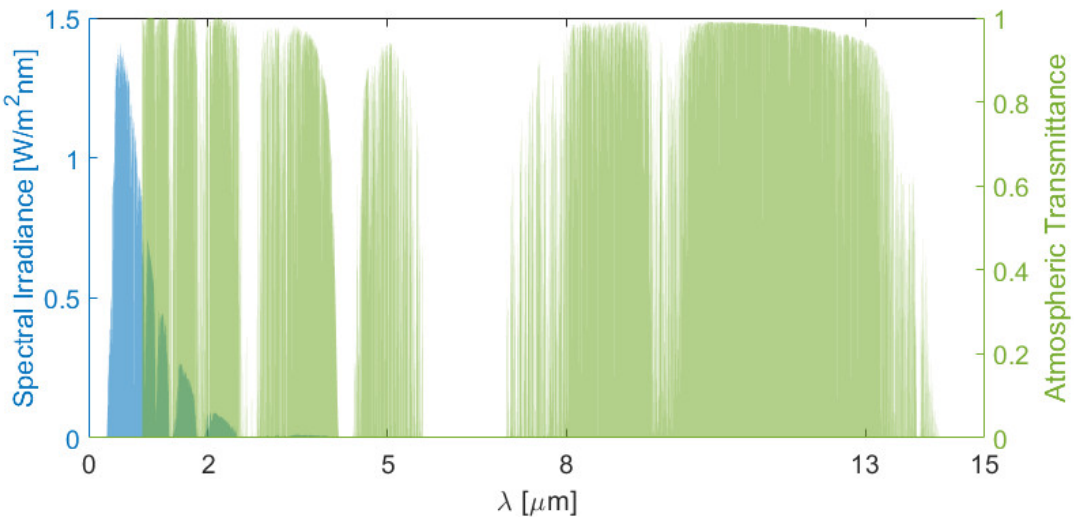

Figure 2.2. Solar radiation spectrum for air mass 1.5 based on the global 37-deg tilt data, along with the infrared spectrum of the atmospheric transmission from Gemini observatory.

Passive radiative cooling can be grouped into three main categories according to the specific application: (1) Nocturnal refrigeration for which the purpose is to reach a temperature below the ambient, e.g., to produce cooling water or to make ice [70-72]. In this case, the material should have a high emissivity in the infrared atmospheric window and a low emissivity elsewhere. Because only 0.2% of the thermal radiation emitted from

an object at ambient temperature is at wavelengths shorter than 4 μm, the radiative properties in this region play minimal role for nighttime cooling, same for diurnal cooling with a clear sky when the sun is blocked. (2) Daytime cooling and energy saving, where reducing the temperature rise is desired under the exposure of solar radiation. This could be achieved by using a solar reflective material with high broadband infrared emissivity [73, 74]. (3) Daytime refrigeration, which aims at obtaining an equilibrium temperature below the ambient under sunlight. Such daytime refrigeration has not been achieved until recently when materials with high solar reflectance (greater than 0.9) and selective high emissivity within the infrared atmospheric window are employed [65, 75-77]. To achieve daytime cooling or refrigeration under direct solar irradiation, enhancing materials' reflectance in the wavelength region $0.3\ \mu\text{m} \le \lambda \le 4.0\ \mu\text{m}$ is critically important to reduce the absorption of solar irradiation which could exceed 1000 W/m^2.

To achieve day-time radiative cooling, Raman et al. [75] fabricated a photonic multilayer structure with 0.97 solar reflectance, while emitting strongly in the infrared atmospheric window, and demonstrated refrigeration nearly 5°C below the ambient under solar irradiance exceeding 850 W/m^2. Subfreezing refrigeration was also achieved by the same group in a vacuum test chamber by blocking solar irradiation [71]. However, the fabrication cost and susceptibility to corrosion for such photonic meta-surfaces are the bottlenecks for scaling up.

An alternative, economically viable approach has recently been demonstrated by several research groups, achieving radiative cooling using dispersed materials. Using TiO_2 pigments, Harrison and Walton [65] were the first to achieve daytime refrigeration of 2°C below the ambient under direct sunlight at noon during a winter day in a high latitude

geographical location (51°N). Nanoparticle-based paint and coatings have been proposed and demonstrated day-time cooling effect by several groups [73, 78, 79]. Mandal et al. [76] presented a scalable porous polymer coating that can be directly applied to existing roofs or walls. Zhai et al. [70] used a silver coated glass-polymer hybrid material and demonstrated scalability while achieving a noontime radiative cooling power of 93 W/m^2. While Ag is a good reflector in the visible and infrared and has been used in several publications, it has a relatively high absorptance in the ultraviolet especially at wavelengths shorter than 0.35 μm. It seems that the best configurations can reflect about 0.96-0.97 of the solar irradiation.

In the present research, a sintered polymer named polytetrafluoroethylene (PTFE) is used, which is essentially the white material used as the inner coating of integrating spheres and diffuse reflectance standard [57, 80, 81]. It is of extremely high diffuse reflectance from ultraviolet to near-infrared (0.2-2.5 μm wavelength). To achieve opacity and high reflectance, the thickness of the PTFE needs to be several millimeters, which is not practical for large area applications. The design in the current study uses a PTFE sheet of submillimeter thickness and a reflector made of a Ag film. It is expected that the overall solar reflectance of this dual-layer structure can be enhanced even though the PTFE layer is semitransparent. In addition, it is known that a 10-mm thick PTFE acts as a perfect diffuse reflector, but it is unclear if the reflectance will remain diffuse when the thickness is reduced to a submillimeter scale and when it is applied on a glossy surface. Experimental and theoretical studies on the directional-hemispherical as well as bidirectional radiative properties of the dual-layer structure are performed.

2.4 Rigorous Coupled-Wave Analysis

Solving the Maxwell's equations numerically can be done using various computational methods, such as finite element method (FEM), finite-difference time-domain method (FDTD), method of moments (MOM), etc. These methods have been developed for several decades and are available in a number of commercial softwares, such as Remcom's XFDTD, Lumerical's FDTD solutions, FEM-based COMSOL's RF Module and Ansoft's HFSS. Based on the meshing and discretization, they can handle the light-matter interaction of complex structures and light sources, but also suffer from the discretization error and significant computation cost. For periodic structures, especially micro/nano-scale gratings, rigorous coupled-wave analysis (RCWA), also referred to as Fourier modal method is more suitable and does not require a discretization scheme.

Isotropic RCWA for 1-D grating was first proposed in 1981 by Moharam and Gaylord [82], and an efficient implementation was later presented [83]. The algorithm was reformulated by Li [84] with a stable Fourier factorization rules. For anisotropic gratings, Glytsis and Gaylord [85] also formulated RCWA for 1-D case in three-dimensional space. Radiative properties of other periodic structures can also be efficiently calculated based on the formula for gratings. An easy-to-implement algorithm for 2-D periodic structures made of biaxial materials with a diagonal permittivity tensor is presented by Zhao [41]. The current work does not intent to focus on the theoretical development or implementation of RCWA, and only a brief introduction of the simplest case is presented to illustrate the gist of this method.

The Helmholtz equation for E is:

$$(\nabla^2 + k^2)E = 0 \tag{2.19}$$

Take transverse electric (TE) mode for example, E field only has component in the transverse (y) direction, then:

$$\frac{\partial^2 E_y(x,z)}{\partial z^2} + \frac{\partial^2 E_y(x,z)}{\partial x^2} + k_0^2 \varepsilon(x) E_y(x,z) = 0 \tag{2.20}$$

Note that this equation is valid in the incident and refracted medium, with different permittivity values, and k_0 is the wave vector in vacuum. To solve the Helmholtz equation, the electric field (inside the diffracted medium) is expressed with a Fourier expansion in terms of the space-harmonic fields as:

$$E_y(x,z) = \sum_j \Psi_j(z) e^{ik_{xy}x} \tag{2.21}$$

Likewise, the dielectric function should also be expanded in a Fourier series:

$$\varepsilon(x) = \sum_m \varepsilon_m \exp\left(i \frac{2m\pi}{\Lambda} x \right), m = 0, \pm 1, \pm 2, ... \tag{2.22}$$

Plug into Eq. (2.20):

$$\frac{\partial^2 \Psi_j(z)}{\partial z^2} = k_{xj}^2 \Psi_j(z) - k_0^2 \sum_p \varepsilon_{j-p} \Psi_p(z) \tag{2.23}$$

which is a system of N equations, and N is the number terms used in Fourier expansion. This system of equations can be normalized with k_0 and written in matrix form:

$$\frac{\partial^2 \mathbf{\Psi}}{\partial z'^2} = (\mathbf{K_x^2} - \mathbf{E})\mathbf{\Psi} = \mathbf{A\Psi} \tag{2.24}$$

where $\mathbf{K_x^2}$ is a diagonal matrix formed by k_{xj} / k_0, the normalized coordinate is $z' = k_0 z$, and $\mathbf{E}$ is formed by permittivity harmonics.

Notice that matrix **A** is non-diagonal, the second order differential equation can be easily solved once the system is diagonalized. The key is to find the eigenvalues and eigenvectors of **A**. Let $\mathbf{\Psi} = \mathbf{W\Gamma}$, where **W** is the matrix whose *m*-th column is the eigenvector corresponding to the *m*-th eigenvalue of the matrix **A**. By the definition of diagonalization, it is known that $\mathbf{D} = \mathbf{W}^{-1}\mathbf{AW}$, where **D** is the diagonal matrix with the eigenvalues of **A**. Now the decoupled equation is:

$$\frac{\partial^2 \mathbf{\Gamma}}{\partial z'^2} = \mathbf{D}\,\mathbf{\Gamma} \tag{2.25}$$

the solution of which is simply:

$$\Gamma_j(z) = c_j^+ e^{k_0 q_j (z-d)} + c_j^- e^{-k_0 q_j z}, \;\; j = 1,2,3,...,n \tag{2.26}$$

where q_j is the positive square root of the eigenvalue of matrix **A**. And the coefficient of Fourier series of *E* can be obtained from $\mathbf{\Psi} = \mathbf{W\Gamma}$. The unknowns c_j^+ and c_j^- from above can be obtained by phase matching condition at the interface, and *H* field is obtained from the Maxwell's equation as:

$$H = (\frac{j}{\omega\mu})\nabla \times E \tag{2.27}$$

The details of the formula can be found in Ref. [83], as well as the similar formula for TM case.

RCWA method provides a semi-analytical solution to the electromagnetic waves propagating in periodic medium and is very suitable for investigation of radiative properties of gratings in the present study. It is more flexible in dealing with small

structures like 2D materials compared with FEM and FDTD, which becomes very challenging and time-consuming due to the requirement of sufficiently small and fine meshing. As pointed out by Zhao [41], when structures with small characteristic lengths coexist with large structures, such as the hybrid grating-graphene structure, this method is an ideal tool for numerical study.

2.5 Magnetic Polaritons in Deep Metal Gratings

The finding of magnetic polariton starts from 1999, when Pendry et al. [35] reported that a nonmagnetic metallic element with subwavelength features, such as a split ring or a Swiss roll structure, exhibits an effective magnetic permeability that can be tuned to a wide range of values not accessible in natural materials. This phenomenon originates from the induced electric current in the metal structure that give rise to a magnetic response. When combined with negative permittivity, these structures ultimately lead to the discovery and development of materials with effective negative refraction index, a special class of metamaterials [86]. Similar to the surface plasmon polariton (SPP), which refers to the collective motion of conduction electrons due to the coupling with external electric field, the magnetic response or coupling has been termed as the magnetic plasmon or magnetic polariton (MP) [25]. Over the past two decades, MPs have demonstrated applications in extraordinary optical transmission, cloaking, coherent thermal emitters, and enhanced absorption when coupled with novel 2D materials [87]. However, they were mostly demonstrated on spherical or cylindrical structures, while experimental demonstration of MPs on metallic gratings is rarely reported, despite the abundant theoretical studies and relatively simpler fabrication processes.

Wang and Zhang [88] theoretically and later experimentally [37] demonstrated coherent thermal emission from thin metallic gratings due to the excitation of MP. However, this type of metamaterials is based on the resonance between the periodic strip on top and the metallic substrate separated by a thin dielectric film. Mattiucci et al. [89] theoretically demonstrated a temporally coherent, wide-angle thermal radiation source based on the bulk resonance of a deep Al grating. Zhao and Zhang [90] examined the fundamental mechanism of MPs inside deep metallic gratings with a full-wave analysis and a simplified model. Their work has distinguished MPs from the conventional cavity modes. In addition to coherent emission, it has also been reported that MPs could facilitate extraordinary transmittance in slit arrays [39, 91], which has broad applications in optical devices including modulators, color filters, and polarizers. Recently, Zhao and Zhang [40] reported the strong plasmonic coupling of deep metal gratings with graphene, which shows perfect or near-perfect absorption that can be tuned for subwavelength imaging or energy harvesting. Similar coupling was also demonstrated in hBN-grating structure [92]. Nevertheless, no experimental work has been conducted so far to study the effect of MP on the radiative properties of deep metal gratings. An effort to demonstrate the MPs in deep Al gratings will be presented in this work, with emphasize on the different dispersion contour for in-plane and off-plane lay-out of gratings.

CHAPTER 3

INSTRUMENTATION FOR MEASUREMENT OF SPECTRAL RADIATIVE PROPERTIES

The study of reflectance and transmittance of a material as a function of wavelength is termed as spectrophotometry. This chapter presents the information of the spectrophotometers used in the thesis, which includes a monochromator with an integrating sphere, for wavelength from 0.28 μm to 1.8 μm; a Fourier transform infrared spectrometer (FTIR) with various accessories, for wavelength from 1.5 μm to 19 μm; and an optical laser scatterometer operated at wavelength of 635 nm. Spectral and directional-hemispherical (d-h) radiative properties could be obtained with the help of integrating sphere, while the specular reflectance is captured using the specular reflectance accessories for FTIR. Directional-directional (d-d) radiative properties is obtained using the optical scatterometer only at the prescribed wavelength. Operating principles of the equipment are detailed, and the measurement equations are derived accordingly.

3.1 Monochromator with Integrating Sphere

The schematic of the monochromator with an integrating sphere is shown in Figure 3.1. A tungsten-halogen lamp is chosen as the light source with a broad spectral range from visible to NIR. The lamp should be kept on for a least one hour before the measurement for the system to reach thermal equilibrium. Several band-pass filters are mounted on a filter wheel and placed between the monochromator and the light source. The transmission window for the filters are from 400 nm to 750 nm, 750 nm to 1200 nm and 1100 nm to

1900 nm. By interchanging the filters, the grating monochromator (Oriel Instruments Cornerstone 130) could produce highly selective single wavelength light. The broadband spectrum from the lamp beam is diffracted by the gratings (1200 lines/mm) into various directions, and only the selected wavelength leaves from the exit slit. The grating provides a resolution of 10 nm at the 500 nm wavelength when combined with a 1.56 mm wide entrance and exit slit [93]. The width and height of the exit beam could be reduced by blocking the exit slit when needed. This is known as a dispersive spectrophotometer, which is frequently used in visible to near infrared region due to higher accuracy, another example of dispersive methods is a prism. A mechanical chopper is then used to modulate the light at a frequency of 400 Hz, which is synchronized to a lock-in amplifier (EG&G 7265DSP) to pick up the signal. Two collimating lenses ($f_1 = 25$ mm and $f_2 = 100$ mm) are used to focus the incident light onto the sample surface. When center-mount scheme is used, the incident light is focused onto the center of the integrating sphere. This scheme offers convenience in changing the angle of incidence by rotating the sample holder, but is incapable of differentiating reflectance R_{dh} from transmittance T_{dh} , and only the summation $R_{\mathrm{dh}} + T_{\mathrm{dh}}$ is measured [94]. For the studies in the present work, either back-mounting is used for R_{dh} and reference measurement, or front-mounting is used for measuring T_{dh}, as shown in the schematic. The focus can be tuned by moving the lenses along the axis, and be visualized by attaching a piece of anti-sticking tape to the focal plane.

The integrating sphere is a 200-mm-diameter sphere imbedded in a cube, custom-designed from Sphere Optics, Inc. Five ports are opened at the center of each face, and only the front and back port are being used. The port diameter is 25 mm and can be reduced

by half using a smaller aperture when the sample is too small. The inner wall is coated with polytetrafluoroethylene (PTFE), producing a nearly diffuse reflectance of approximately 0.99 in the working wavelength of the equipment [81]. A silicon detector and a germanium detector are used for visible and near infrared measurement, the working range is from 190 nm to 1 μm, 0.8 μm to 1.8 μm, respectively. Considering the limitation of light source and filters, the measurements are taken with Si detector from 0.4 μm to 1 μm, and with Ge detector from 1 μm to 1.8 μm. Usually an overlapped region of around 60 nm is taken with both detectors to test the signal consistency. The filters should also be switched accordingly as the output wavelength changes. Note that by selecting a different filter with a pass band from 350 nm to 550 nm, measurement range can be extended below 400 nm. This is of special interest for solar energy applications, which requires data starting from 280 nm. The uncertainty of measurement from 280 nm to 350 nm is still large due to the spectral power distribution of light source, as well as the cut-off limit of the filter being used.

Inside the integrating sphere, a baffle is fixed above the detector to block the first order reflection directly from the sample, which is required from the derivation of the integrating sphere equation. A 10-mm thick PTFE slab is used as a reflectance standard and mounted at the back of the integrating sphere when collecting the reference signal. The incident light undergoes multiple reflections inside the sphere before being captured by the detector. The detected signal is passed to the trans-impedance pre-amplifier and then to the lock-in amplifier, which picks up the modulated signal at 400 Hz. Due to the presence of the modulation, most experiments do not require a dark room, unless the reflectance from the sample is very small, and the gain from pre-amplifier is too large that room lighting causes the saturation of the detector. The data acquisition from the lock-in amplifier is

automated using LabVIEW. At each point, multiple data points are acquired (usually 10) and averaged. The ratio of the obtained power over that from the reflectance standard gives the R_{dh} or T_{dh} of the measured sample. It is worth mentioning that in the current scheme, the reflectance is relative which depends on the reference sample, while the transmittance is absolute value. Absolute reflectance measurement using integrating spheres can be found in Ref. [95]. The absolute uncertainty in this work is estimated to be 0.02 for R_{dh} and 0.01 for T_{dh} [29, 96].

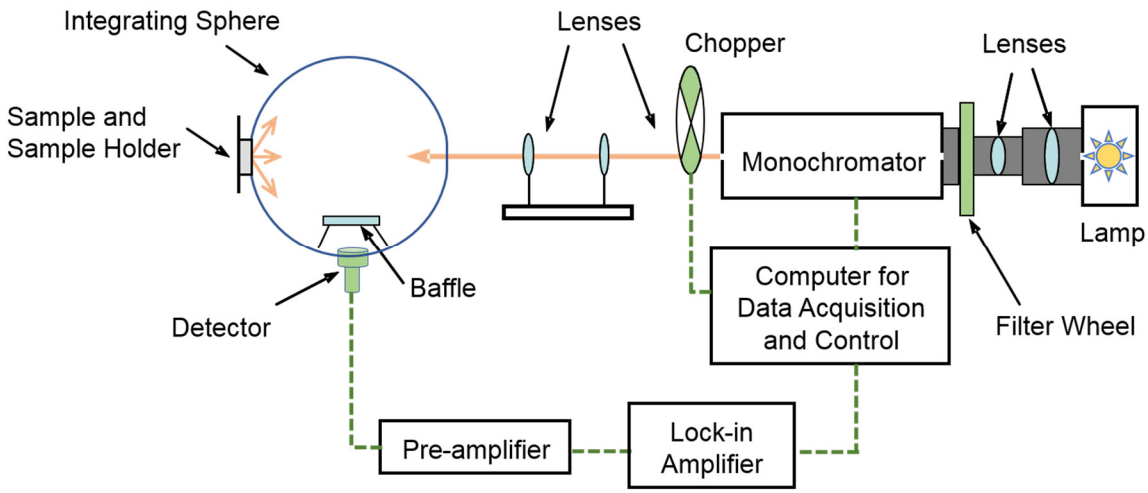

Figure 3.1. Schematic of the integrating sphere with monochromator for visible to near infrared range radiative properties measurement.

When attaching the sample to the back, a vertical sample holder is used for diffuse samples, and a slightly tilted sample holder is used when measuring highly specular surfaces. The tilted sample holder can prevent the specular reflection from escaping from the front port, so the d-h reflectance can be measured accurately. It is assumed that by slightly tilting the sample, the reflectance should not change significantly. Strictly

speaking, the condition under which the reference signal and the sample signal are taken should be identical, meaning that the fractional surface area of sample, entrance port and PTFE should remain the same. By switching the sample and the reference PTFE slab during the measurement, this criterion is not satisfied. It is suggested that two symmetric ports should be opened at the back side, each at 8° normal to the entrance port. During the measurement, one port is mounted with sample while the other is left blank. This method measures radiative properties of 8° incidence rather than normal incidence, gives absolute reflectance value that does not require correction based on reference reflectance, and can easily deal with both specular and diffuse surfaces, with an error reduction to around 0.1% [95]. However, it requires a customized integrating sphere and precise control of its rotation during the measurement, which significantly increases the cost and complexity of the system.

3.2 Fourier Transform Infrared Spectrometer and Accessories

The near- and mid-infrared radiative properties are measured using an ABB FTLA 2000 FTIR. The schematic of FTIR is shown in Figure 3.2. An FTIR is essentially an interferometer, with a moving mirror scanning a certain distance L while holding the other mirror still. The incident light is divided into two beams by the beam splitter and recombines after being reflected by the two mirrors. The optical paths of the two beams have a difference δ, which leads to an interference pattern after the two beams recombine. The obtained interference pattern, i.e. interferogram $I(\delta)$, is transformed to frequency domain using Fourier transform, as:

$$B(\nu) = \int_{-\infty}^{\infty} I(\delta)\cos(2\pi\nu\delta)d\delta \tag{3.1}$$

where $B(\nu)$ is the obtained spectrum and ν is the wavenumber. Ideally, the Fourier transform requires the optical path difference ranging from $-\infty$ to ∞, while in reality, the mirror only moves a distance of L. It can be shown that by doing so, the resolution of the obtained spectrum is $\frac{1}{L}$ [97]. While the resolution in the frequency domain is decided by the integration range in the spatial/time domain, the range of the frequency domain depends on the integration resolution in the spatial/time domain, i.e. dL. If the mirror takes more steps and has a smaller dL value, the obtained spectrum should be broader. However, the spectral range is oftentimes limited by the detector's responsivity and bandgap, light source and transmission window of the lenses in the system.

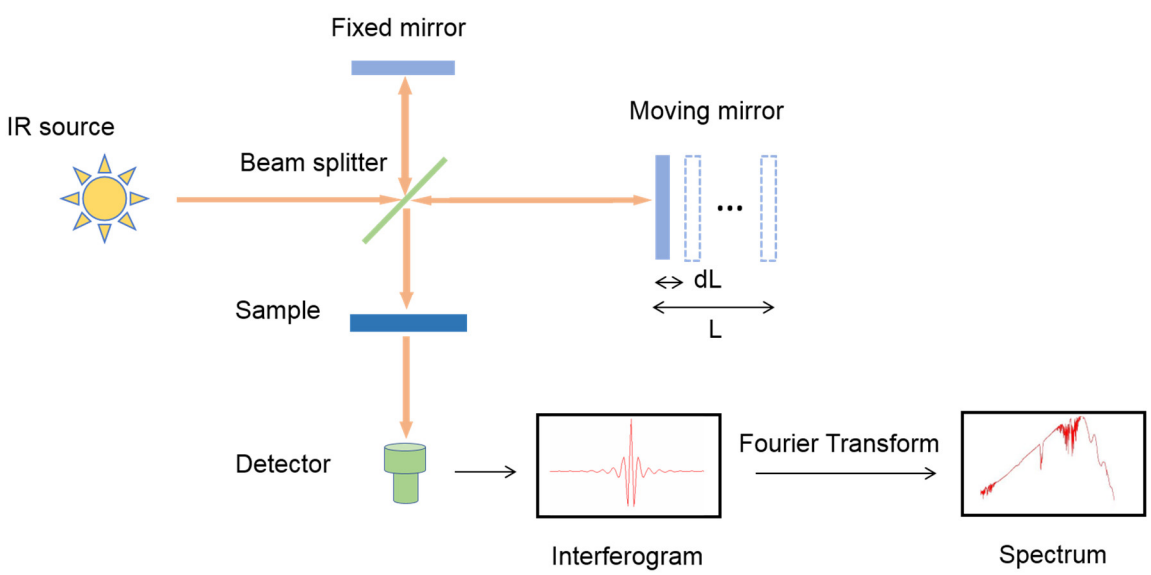

Figure 3.2. Schematic for the principles of FTIR, the moving mirror collects interferogram in the spatial domain and utilize Fourier transform to obtain frequency domain spectrum.

For a monochromatic light, the interference pattern should be a sinusoidal signal. Yet in FTIR where a broadband emitter is used as the light source, the interference pattern is the superposition of infinite sinusoidal signals each with a different frequency. At the position where $\delta = 0$ though, all the sinusoidal signals should be at maximum due to the constructive interference of the two beams, this phenomenon is called centre-burst. Note that sometimes there is indeed a monochromatic light with a known wavelength in the system, oftentimes a He-Ne laser, which is used for calibration of the optical path difference and to improve the resolution of the system.

In this work, an ABB FTLA-2000 FTIR was used for spectroscopic measurements, with a near infrared source of quartz halogen and a mid-infrared source of SiC. The NIR source should be turned off after each measurement to save lifetime while the MIR source can be left on. The lowest wavenumber measurable of this device is limited by the transparency window of ZnSe to approximated 500 cm^{-1}, while the highest wavenumber is limited by the magnitude of the signal and the sampling frequency *dL*. Data up to 14000 cm^{-1} can be obtained, but the cut off wavelength is usually 6000 cm^{-1} to 8000 cm^{-1}, beyond which the noise is too large. Note that two sets of detectors are used, a deuterated triglycine sulfate (DTGS) detector for specular reflectance/transmittance, and a HgCdTe (MCT) detector with a 100-mm-diameter gold-coated integrating sphere for d-h reflectance/transmittance. The MCT detector has a cut-off wavenumber around 630 cm^{-1} (16 μm) and requires liquid nitrogen cooling before measurement. The minimum resolution of this device is 1 cm^{-1}, while during experiment 4 cm^{-1} or 8 cm^{-1} is often used to save scan time and remove unwanted interference features. The FTIR can also be coupled with external sources to achieve specific measurement [37].

Before measurement, the NIR source should be turned on for at least one hour to achieve thermal equilibrium, then alignment should be checked by observing the interferogram of the system. It is expected to see an centre-burst in the interferogram, otherwise the system should be checked. Next a background scan is obtained by measuring without loading any sample. Note that for transmittance measurement, no reference sample is needed, whereas for reflectance measurement, a reference piece, oftentimes a gold substrate with known reflectance, is placed at the sample holder as the reflectance standard. An open beam test is needed for reflectance measurement to account for the reflectance from apertures in the accessories. After loading the sample, the spectrum is taken and averaged multiple times to achieve smaller noise. While the measured value gives the transmittance directly, the reflectance can be computed by the following equation:

$$R = \frac{I_{\text{sample}} - I_{\text{open beam}}}{1 - I_{\text{open beam}}} \times R_{\text{ref}} \tag{3.2}$$

where I is normalized using the background, and R_{ref} is the reflectance standard of the gold piece, taken as 0.985 for deposited gold film and 0.95 for the roughened gold substrate used in the integrating sphere. For absolute reflectance measurement, one can either use the aforementioned integrating sphere design [95] or the classical V/W design. Purging can be done both inside and outside the FTIR in the accessories, using nitrogen to remove CO_2 and H_2O vapor in the atmosphere, which are highly absorbing at certain wavelength. It is necessary to obtain another background when the system state is altered, for instance the purging has stopped, the polarization of the incident light is changed, or simply after around an hour, when the intensity from the light source might have drifted.

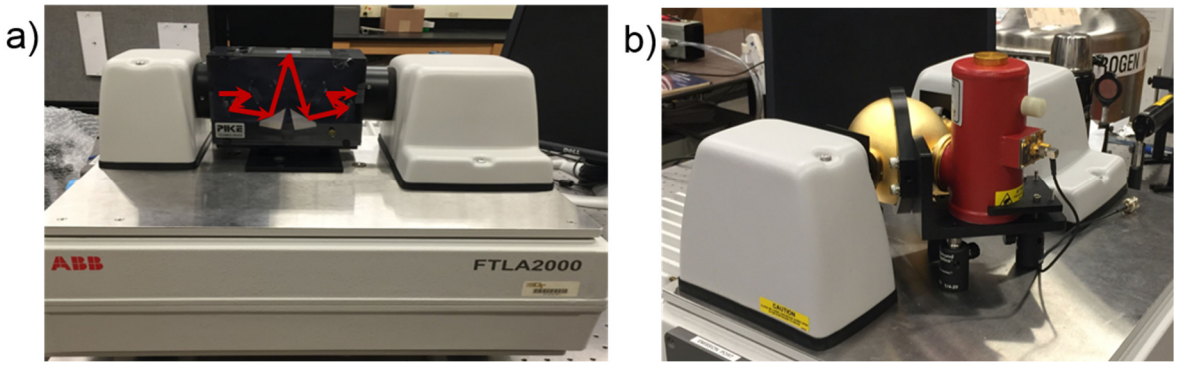

Figure 3.3. Pictures of the FTIR accessories; (a) a specular accessory collecting reflection at 10° incident, accessories at 30° and 45° incident angle are also available; (b) a gold-coated integrating sphere with a MCT detector for directional-hemispherical properties measurement.

It is beneficial to take a closer look at the accessories being used in the thesis, as shown in Figure 3.3(a). The specular accessories provide reflectance measurement at 10°, 30° and 45° using three separate devices. This feature is important for the grating project to observe the magnetic polaritons. The d-h measurement for both transmittance and reflectance are done using the integrating sphere shown in Figure 3.3(b). The light beam is focused at around the center of the FTIR stage, therefore when measuring the reflectance, the sphere should be moved closer to the light source to focus on the backside, and opposite when measuring the transmittance. Purging inside the integrating sphere can be done when measuring the reflectance by connecting the integrating sphere with the port of the FTIR. Note that a tilted and a vertical sample holder are available in lab, similar to the monochromator with integrating sphere. But since the integrating sphere is smaller, the

loss from the front port is more significant. The estimated absolute uncertainty is 0.03 for R_{dh} and 0.01 for T_{dh} [96].

Overall FTIR has the advantage of high throughput, better signal-to-noise ratio in the infrared and higher wavelength accuracy compared to dispersive spectrometers. But dispersive methods usually have the advantage of being easier to analyze, works well for DC detectors and slow AC detectors, and are chosen for visible to near-infrared region measurement.

3.3 Optical Laser Scatterometer

The monochromator and FTIR are used for spectral measurement, with limited information on the angular radiative properties. An optical scatterometer system has been designed and calibrated by earlier studies in the group [43], which provides angle-resolved R and T at a certain wavelength. As shown in Figure 3.4, a laser diode coupled with optical fiber is used to provide incident light at 635 nm. The laser diode is equipped with a thermoelectric cooling system to provide power stability within a standard deviation of 0.2%. The laser is modulated using a lock-in amplifier at 400 Hz to pick up the scattered light signal from the background radiation. The beam passes through a collimator with a pair of lenses and a small aperture, after which a linear polarizer is mounted on a dial to allow for the selection of polarization. The presence of polarizer is always required since the laser is not randomly polarized, a small perturbation during the experiment could alter the polarization state of the incident light, thus affecting the beam splitting ratio. The beam splitter divides the light into two portions: the transmitted beam is incident on the sample and then captured by detector A, and the reflected beam going to a stationary reference

detector B. Both signals are sent through separate trans-impedance pre-amplifiers and picked up by the lock-in amplifier. By recording them simultaneously, the laser fluctuation can be better accounted for.

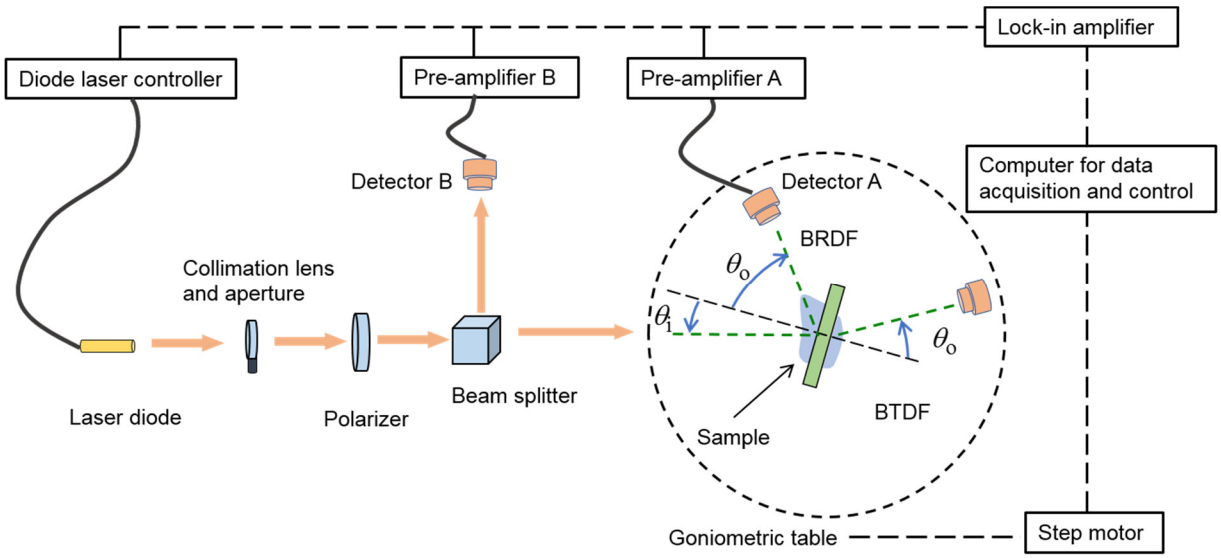

Figure 3.4. Schematic of the TAAS system; note that the arrows in the goniometric table indicate the direction in which these angles increase, and that the observation angle θ_o is defined separately for BRDF and BTDF, one detector is rotated to capture the signal at various observation angles.

The sample is mounted on a goniometric table with three rotary stages, which provide both in-plane and out-of-plane BRDF/BTDF measurement. In the schematic, only the polar angle, or zenith angle θ is shown, though the dimension ϕ can also be varied from 0 to 90°. Note that the observation angle θ_o is defined separately for BRDF and BTDF to ensure the range is within $\frac{\pi}{2}$ to $-\frac{\pi}{2}$, and the direction in which it increases is indicated by the arrows. The detector A and sample are mounted on different stages

controlled by steps motors and automated with LabVIEW. The BRDF within $\pm 2.5^{\circ}$ of the retroreflection direction cannot be measured since detector A blocks the incident beam. At each measurement step, the signal from both detectors are measured multiple times (usually 10 times) and averaged. The detailed information on the resolution, accuracy and repeatability of the stages can be found in Ref [43].

The measurement equation for BRDF is given as:

$$\mathrm{BRDF} = C \frac{P_{\mathrm{A}}}{P_{\mathrm{B}} \cos\theta_{\mathrm{o}} \Delta\omega_{\mathrm{o}}} \tag{3.3}$$

where P_A and P_B are the power collected by detector A and B, respectively, and the solid angle of the detector A is measured to be $\Delta\omega_{\mathrm{o}} = 2.11 \times 10^{-4}$ sr. A precision aperture of 8 mm diameter is placed in front of detector A, and the distance between the sample and the precision aperture is 488 mm. Consequently, the solid angle deviates from the previous reported value of 1.84×10^{-4} [43]. The constant C compensates for the beam splitting ratio and gain difference from the two pre-amplifiers. Thus, it is necessary to measure the beam splitting ratio by unloading the sample and collecting the transmitted light directly using detector A, each time before and after experiment. The power of the same beam before and after being diffusely scattered can be four orders of magnitude different, therefore a large dynamic range of the pre-amplifiers is needed to ensure at least five significant digits from the lock-in amplifier output. Note that incident wavelength could be changed easily by replacing the laser diode with another one while maintaining the rest of the configuration. Detectors should also be changed accordingly when needed.

Compared with the scatterometer at National Institute of Standards and Technology (NIST), which is only for in-plane BRDF measurement [98], this three-axis automated scatterometer (TAAS) offers the off-plane measurement capability and has resulted in multiple research works [57, 99-101]. Nevertheless, there are some problems that needs to be pointed out. The spectral range of this scatterometer is indeed limited by the wavelength tunability of the light source. Monochromators with tungsten-halogen lamp offers broader range, as shown in the previous equipment, but does not offer high enough intensity, such that the scattered light is too weak to be picked up. Also, as to be discussed later in Chapter 6, R_{dh} and T_{dh} can be obtained by integrating BRDF and BTDF over the hemisphere, respectively, based on their definition. But it has be shown by multiple researchers that the values measured yields a bias of around 5% [43, 57, 93]. Last but not least, due to the sample holder being used, samples with thin and flexible texture tend to have larger uncertainty due to surface bending, especially at large incident angles.

CHAPTER 4

RADIATIVE PROPERTIES OF SEMITRANSPARENT CERAMIC PLATES

This chapter provides an experimental and theoretical study on the radiative properties of three dense refractory ceramic plates: Al_2O_3, AlN and Si_3N_4. By examining the d-h and specular transmittance and reflectance, information such as the optical constants, volumetric scattering, porosity and surface roughness can be obtained. The sample characterization and experimental methods are introduced first, then the measured spectra are interpreted qualitatively. Mie scattering theory is applied to provide quantitative information on the porosity and scatterer size of Al_2O_3 and AlN plates, while Lorentz oscillator model is used to obtain the optical constants of Si_3N_4. Knowledge gained from this study may facilitate the heat transfer analysis in high temperature refractory systems, and also help understand the light scattering in such dispersed medium.

4.1 Sample Characterization and Experimental Method

Dense ceramic plates of Al_2O_3, AlN and Si_3N_4 were purchased from MTI Corporation (Richmond, CA), with the lateral dimensions being 50 mm by 50 mm. Both the Al_2O_3 and AlN samples are tape cast with a nominal thickness of 0.5 mm. The hot-pressed Si_3N_4 sample is about 1.5 mm thick. These samples are relatively pure with greater than 99% purity and their densities very close to the bulk counterparts. Despite the high purity, Al_2O_3 and AlN are translucent rather than transparent, due to the light scattering produced by grain boundaries and less than 1% impurities. The Si_3N_4 specimen of 1.5 mm is opaque and dark in the whole measured spectral region. Each of samples has two

different surface conditions, one side is relatively smooth and the other is relatively rough. Images and roughness of both sides of each specimen was measured using an Olympus LEXT OLS4000 3D laser confocal microscope, presented in Figure 4.1. One can see an obvious contrast between the smooth and rough sides, and the average grain size of AlN sample can be estimated to be about 3 μm to 5 μm. The grain sizes for Al_2O_3 and Si_3N_4 specimens are expected to be less than 1 μm. Table 4.1 summarizes the specimen composition, purity, density, fabrication method, and root-mean-square (rms) surface roughness [96].

Table 4.1. Sample description including fabrication method, purity, thickness, density, and typical root-mean-square (rms) surface roughness on each side.

Material	Fabrication method	Purity	Thickness (mm)	Density (g/cm^3)	Smooth side σ_{rms} (μm)	Rough side σ_{rms} (μm)
Al_2O_3	Tape cast	99.6%	0.51	3.87	0.017	0.32
AlN	Tape cast	99%	0.53	3.26	0.027	1.09
Si_3N_4	Hot pressed	99.95%	1.51	3.26	0.028	0.19

The directional-hemispherical reflectance and transmittance of the specimens were measured by the monochromator with an integrating sphere introduced in Chapter 3. The measurement was from 0.4 μm to 1.8 μm with 0.02 μm increment. Since the polished surfaces produce a significant portion of specular reflectance, a tilted sample holder was utilized to measure the specular plus diffuse reflectance components. Diffusely reflected

component were measured using a vertical sample holder. The specular reflectance for the smooth surface of each specimen, represented by R_{sp}, can be obtained from the difference of the reflectance measured with the sample holder that is titled R_{tilt} or vertical R_{vert}, so the specular component is obtained by $R_{sp} = R_{tilt} - R_{vert}$. For the rough side, the specular component is negligibly small, and the measured d-h reflectance is based on the average of R_{tilt} and R_{vert}.

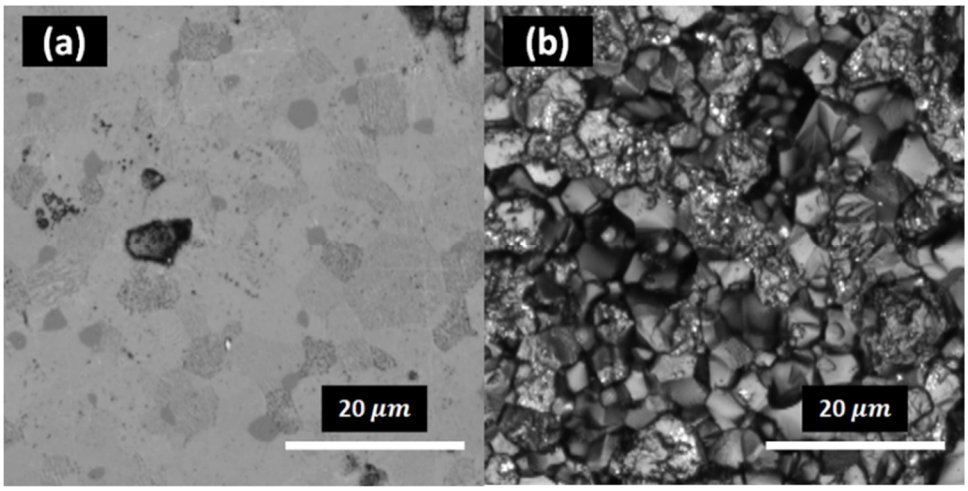

Figure 4.1. Confocal microscope images of (a) the smooth side and (b) the rough side of the AlN ceramic sample.

The near- and mid-infrared transmission and reflectance of each sample were measured with the FTIR from 630 to 6000 cm^{-1} (wavelengths from about 15.9 μm to 1.67 μm) using the gold-coated integrating sphere with the MCT detector. A tilted sample holder is used along with the diffuse gold standard, which has a reflectance of 0.95 and nearly independent of the wavelength according to the manufacture. The open beam (background) is taken when no sample or reference is mounted in the sample holder, which is corrected

in the data reduction process according to Eq. (3.2). For measurement of the d-h transmittance, the sample is placed at the front port while the backport is covered with the diffuse gold standard. Specular reflectance is measured with the same FTIR spectrometer using a 10° specular reflectance accessory and a DTGS detector, from about 500 to 6000 cm^{-1} (wavelengths from about 20 μm to 1.67 μm). The sample is placed on top of a set of mirrors so that only specular reflection can be captured. The measurement is related to a gold reference mirror, the reflectance of which can be calculated using the optical constants of gold (around 0.985) and corrected to obtain the sample reflectance [102]. The specular transmittance at normal incidence was also measured using the FTIR setup and the DTGS detector without the integrating sphere.

4.2 Measurement Results and Interpretations

4.2.1 Visible and Near-Infrared Radiative Properties

The directional-hemispherical reflectance and transmittance of the Al_2O_3 plate measured by the monochromator and integrating sphere are plotted in Figure 4.2(a), along with the specular reflectance determined from experiment R_{sp} and model R_{model}. It is shown that the sum of the directional-hemispherical reflectance and transmittance is close to unity, suggesting that absorptance, $\alpha = 1 - R_{dh} - T_{dh}$, is negligible in the concerned wavelength range. R_{sp} can be compared with theoretical estimation based on Fresnel's reflection formula at the interface between air and a semi-infinite medium. At normal incidence, the model reflectance is [7]:

$$R_{model} = \frac{(n-1)^2 + \kappa^2}{(n+1)^2 + \kappa^2} \tag{4.1}$$

where n and κ denote the refraction index and extinction coefficient, respectively, taken from Ref. [8]. The experimentally obtained specular reflectance agrees well with the reflectance from the model near the wavelength $\lambda = 1.8$ μm, but decreases towards shorter wavelengths due to surface scattering even though the rms roughness is 17 nm only, which also indicates that surface roughness is negligible beyond 1.8 μm.

Considering the multiple reflectance from the top and bottom surface, for a Al_2O_3 plate with perfectly smooth surfaces, it is expected that $R_{dh} \approx 2R_{sp}$. Even considering the surface roughness, R_{dh} should not change significantly since the absorption is negligible. Therefore, the large R_{dh} shown in Figure 4.2(a) is from diffuse reflection caused by volume scattering, which may come from scattering by impurities, pores and grain boundaries.

The measured reflectance and transmittance of AlN is shown in Figure 4.2(b,c), with the optical constants taken from Ref. [16]. Unlike Al_2O_3, the absorptance of AlN is non-zero, but increases toward shorter wavelengths, especially in the visible region. This could be caused by the increased absorption toward the bandgap along with the enhanced volume scattering at shorter wavelengths. The increased volume scattering also causes the decrease of both R_{dh} and T_{dh}. Similar to Al_2O_3, surface scattering is also stronger at short wavelengths as seen by the smaller R_{sp}. Note that the volume inhomogeneity of AlN is the largest among the three samples with about 1 % impurities, which might cause some deviation from the refractive index obtained from AlN crystals.

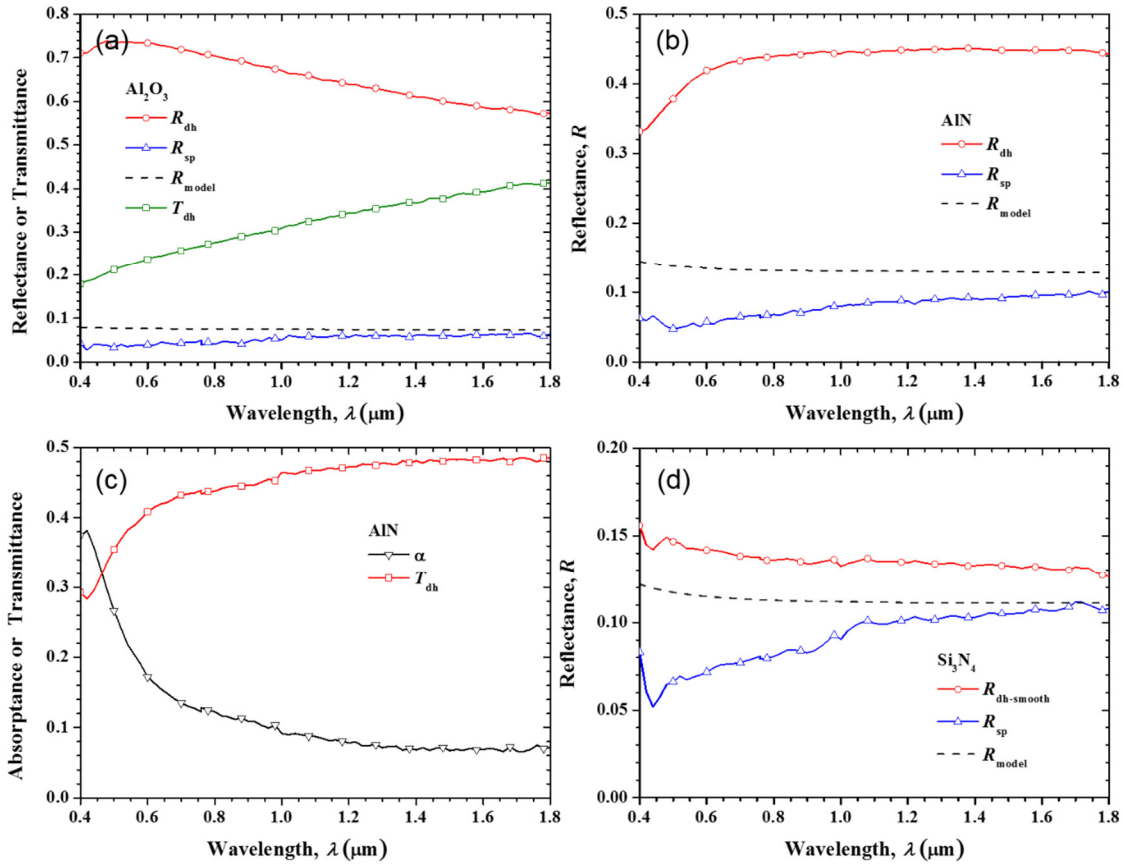

Figure 4.2. Radiative properties of the three samples in the visible and near-infrared region measured with the monochromator and integrating sphere: the directional-hemispherical and specular reflectance for (a)Al_2O_3, (b)AlN and (d)Si_3O_4, the calculated specular reflectance from the surface reflection model is also shown together; (c) absorption and transmission of AlN sample.

Si_3N_4 plate appears dark gray and opaque and no transmittance is obtained, as shown in Figure 4.2(d). Surface scattering can also be observed on the sample by the difference of R_{sp} and R_{model}, which is taken from Philip [18]. Note that R_{dh_smooth} follows the trend of R_{model} and increases slightly towards short wavelength due to change

of refractive index. The difference is attributed to volume scattering which has enhanced diffuse reflectance. Compared to the other samples, volumetric scattering is much weaker. For a surface without volume scattering, R_{sp} varies with surface roughness but R_{dh_smooth} should remain close to R_{model}.

4.2.2 Near- to Mid-Infrared Radiative Properties

Figure 4.3(a,b) shows the R_{dh}, T_{dh}, R_{sp}, T_{dh} measured with FTIR for Al_2O_3. Note that the reflectance varies with the surface roughness and they are plotted separately for the relatively smooth and rough surface, while the transmittance is the same for both surfaces. A closer up view of the phonon (absorption) band, also called the reststrahlen band, is also plotted from about 500 cm^{-1} to 900 cm^{-1}, when the extinction coefficient κ is large, and the reflectance is very high. The Christiansen wavelength is observed at the edge of the band, at approximately 1038 cm^{-1}, where the reflectance approaches to zero and the absorptance is close to unity. The difference of reflectance between the smooth and rough surfaces can be clearly seen within the phonon band. This can be understood from the effective medium approximation, where the roughness region behaves as an effective antireflection layer. For incidence on the same surface, the specular reflectance R_{sp} is somewhat lower than that of the directional-hemispherical reflectance R_{dh}. This may be attributed to a small amount of volume scattering, though uncertainties in the measurements may account for some of the differences. Beyond the reststrahlen band and in the higher wavenumber region $1500\ \text{cm}^{-1} < \nu < 6000\ \text{cm}^{-1}$, R_{dh} for both sides is very close and much higher than R_{sp}, which suggests that volume scattering plays a significant

role or even dominates the radiative properties in the short wavelength region. This can also be observed by examining T_{sp} and T_{dh}.

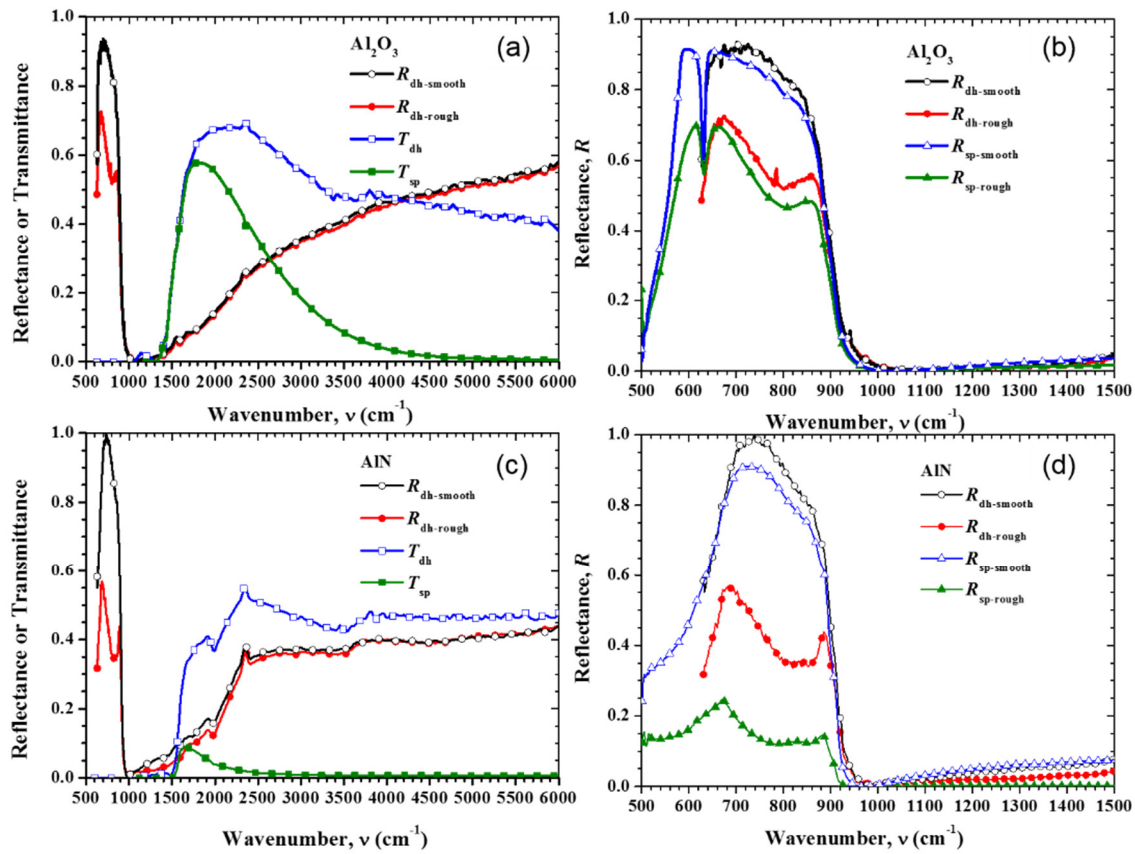

Figure 4.3. Radiative properties of the Al_2O_3 and AlN in the mid-infrared region measured with FTIR: (a,c) the directional-hemispherical reflectance and transmittance along with the specular transmittance, at wavenumbers from 630 cm ^{1} to 6000 cm ^{1}; (b,d) comparison of the specular and directional-hemispherical reflectance for both sides from 500 cm ^{1} to 1500 cm ^{1}.

At wavenumber $\nu > 1700\ \mathrm{cm}^{-1}$, T_{sp} decreases exponentially when T_{dh} remains relatively stable, indicating a transition from surface to volumetric scattering, the same conclusion obtained in analysis the VIS to NIR data. Note that in the overlap region of these two sets of equipment, the measured data has achieved good agreement.

The radiative properties of AlN is also shown in Figure 4.3(c,d) with similar features. The reststrahlen band and Christiansen wavelength (at about 1028 cm ^{1}) can also be observed. Note that the roughness causes significant reduction of reflectance in the reststrahlen band on the rough side due to relatively larger roughness compared with Al_2O_3. Beyond the phonon band where the volume scattering is dominant, the d-h reflectance from the two surfaces is very close. T_{sp} drops to zero more quickly at larger wavenumbers due to the stronger scattering and absorption.

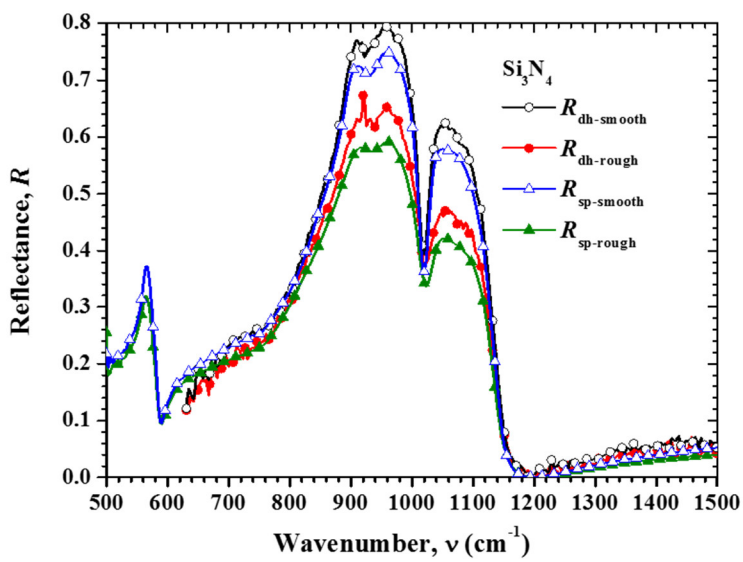

Figure 4.4. The directional-hemispherical reflectance and the specular reflectance of the Si_3N_4 sample from 500 cm ^{1} to 1500 cm ^{1}

R_{dh} and R_{sp} for the two sides of Si_3N_4 is plotted in Figure 4.4. The phonon features in Si_3N_4 are more complicated due to involvement of more atoms in a unit cell and thus more lattice vibration modes. However, the main phonon bands observed are in reasonable agreement with the literature for amorphous Si_3N_4 film and ceramic samples [18-20, 22], with a much higher reflectance value. The Christiansen wavelength is at 1201 cm^{-1}, beyond which both R_{dh} and R_{sp} slowly increase, and the smooth side is slight higher than the rough side due to surface scattering. Since the Si_3N_4 plate has higher purity and stronger absorption, volume scattering plays a less important role compared with the other two samples. The detailed band structure will be fitted in the following section using Lorentz oscillator model.

4.3 Theoretical Modeling

4.3.1 Scattering and Absorption Coefficient

Before further analysis of the light scattering and transport inside the medium, it is necessary to connect and smooth the data obtained from measurements. Polynomial functions are used to smooth the relatively high noise in the FTIR measurement by splitting the spectrum into several regions so that suitable weight can be intentionally placed to remove some artifacts and noises. The purpose of using the polynomial fit is to capture the main scattering and absorption properties of the sample without paying too much attention to the details, so some defects from water vapor and CO_2 absorption are neglected, such as absorption band caused by the adsorbed moisture in the sample due to O–H bonds. A final fitting is performed that combines the monochromator data and FTIR data using a

polynomial function of up to nine orders for the reflectance or transmittance. Then the scattering and absorption coefficients are calculated from the IAD code developed by Prahl [61]. It has been shown that volume scattering dominates the radiative properties in the semitransparent region for the samples studied, in addition, the d-h properties are not affected, therefore the flat surface approximation in the IAD method is valid in this analysis.

The scattering and absorption coefficients obtained from IAD method is presented in Figure 4.5. The IAD extraction becomes unreliable beyond $\lambda = 2$ μm due to the very low R and T of the sample. As expected, the scattering coefficient σ decreases but the absorption coefficient α increases as the wavelength increases. In the visible region, the scattering coefficient is very high (~20 mm ^{1}) and the scattering albedo is close to 1. The absorption effect begins at about 3 μm and increases quickly as the wavelength increases to beyond 5 μm. This significant volumetric scattering could be caused by impurities, grain boundaries and pores. Given the high purity of the Al_2O_3 sample exceeding 99.6%, only scattering by pores is considered. Various pore size and concentration are tried based on the estimation from the confocal microscope images, the calculated scattering coefficients from Mie theory are plotted in Figure 4.5 (a). A smaller pore size tends to give higher scattering coefficient at shorter wavelengths but drops off very fast toward longer wavelengths, while a larger size gives a good agreement in the near- and mid-infrared region but not as high as the IAD results in the shorter wavelengths. By combining these two pore sizes with the corresponding concentration, the scattering coefficients obtained by the IAD method and the Mie scattering calculations agree reasonably well. The overall porosity is within 2%, agreeable with the prediction from confocal images.

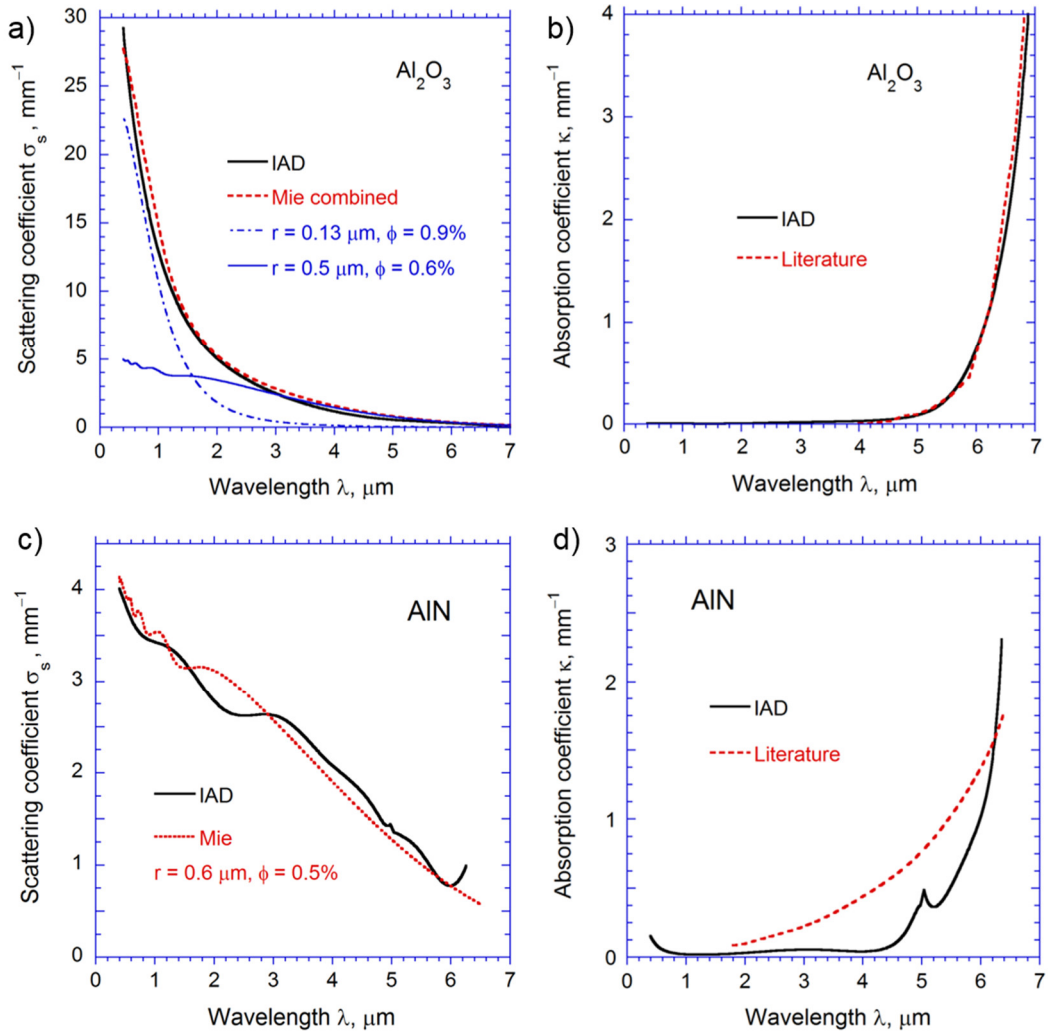

Figure 4.5. Scattering and coefficient of Al_2O_3 and AlN: (a,c) the retrieved values from IAD method compared with the prediction made by Mie theory, the radius and concentration of the pores are indicated on the plot, note that two types of pores are used for Al_2O_3; (b,d) the absorption coefficient obtained from IAD method and from the imaginary part of the refractive index, taken from Tropf and Thomas [9] for Al_2O_3 and Moore et al. [15] for AlN.

Unlike scattering coefficient, the absorption coefficient from Mie theory prediction are for absorbing particles. But in the current study the absorption mainly comes from the medium, not the air pores. Instead, the absorption coefficients could be deduced from the optical constants by [7]: $\alpha = 4\pi\kappa / \lambda$, as shown in Figure 4.5(b). It can be seen that the absorption coefficient calculated from the literature [9] for $\lambda > 4$ μm agrees well with that obtained from the IAD. The exponential increase in the absorption coefficient can be understood as due to multiphonon absorption. The slight deviation may be attributed to the sample difference and the inaccuracy of the extraction method used here in the region where both the *R* and *T* are low.

Similar approach was performed on the AlN sample and the results are shown in Figure 4.5(c,d). Since the optical constants obtained from literature fails to the match with the sample studied, a Lorentz model fitting was first performed to obtain the dielectric function for wavelength range $\lambda > 1.75$ μm , as to be introduced later. In the region $0.4\ \mu\text{m} < \lambda < 1.75\ \mu\text{m}$, it is found that the ceramic material may have a somewhat lower refractive index than single-crystal AlN, caused by the impurities and the variation in crystalline structure. Thus the refractive index is obtained by subtracting 0.2 from the compiled values [16] in this range. It should also be noted that the back side of the AlN sample has an rms roughness of about 1 μm. This relatively high roughness may impact the smooth surface model used in the IAD calculation.

By assuming air pores with r = 0.6 μm and ϕ = 0.5 %, the scattering coefficients predicted by the Mie theory appear to follow the similar trend as those obtained from the IAD method. Some wavy features in the Mie prediction can be removed by considering a

particle size distribution, though it was not done here for simplicity. The IAD method also shows wavy feature, which might come from the impurity and large grain size (3~5 μm). The absorption coefficient calculated from κ values from Moore et al. [15] are plotted against the values retrieved from IAD, and it tends to overpredict at short wavelengths due to the use of Lorentz model. Overall, the trend of the retrieved scattering and absorption coefficient are successfully modeled with Mie theory and the extinction coefficient data, while the agreement is not as good as in Al_2O_3 due to large impurity (1%). Other reasons for the disagreement of these two methods may be scattering by grain boundaries with much large size parameters or by non-spherical scatters. The scattering coefficient for AlN is about 6 times lower in the visible region, while the absorption coefficient of AlN is higher in the visible, about 3 μm, and beyond 4.6 μm, compared with those of Al_2O_3. The larger scattering coefficient of Al_2O_3 as observed and discussed in previous section comes from much smaller pores ($r = 0.13\ \mu\text{m}$) compared with AlN ($r = 0.6\ \mu\text{m}$), based on the Mie prediction, which is also in reasonable agreement with the different microstructures of these two ceramic materials.

4.3.2 Lorentz Oscillator Model

The Lorentz oscillator model is used to predict the dielectric function of AlN and Si_3N_4 samples in the near- and mid-infrared regions. This model treats each discrete vibration mode as a classical damped harmonic oscillator, and frequency-dependent complex dielectric function can be written as a superposition of individual contributions [7]:

$$\varepsilon(\omega) = \varepsilon_\infty + \sum_{j=1}^{N} \frac{S_j \omega_j^{\,2}}{\omega_j^{\,2} - \mathrm{i}\gamma_j \omega - \omega^2} \tag{4.2}$$

where ε_∞ is a high-frequency constant, ω_j is the resonant frequency, γ_j is the damping or scattering rate, and S_j is the oscillator strength. For a model with N Lorentz oscillators, the number of unknowns is $3N+1$. The steepest ascent hill climber algorithm is used to perform a regression analysis of the specular reflectance of the smooth side of the sample as done in a previous study [103]. The fitting is performed by minimizing the standard error of estimate (SEE), defined as:

$$SEE = \sqrt{\frac{1}{M-1} \sum (\mathrm{R}_{\mathrm{meas}} - R_{\mathrm{calc}})^2} \tag{4.3}$$

where the subscripts "meas" and "calc" refer correspondingly to the measured and calculated values, and M is the number of data points from the measurements. The calculated reflectance is based on the specular reflectance in Eq. (4.1) and then compared with the specular reflectance measured to deduce the *SEE*.

Although AlN crystals are slightly anisotropic due to its wurtzite structure, the AlN sample studied in this work is polycrystalline ceramic with random crystalline orientation, thus a single oscillator is used to model the dielectric function without considering the anisotropic effect. The optimized *SEE* is slightly above 0.01, well below the uncertainty in the specular reflectance measurement of 0.02. The good agreement between measured and fitted reflectance spectra is shown in Figure 4.6(a) for AlN. The uncertainty for resonance frequency is within 3% while the other parameters are about 10%. Some noticeable difference occurs at longer wavelengths beyond 12 μm, where resonance frequency is reasonable, but strength might differ, giving a slightly smaller reflectance as

measured. In addition, the measured reflectance curve seems to have narrower shoulder at the resonate frequency, which could come from the birefringence of AlN [15]. The fitted parameters are listed in Table 4.2 as below.

Table 4.2. Lorentz fitting parameters for the AlN and Si_3N_4 specimens; the uncertainty in the resonance frequency is estimated to be within 3% while the typical uncertainty of the other parameters is estimated to be 10%.

	ε_∞	ω_j (cm^{-1})	S_j	γ_j (cm^{-1})
AlN	3.71	657	3.34	23.5
Si_3N_4	3.67	1034	0.0861	42.9
		935	0.0684	27.4
		890	1.88	37.8
		569	0.294	16.8

Compared with literature, either AlN crystal [14] or thin films made from vapor phase epitaxy [15] , the values and trend reported in this work agree well, with the resonance frequency corresponds to the transverse optical phonon mode in these publications. The main difference is the larger scattering rate reported here, 23.5 cm^{-1} compared with 2.2 cm^{-1} in Ref. [15], which leads to a lower peak in both n and κ as shown in Figure 4.6(b,c). As mentioned previously, the impurity of this sample is around 1%, which causes the high scattering rate.

Figure 4.6(d) shows fitting result for Si_3N_4, in which strong phonon resonances are modeled using four oscillators in the ceramic Si_3N_4. The obtained refractive index and extinction coefficients are plotted against literature in Figure 4.6 (e) and (f), respectively. Samples studied by previous research are mostly thin films that are amorphous with broadband phonon features, but the phonon structures are difficult to distinguish [19, 20, 104]. But purity of this Si_3N_4 exceeds 99.95%, giving rise to strong phonon resonances as demonstrated in the measured reflectance. Compared with the published experiments [105] and first-principle simulation [106], the infrared active phonon modes can be identified based on β-Si_3N_4. There are six infrared active phonons but two of them are located below 500 cm^{-1} ($\lambda > 20$ μm). The resonance frequencies of the four phonon modes obtained from this work fall between the values given in Refs. [105, 106]. There exist some discrepancies in the measured and fitted reflectance at $\lambda = 18$ μm, which might be due to the exclusion of the longer wavelength phonon resonators. The strong phonon resonances are attributed to the high-density, high-purity polycrystalline structure and, to our knowledge, the detailed infrared phonon parameters and dielectric function of crystalline Si_3N_4 have not been reported elsewhere. Knowledge of the infrared phonon behavior and optical constants may benefit future applications of dense Si_3N_4 ceramics.

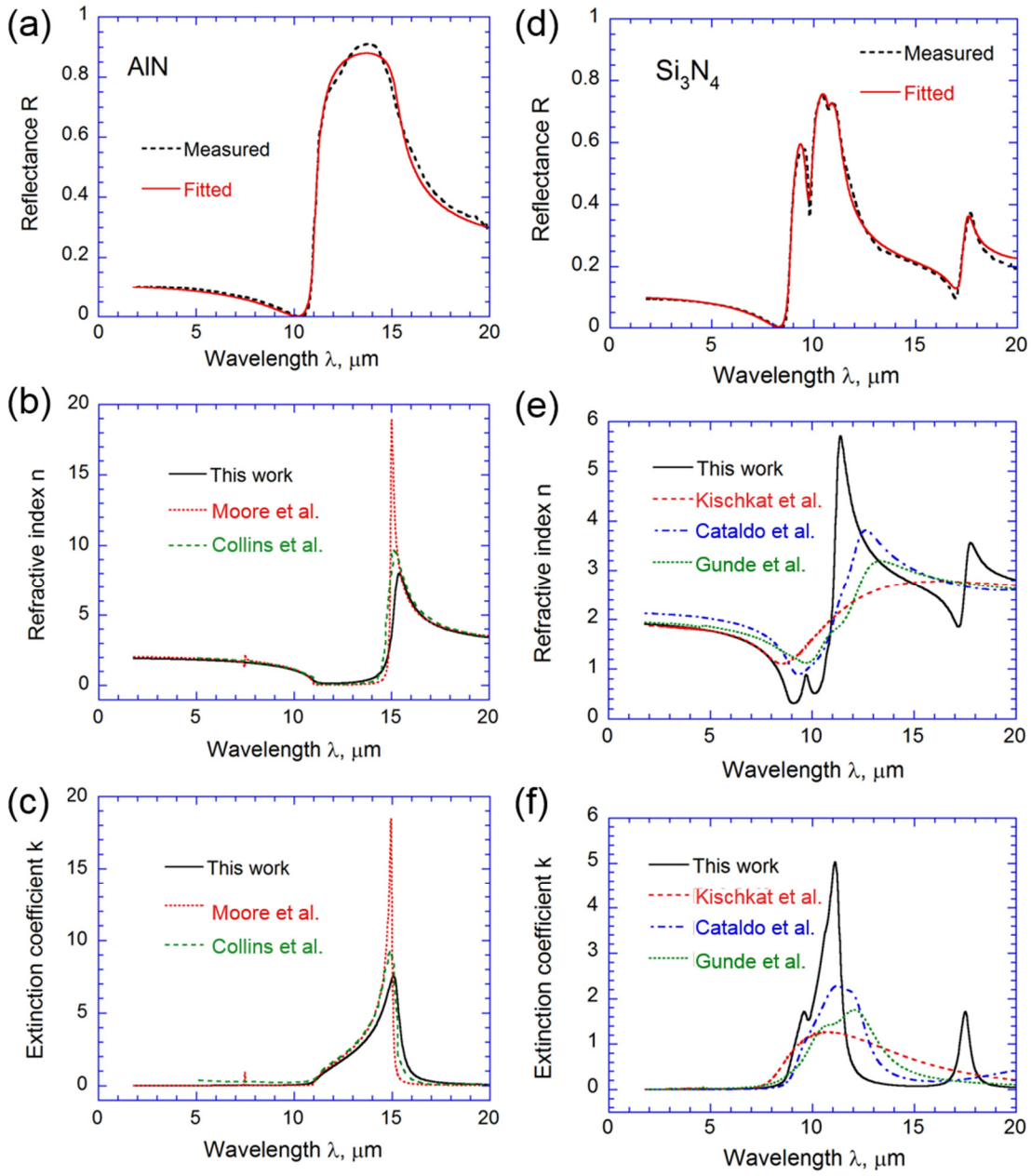

Figure 4.6. Lorentz fitting results for AlN and Si_3N_4: (a,d) comparison of measured and fitted reflectance; (b,e) real part of the refractive index *n*; (c,f) imaginary part of the refractive index κ, the optical constants are also compared with literature values indicated in the labels.

CHAPTER 5

ULTRA-HIGH SOLAR REFLECTANCE

Passive radiative cooling takes advantage of the atmospheric transmission window from 8 μm to 13 μm [68] to emit thermal radiation into deep space. To achieve radiative cooling under the direct sunlight requires not only a high infrared emissivity, but more importantly, a high reflectance in the solar irradiation range from 0.28 μm to 4 μm [69]. In this chapter, a dual-layer structure focusing on enhancing the solar reflectance is proposed, which consists of a sintered polymer sheet atop a thin silver film. The design of the dual-layer structure was introduced first, along with the measurement method. Then the measured results are presented to show the record-high solar reflectance. In addition to the high directional-hemispherical reflection, this structure also produces diffuse reflectance favorable to real system, which will also be measured and discussed. The mechanism for this high diffuse reflectance will be interpreted using different models, and the details of the Monte Carlo model used will be covered in the next chapter. Finally, theoretical calculations demonstrate the radiative cooling performance under ideal circumstances.

5.1 Design and Measurement Method

Sintered polytetrafluoroethylene (PTFE) is a white material of extremely high diffuse reflectance from ultraviolet to near-infrared (0.2~2.5 μm wavelength). It has been used as the inner coating of integrating spheres and diffuse reflectance standard [80, 81], usually with a thickness of 10 mm to achieve opacity, which is not practical for large scale applications. It is imperative to reduce the thickness while blocking the transmittance. On the other hand, silver (Ag) has a plasma frequency in the ultraviolet, thus possesses high

reflectance in most of the solar spectrum from visible to near infrared. The absorption of Ag near plasma frequency can be negligible if the ultraviolet radiation is efficiently reflected. Thus, by placing a layer of PTFE sheet on top of Ag, the high ultraviolet reflectance of PTFE can be combined with the high near infrared reflectance of Ag film, and overall solar reflectance can be maximized. It is worth mentioning that the selection of PTFE is due to its exceptional reflectance performance which comes from its porous and highly scattering nature. Researchers have tried using other particles with highly scattering properties to achieve radiative cooling, such as SiO_2 [70], TiO_2 [65, 73], and more recently a similar polymer named poly(vinylidene fluoride-co-hexafluoropropene) (P(VdF-HFP)$_{HP}$) [76], but none of them demonstrates a solar reflectance higher than the present work. It is not clear though, if the dual-layer structure could also work by replacing the PTFE film with some paint made by these particles. But the integrity and availability of sintered PTFE films are better than other candidates.

Sintered PTFE sheets with three different thicknesses were purchased from a commercial vendor, referred to as Samples A, B, and C with nominal thicknesses of 0.24 mm, 0.5 mm, and 1 mm. A 10-mm-thick PTFE slab was used as a reflectance standard for measurements at wavelengths from 0.28 μm to 1.8 μm using a monochromator; its reflectance is assumed to be the same as that reported by Weidner and Hsia [81] at each corresponding wavelength. For comparison, the 10-mm-thick PTFE slab is referred to as Sample D, whose transmittance is negligibly small.

Table 5.1. Measured properties of PTFE sheets.

Sample	A	B	C
Thickness (μm)	236±4	500±6	993±6
Density (g/cm^3)	1.67±0.05	1.58±0.05	1.65±0.05
Surface roughness (μm)	3.7±0.4	3.5±0.4	3.2±0.4

The surface morphology of the PTFE sheet was characterized with a scanning electron microscope (SEM) Hitachi S-3700N, as displayed in Figure 5.1(a) [52]. Since PTFE is not an electrical conductor, the surface of the PTFE was coated with a 300-nm-thick Ag layer using E-beam evaporation. It can be seen from the SEM image that the PTFE sample contains cracks, porosity, and soft fibrous structures. The surface roughness was estimated with an Olympus LEXT OLS40 00 3D laser confocal microscope to be between 3 μm and 4 μm, as shown in Figure 5.1(c). The peak-to-peak roughness is relatively large due to the textile structure and potential artifacts caused by the strong scattering. Note that the spatial variation of surface roughness on all three samples is not significant, and the autocorrelation length is also measured with the confocal microscope to be between 20 μm and 30 μm. A photo of the white PTFE sheet is illustrated in Figure 5.1(b). Using a micro-balance and sample dimension measurements, the densities of three samples are estimated to be around 1.6 g/cm^3, which is slightly lower than the values reported by Li et al. [57]. The density and surface roughness of each sample are also listed

in Table 5.1. The density for Sample D was reported by Li et al. [57] as 1.52 g/cm^3, which is the lowest of all samples.

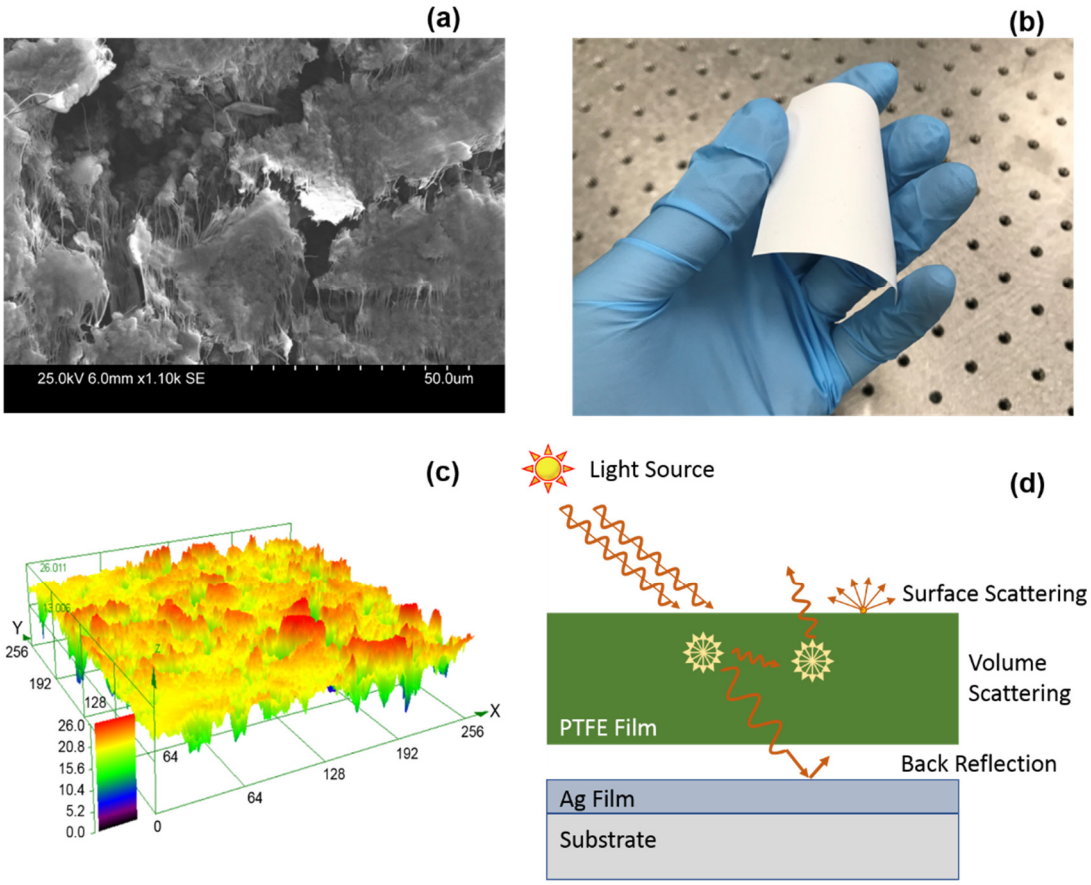

Figure 5.1. (a) SEM image of the PTFE surface coated with a 300-nm-thick Ag layer; (b) a photo of the PTFE sheet; (c) confocal microscope image; (d) schematic of the dual-layer structure, where surface scattering and volume scattering component are illustrated. Note that the Ag film is coated on a substrate and it is assumed that an air gap exists between the PTFE sheet and the Ag film.

The proposed dual-layer structure is shown in Figure 5.1(d). A thin PTFE sheet is placed on top of a silver (Ag) layer. To avoid absorption, no adhesives are applied between the two layers and they are mechanically held together, resulting a natural gap of air. The

Ag film was E-beam evaporated onto a glass substrate. A 1-μm-thick silver film was used to avoid possible wear during repeated measurements, though a 200 nm thickness is generally considered to be sufficient [7]. It is interesting to note that attempts are made by depositing Ag film by E-beam evaporation directly on one surface of the PTFE sheet. As it turned out, the reflectance for incidence on the uncoated PTFE surface was reduced. Due to the surface morphology of the PTFE, deposited Ag forms clusters and causes more absorption and result in a deterioration of the spectral reflectance. Improvement in the binding method of the dual-layer structure could be made.

Both the monochromator with integrating sphere and the FTIR with integrating sphere were used to measure R_{dh} and T_{dh} of the samples. Wavelength range from 0.28 μm to 1.8 μm was measured with the monochromator with an estimated uncertainty of within 0.01, except for the shorter wavelength region when $\lambda < 0.40$ μm . The measured reflectance was corrected based on the reflectance of the standard 10-mm-thick PTFE (Sample D) according to Ref. [81]. T_{dh} is obtained as $T = 1 - R$ to avoid the larger uncertainty in the transmittance measurement. Since the samples are diffuse, all the measurements are for near-normal incidence.

Measurement in the near- to mid-infrared region was performed on the FTIR with MCT detector, with a resolution of 4 cm^{-1} and averaged over 256 scans to improve the signal-to-noise ratio. The data are smoothed by averaging 51 near-by points and presented with a wavelength interval of about 20 nm. The reflectance of Sample D is also measured, which agreed well with literature in the overlapped region. The uncertainties of the measurements at wavelengths from 2.0 μm to 3.5 μm are estimated to be 0.01 and 0.02

respectively. At wavelengths longer than 3.5 μm, the reflectance of PTFE drops quickly, and the measurement uncertainty is estimated to be 0.02 according to Yang et al. [107].

5.2 Results and Applications for Radiative Cooling

5.2.1 Directional-hemispherical Reflectance

Figure 5.2 (a) and (b) shows the measured directional-hemispherical reflectance and absorptance of PTFE samples in the solar spectral region from 0.28 μm to 4 μm. Note that all properties presented in this study were measured at room temperature 295 K. The absorption is calculated from $A = 1 - R_{\mathrm{dh}} - T_{\mathrm{dh}}$, and below 1.8 μm it is taken to be zero. It is shown that in general, the thicker the PTFE sheet, the higher its reflectance gets. The absorption bands can be seen from the reflectance curve at around 2.84 μm, 3.42 μm, and 4.24 μm (not shown here due to the cutoff wavelength of 4 μm). They are better visualized in the absorption plot, where the thicker the PTFE, the stronger the absorption becomes. The weak absorption bands near $\lambda = 2.1$ μm and $\lambda = 2.4$ μm are barely observable in the thin PTFE sheets. In the short wavelength end, there appears to be an abrupt drop of reflectance for $\lambda < 0.34$ μm. This may be caused by the absorption of PTFE in the ultraviolet (as also indicated by the reduction of reflectance for Sample D) as well as the uncertainty near the instrument's spectral limit.

When the PTFE sheets are backed with a Ag film, Sample A, the thinnest sample with lowest reflectance, is boosted to be the one with the largest reflectance, as shown in Figure 5.2(c). In the wavelength region from 0.4 μm to 1.7 μm, where 92.5% of solar irradiation is concentrated [69], the reflectance for all three samples exceeds 0.99. At $\lambda > 1.7$ μm, the absorption gradually increases, resulting in a reduction of the reflectance.

Since the Ag reflector helps boost additional multiple scattering events in the PTFE sheet, some weak absorption bands can now be seen in the spectra of Samples B and C, near $\lambda = 2.1$ μm and 2.4 μm, but remain undiscernible for the thinnest sheet (Sample A).

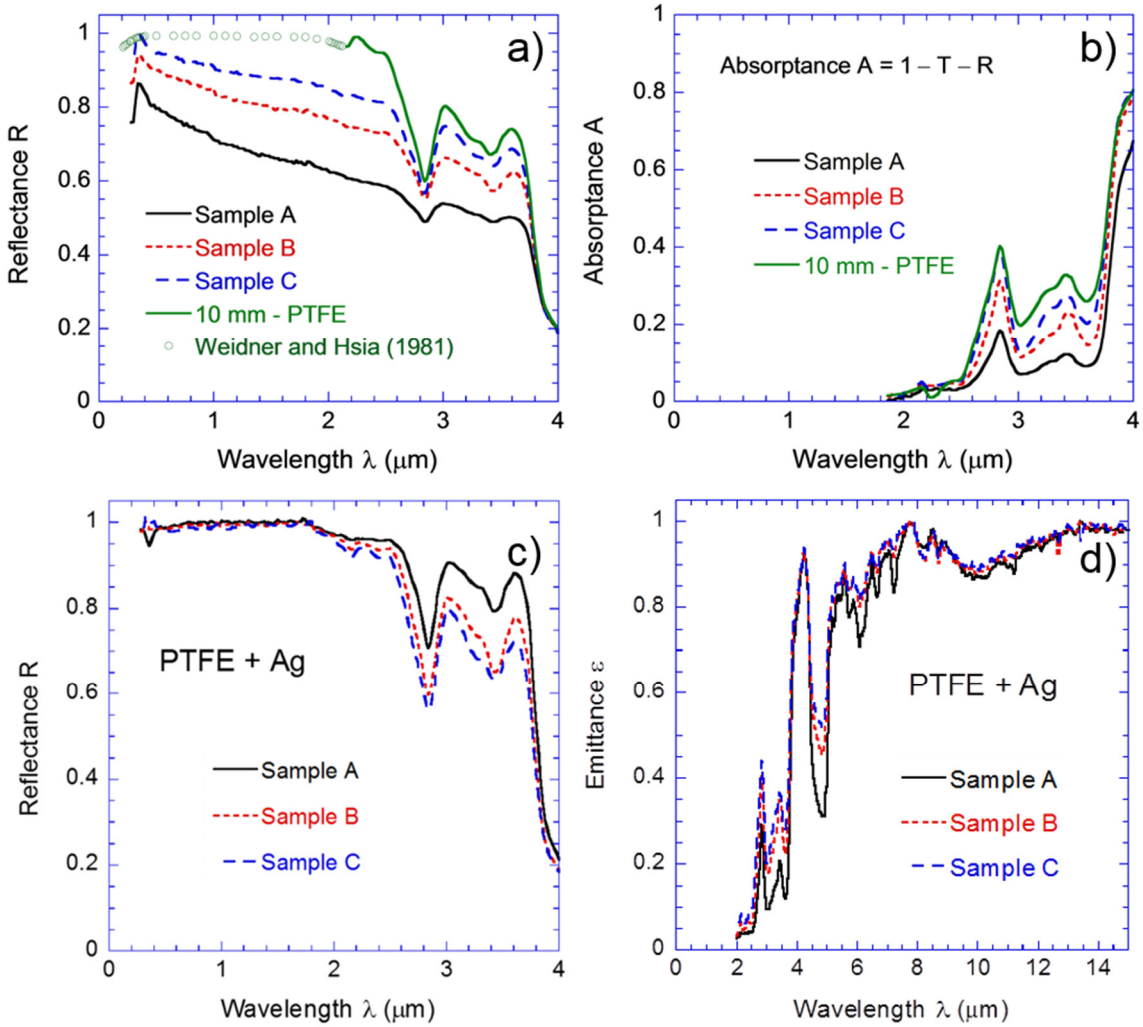

Figure 5.2. (a) Reflectance and (b) absorptance of the PTFE sheets and the 10-mm slab for 0.28 μm < λ < 4 μm. The reflectance of Sample D is taken from Weidner and Hsia [81] at wavelengths shorter than 2.1 μm. The absorptance at λ < 1.8 μm is assumed to be zero for all samples; (c) reflectance of the dual-layer structures with PTFE sheets on the Ag film; (d) spectral emittance of the dual-layer structure with different PTFE thicknesses at wavelengths from 2 μm to 15 μm.

The fact that Sample A exhibits the highest among all three dual-layer samples can be explained in following modeling section. In brief, the thinnest sample has the smallest absorption due to multiple scattering enhanced with the Ag film. Beyond 2.4 μm, the reflectance of Sample A in the dual-layer structure is higher than that of Sample D (without Ag reflector), although the fraction of solar radiation is only 1.1%. This result clearly demonstrates that using the dual-layer structure can enhance the solar reflectance with much less PTFE material. In the ultraviolet end, the reflectance of the dual-layer structure remains to be high even though the reflectance of Ag drops quickly towards shorter wavelength due to interband transitions. Note that if the absorption in PTFE is negligibly small, the reflectance of the dual-layer structure can be higher than the reflectance of either a free-standing PTFE sheet or a Ag film. The near- to mid-infrared emittance of the dual-layer is shown in Figure 5.2(d). All three samples have similar emittance profile and the value is high in the atmospheric transmittance window from 8 to 13 μm. This indicates a potential for radiative cooling application, as to be discussed in the calculation part.

5.2.2 Bidirectional Reflectance

The bidirectional radiative properties are measured using the optical scatterometer introduced in Chapter 3 at wavelength of 635 nm. BRDF and BTDF of free-standing PTFE samples are measured, while only BRDF is measured for the dual-layer structure. Figure 5.3 shows the BRDF and BTDF at normal incidence of all three samples, the thicknesses of which are shown in Table 5.2. The range is set from 0 to 1, but the value could be much larger than 1 for a surface with a significant specular component. For a perfectly diffuse surface with a reflectance of R, the BRDF should be a constant of R/π . There are some

fluctuations of BRDF as well as variations for the three PTFE sheets on Ag. However, the variations are insignificant and therefore a quadratic curve fitting is made for all samples as shown in Figure 5.3(a). Furthermore, the titling of the measured BRDF may be due to imperfect alignment in mounting the sample. Hence, the fitting assumes a symmetric function by setting the coefficient of the first term to zero. The standard error of estimate of the fitting is 4.7%. For free-standing PTFE, the BRDF increases while the BTDF decreases as the thickness increases. Each data set is fit to a quadratic equation and the fitted curves are also shown on Figure 5.3(b). Overall, the standard error of estimate for the fitting is within 5% for all data sets.

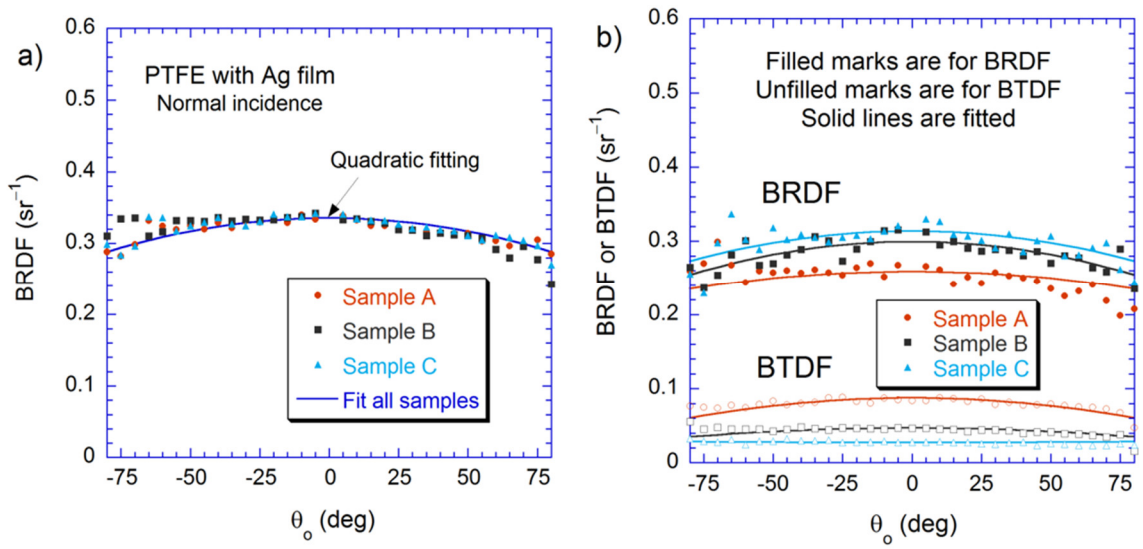

Figure 5.3: (a) The measured BRDF at normal incidence for three PTFE sheets on Ag film. All three samples are fitted with a quadratic curve as shown as the solid line. (b) The measured BRDF and BTDF at normal incidence for the three PTFE samples. The fitted values are plotted as solid lines.

Both the fitted BRDF and BTDF can be integrated to get the normal hemispherical reflectance based on their definition, by assuming no azimuthal dependence:

$$R = \int_{2\pi} \mathrm{BRDF} \cos\theta_{\mathrm{o}} d\omega_{\mathrm{o}} = 2\pi \int_{0}^{\pi/2} \mathrm{BRDF} \cos\theta_{\mathrm{o}} \sin\theta_{\mathrm{o}} d\theta_{\mathrm{o}} \qquad (5.1)$$

Table 5.2: Thicknesses and the reflectance and transmittance of all three PTFE sheets from integration of measured BRDF and BTDF (TAAS) as compared with the values from monochromator and integrating sphere (IS) measurements.

	Sample A	Sample B	Sample C
Thickness (μm)	236	500	993
R (TAAS)	0.786	0.888	0.938
T (TAAS)	0.243	0.133	0.087
R+*T* (TAAS)	1.030	1.021	1.030
R (IS)	0.755	0.884	0.922
T (IS)	0.236	0.128	0.072
R+*T* (IS)	0.991	1.012	0.994

Similarly, the transmittance *T* can be obtained by integrating over the BTDF. The results are compared with the ones measured from the monochromator with an integrating sphere, tabulated in Table 5.2 for the free-standing PTFE samples. For the three samples with Ag film, the fitted curve based on TAAS measurements is integrated, resulting in a reflectance of 0.999 (after the systematic correction as mentioned previously). The

integrating sphere measurements give an average value of 0.986. For the free-standing PTFE samples, the integrated values from TAAS measurements agree with that from the IS measurements within 4% which is within the combined uncertainties.

The measured BRDF of Sample A at incident angles of 0°, 30°, 50° and 70° are plotted in Figure 5.4, for both the PTFE sheet and the dual layer structure. No specular component was generated by placing the silver film at the back of the PTFE sample. This could also be verified by considering the profile of BTDF, which is nearly diffuse with a small magnitude. For the dual-layer structure to have a specular peak, a significant collimated transmittance is required, meaning that the BTDF should have a strong peak from the unscattered incident light. The fact that BTDF is diffuse indicates that very strong volumetric scattering alters the incident light direction and produces diffuse transmission at the back. Given the calculated scattering coefficient of 34.4 mm^{-1} from the inverse-adding doubling method [52], a PTFE thickness of roughly $1/34.4 \approx 0.03$ mm is required to observe noticeable collimated transmittance, which is ten times thinner than Sample A, and it will be proved again using the MCRT results in next chapter. For radiative cooling applications, it is desired to have strong volumetric scattering so that the thickness of the surface could be reduced and wear-resistant. It is worth mentioning that the scattering coefficient reduces as the wavelength increases for PTFE, but at the same time, the absorption coefficient increases, making it hard to observe the collimated transmittance even in the near-to-mid infrared region.

Another important message from Figure 5.4 is the emerging specular component at oblique incidence, which becomes more significant at increasing incident angles. At 50° incidence, the BRDF at the specular peak is around 0.5 and it is over 1 at an incident angle

of 70°. The specular peak is not centered at the retroreflection direction precisely, but has a shift towards larger angles. This off-specular reflectance from roughened surfaces has long been observed and reported in previous studies [57, 108, 109], which can be explained by specular reflection from the facets. Due to the increase in the specular component, the BRDF values at the non-specular direction slightly decreases as the incident angle increases.

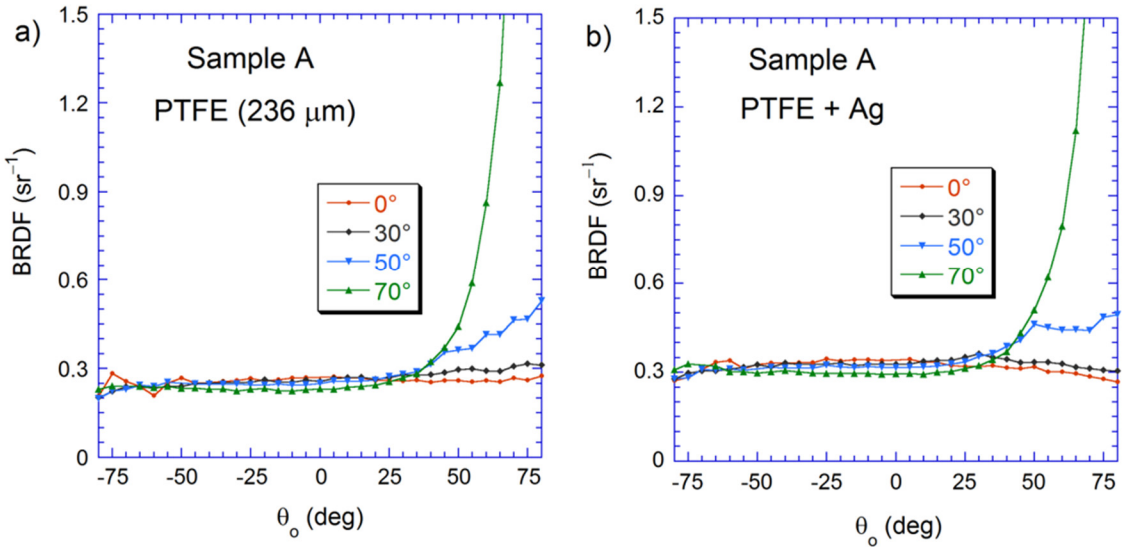

Figure 5.4. The measured BRDF as a function of the observation angle with various incidence angles for (a) Sample A PTFE only and (b) Sample A with a silver film.

Figure 5.5 shows the measured BRDF of both the PTFE and the dual-layer structure, to demonstrate the effect of the PTFE thickness on the directional radiative properties. For a single layer PTFE sheet (Figure 5.5(a,b)), Sample A has the smallest BRDF value, which corresponds to the smallest directional-hemispherical reflectance after integration; Sample C has the largest BRDF value. When the silver film is attached to the PTFE sheet, all samples have 100% reflectance, as reported in the previous work. Figure

5.5(c,d) shows that the BRDF of all samples are nearly the same at 30° incidence. At 50 ° incidence, there is a small discrepancy in the specular reflectance component, which could come from slight bending of the surface and relatively larger uncertainty.

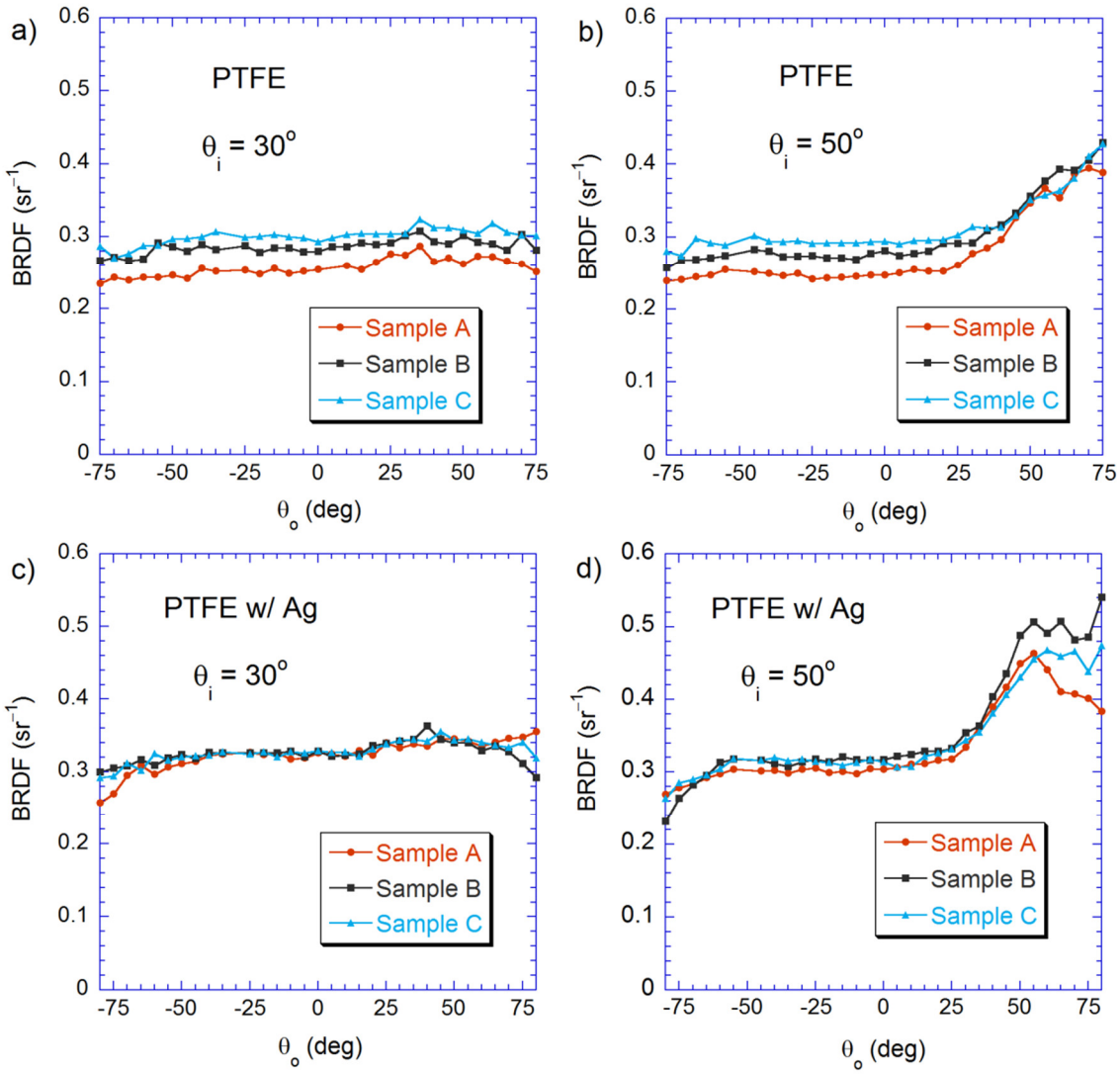

Figure 5.5. The measured BRDF at incidence angles of 30° and 50° for (a, b) Sample A, B and C free-standing PTFE, and (c, d) the three PTFE samples with a Ag film.

Notice that Sample B has the largest specular component, which might come from the slightly smaller density, 1.58 g/cm^3, compared with 1.67 g/cm^3 of Sample A and 1.65 g/cm^3 of Sample C. This could mean a higher porosity and therefore more significant surface scattering at large incident angles. Whether this is the reason or not also needs further investigation. Overall, it can be shown that the variation of sample thickness does not impose significant changes in the measured BRDF. It is also worth mentioning that the PTFE sheets exhibit similar directional radiative features as the dual-layer structure, which has already been proved previously in Figure 5.4.

It is now clear that the dual-layer structure has diffuse radiative properties at normal incidence and a larger specular component at large incident angle, which are not affected by the sample thickness. Nevertheless, whether the surface roughness should affect the BRDF is not known. Another piece was cut from the 0.23 mm-thick PTFE and mechanically polished on one side, named Sample A2. The sample was cleaned, and the surface roughness was measured with an Olympus LEXT OLS4000 3D laser confocal microscope. The surface roughness σ_{rms} values before and after the smoothing process was found to be 3-4 μm and 0.4-1 μm, respectively. The large variation is due to the inhomogeneity in the PTFE surface structure. The BRDF ratio of Sample A2 and Sample A, both with silver film at the back, is plotted in Figure 5.6 for different incidence angles. It is found that small specular peaks exist even at θ_{i} = 30° for Sample A2 relative to Sample A. At large incident angles, the specular component is slightly enhanced with a smoother surface. Since the refractive index of PTFE is 1.3 at the current wavelength [110]. the surface reflectance is not significant. We expect a stronger surface roughness dependence for materials with larger refractive indices.

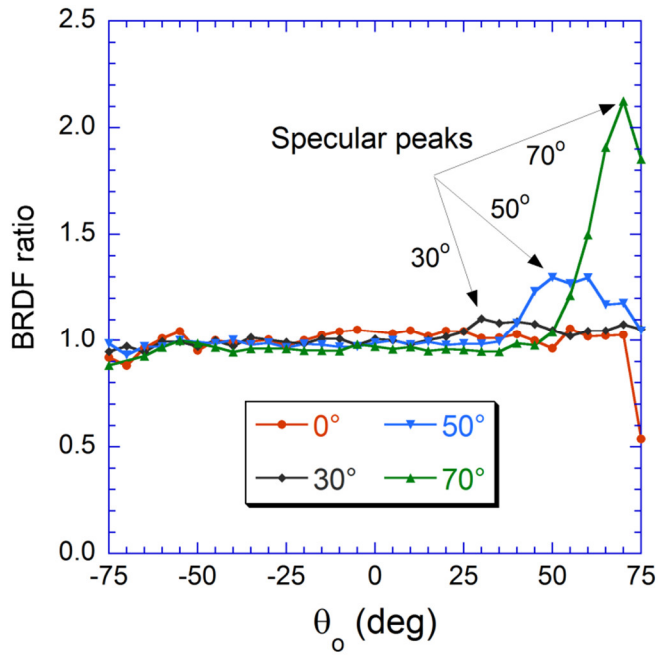

Figure 5.6. Ratio of the measured BRDF of Sample A2 over that of Sample A, both with a Ag film, at different incidence angles.

5.2.3 Theoretical Modeling

To theoretically model the properties of the properties of PTFE, the scattering and absorption coefficient, σ and α are needed due to the volumetric scattering. Unlike monodispersed particle matrix, σ and α of the sintered PTFE sheets cannot be calculated from those of a single particle or a cluster of particles due to its complicated texture. It is imperative to solve them from measured R and T values at each wavelength. In this sense, the theoretical modeling depends on measurement results and is not "purely theoretical". The retrieved σ and α are then taken as input to solve for the R and T of the PTFE sheets using different numerical methods. Once the calculated values are close to the measurement, not only is the σ and α verified, but also can these values be applied to

other samples to predict the properties, including the enhanced reflectance when the Ag film is attached. Note that in addition to the directional hemispherical properties, the bidirectional radiative properties (BRDF and BTDF) can also be calculated from the modeling.

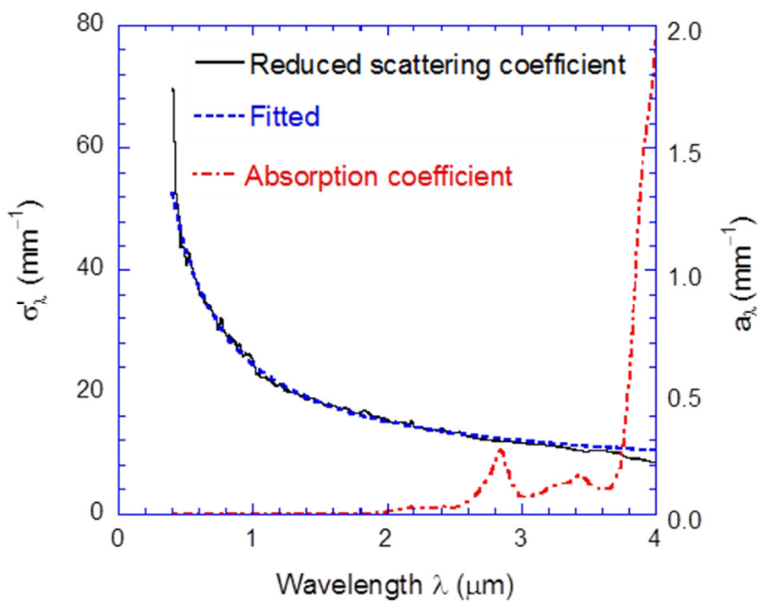

Figure 5.7. Scattering (reduced) and absorption coefficients obtained from the IAD method. The fitted scattering coefficient is also shown.

Based on R_{dh} and T_{dh} of the free-standing PTFE samples, σ and α are retrieved using IAD method and plotted in Figure 5.7. The values are averaged over Sample A, B and C to reduce random error. The reduced scattering coefficient σ' is plotted assuming g = 0.9, since PTFE is anisotropic and with a large forward scattering portion [57]. It is shown that σ' decreases rapidly as the wavelength increases and can be fitted by $\sigma'_\lambda = a + b/\lambda$, where $a = 5.7911\ \mathrm{mm}^{-1}$ and $b = 18.759\ \mu\mathrm{m}\cdot\mathrm{mm}^{-1}$ for $0.4\ \mu\mathrm{m} < \lambda < 3.0\ \mu\mathrm{m}$, and the deviation becomes larger beyond this region as shown in the plot. Note that for Rayleigh

scattering of small particles, the scattering coefficient scales with λ^{-4}. For PTFE, however, the size of the scatters is in the same order as the wavelength and there may exist multiple scattering as well as dependent scattering. The absorption coefficient has peaks around $\lambda = 2.84$ μm and 3.42 μm, and increases rapidly at $\lambda > 3.8$ μm, which are consistent with the absorptance spectra.

With the knowledge of σ and α, the RTE can be solved stochastically using Monte Carlo method. In this work, a Monte Carlo ray tracing (MCRT) algorithm is developed to model the radiative properties of PTFE and PTFE with Ag film. Two versions are implemented, with one only considering the volumetric effect and treat the surface reflection as specular, and the other version considering both surface and volumetric scattering in order to model the bidirectional properties. The detailed implementation and results of the MCRT are presented in the next chapter.

Due to the computational cost for the MCRT, an analytical method is desirable to model the radiative properties of PTFE slab. Since PTFE is a highly scattering medium, the two-flux method appears to be attractive for calculating the d-h properties. The two-flux method was originally proposed by Schuster [48] for modeling light scattering in a foggy atmosphere assuming a forward component and a backward component in a stratified medium for isotropic scattering. It has been expanded and modified in many ways and can even include anisotropic scattering with suitable scaling [23]. Dombrovsky et al. [51] modified the two-flux method to include a collimated beam incidence as well as boundary reflection using an isotropic scaling, which is essentially based on the reduced scattering coefficient for the study of radiative properties of layered structures. In the present study, this modified two-flux approximation is used to obtain the d-h reflectance

of the PTFE, denoted by R_0 and T_0. By considering multiple reflections and taking the d-h reflectance of the Ag film as ρ_{Ag}, one can express the d-h reflectance of the dual-layer structure as follows:

$$R = R_0 + \frac{\rho_{\mathrm{Ag}} {T_0}^2}{1 - \rho_{\mathrm{Ag}} R_0} \tag{5.2}$$

Note that ρ_{Ag} is obtained by integrating the specular reflectance, predicted based on Fresnel's reflection coefficient, over the hemisphere [7]. All the properties in the above equation are wavelength dependent. The results of the modeling are compared with the measurement in the next chapter after the details of MCRT are introduced.

The optical constants (or the dielectric function) of Ag are needed in order to apply either the Monte Carlo method or the modified two-flux method. Note that in the Monte Carlo simulation, the reflectance of Ag is considered based on the incident angle of the scattered photon bundles emerged out of the PTFE sheet. The optical constants compiled by Lynch and Hunter [102] tend to yield a lower reflectance (0.975 ~ 0.985) in the near infrared. The Drude free-electron model gives the dielectric function as

$$\varepsilon(\omega) = \varepsilon_\infty - \frac{\omega_p^2}{\omega^2 + i\gamma\omega} \tag{5.3}$$

where ω is the angular frequency, ε_∞ is the high-frequency constant, ω_p is the plasma frequency, and γ is the scattering rate. Using the following parameters $\varepsilon_\infty = 3.4$, $\omega_p = 1.396 \times 10^{16}$ rad/s and $\gamma = 2.70 \times 10^{13}$ rad/s [31], the Drude model predicts well the infrared reflectance of Ag but fails in the ultraviolet region due to interband transitions [111]. In the present study, the Drude model is used at $\lambda > 1.9$ μm. From ultraviolet to $\lambda =$

1.9 μm, the measured data from Johnson and Christy [112] was used, which has been verified to be suitable particularly for Ag films [113]. Compared with other metals, while Au has a similar reflectance as Ag at $\lambda > 1.0$ μm, its reflectance is much lower at $\lambda < 1.0$ μm [112]. The reflectance of Al is also lower than that of Ag especially at $\lambda < 1.0$ μm due to the interband absorption near $\lambda \approx 0.8$ μm, though Al has a higher reflectance than Ag or Au for 0.2 μm < λ < 0.5 μm due to its higher plasma frequency. Consequently, Ag is the best choice among all metal materials for high solar reflectance.

The optical constants of PTFE are compiled from two references. At wavelengths smaller than 1.5 μm, the refractive index n of PTFE is obtained from Ref. [114], which varies from 1.32 ($\lambda = 0.28$ μm) to 1.29 ($\lambda = 1.555$ μm). The extinction coefficient κ is essentially 0 since PTFE is non-absorbing. At wavelengths from 2 μm to 20 μm, Korte and Röseler [115] measured n and κ of PTFE based on infrared ellipsometry. In the region 1.55 μm < λ < 2.0 μm, linear interpolation is applied to connect the refractive index since the values do not change dramatically, i.e., from 1.29 ($\lambda = 1.555$ μm) to 1.26 ($\lambda = 2.0$ μm).

5.2.4 Solar Reflectance and Application for Radiative Cooling

The solar reflectance is defined as the integral of the spectral reflectance, $R(\lambda)$, over the solar spectrum weighted by the solar spectral irradiance at air mass 1.5, $I_{\mathrm{AM1.5}}(\lambda)$, viz.

$$R_{\mathrm{solar}} = \frac{\int_{\lambda_1}^{\lambda_2} R(\lambda) I_{\mathrm{AM1.5}}(\lambda) d\lambda}{\int_{\lambda_1}^{\lambda_2} I_{\mathrm{AM1.5}}(\lambda) d\lambda} \tag{5.4}$$

where the solar spectral irradiance for AM1.5 can be found from ASTM [69], and the integration limits are $\lambda_1 = 0.280$ μm and $\lambda_2 = 4.0$ μm. The calculated solar reflectance based on the spectral reflectance of Sample A, B, and C is respectively, 0.991, 0.986, and 0.981 with the Ag reflector. Since the solar absorptance can be calculated by $A_{\text{solar}} = 1 - R_{\text{solar}}$, less than 1% of the solar radiation is absorbed by the dual-layer structure made of PTFE (Sample A) plus the Ag film. It should be noted that the solar reflectance for a 10-mm-thick PTFE slab is 0.989, which is between the values obtained for Sample A and B when using the Ag reflector. As mentioned earlier, such a sample is too thick and not suitable for practical applications.

The spectral reflectance for several solar reflective materials is shown in Figure 5.8 for comparison. For white paint pigmented by TiO_2, obtained by Song et al. [116], the reflectance drops quickly in the near infrared and also ultraviolet region. As a result, the solar reflectance is only 0.873. The photonic multilayer structure [75] achieves an average reflectance of 0.979 for $0.4\ \mu\text{m} < \lambda < 2.6\ \mu\text{m}$ and $R_{\text{solar}} = 0.97$ due to the reduction of reflectance at both the longer and shorter wavelengths. The spectral reflectance using Ag film coated on the backside of a transparent polymer embedded with glass microspheres [70] gives a somewhat lower reflectance with $R_{\text{solar}} = 0.96$. The recently published work using porous $P(VdF\text{-}HFP)_{HP}$ coatings reports a solar reflectance of 0.96 [76] (not plotted here). Note that the calculated solar reflectance for Ag films is 0.987 at normal incidence and 0.986 if the reflectance is integrated over the hemisphere. Therefore, the weighted solar reflectance of $R_{\text{solar}} = 0.991$ using a 0.24-mm thick PTFE (Sample A) with the Ag reflector is the highest solar reflectance reported to date among all the natural and

synthesized materials. There may exist a critical thickness beyond which the absorption of silver in the ultraviolet becomes dominant, so that further decreasing the thickness of PTFE would not improve the overall solar reflectance.

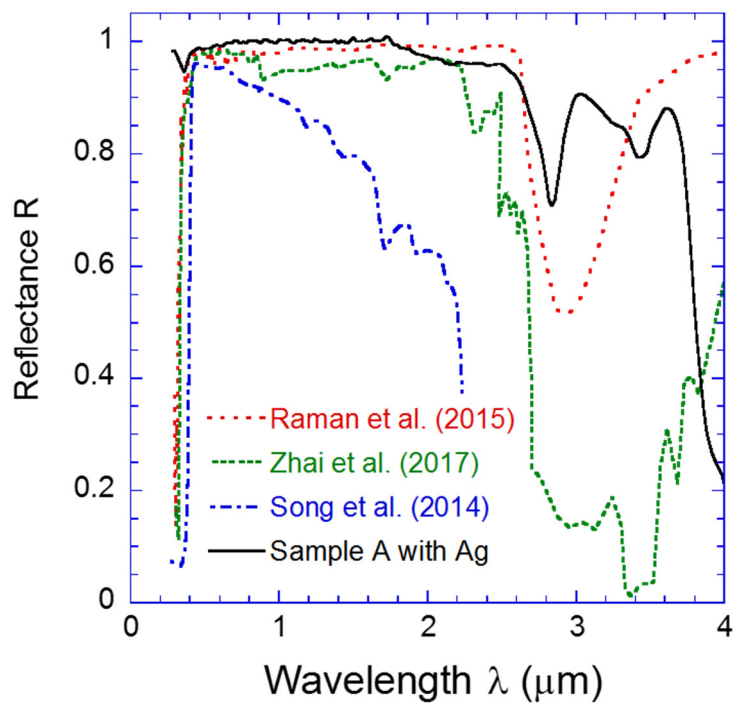

Figure 5.8. Comparison of the measured reflectance of the dual-layer structure based on Sample A with some solar reflectance materials reported in the literature.

Now let us consider the theoretical radiative cooling power of this dual-layer structure. From energy balance, the net cooling energy of an emittance surface is:

$$P_{\text{net}}(T) = P_{\text{emi}}(T) - P_{\text{abs\_sun}} - P_{\text{abs\_amb}}(T_{\text{amb}}) - P_{\text{non-rad}}(T) \qquad (5.5)$$

where $P_{\text{emi}}(T)$ is the power emitted by the surface, $P_{\text{abs\_sun}}$ is the absorption of the solar radiation, $P_{\text{abs\_amb}}(T_{\text{amb}})$ is the absorbed power from the atmosphere radiation,

$P_{\text{non\_rad}}(T)$ is the non-radiative loss from conduction and convection. They can be calculated as follows [78]:

$$P_{\text{emi}}(T) = A\int_{2\pi} d\Omega \cos\theta \int_0^{\infty} \varepsilon(\lambda) I_{BB}(T,\lambda) d\lambda \tag{5.6}$$

$$P_{\text{abs\_sun}} = A\int_0^{\infty} \alpha(\lambda,\theta) I_{\text{AM1.5}} d\lambda \tag{5.7}$$

$$P_{\text{abs\_amb}}(T_{\text{amb}}) = A\int_{2\pi} d\Omega \cos\theta \int_0^{\infty} \varepsilon(\lambda)\varepsilon_{\text{amb}}(\lambda,\theta) I_{BB}(T_{\text{amb}},\lambda) d\lambda \tag{5.8}$$

$$P_{\text{non-rad}}(T) = A h_{\text{eff}}(T_{\text{amb}}, T) \tag{5.9}$$

where A is the exposed surface area, I_{BB} is the blackbody spectral intensity, $\varepsilon(\lambda)$ is the emissivity of the surface, $\alpha(\lambda)$ is the surface absorptance, $\varepsilon_{\text{amb}}(\lambda,\theta) = 1 - t(\lambda)^{1/\cos\theta}$ is the directional emissivity of the atmosphere, and t is the spectral transmittance in the zenith direction, h_{eff} is the effective heat transfer coefficient accounting for the conduction and convection loss. Since the surface being studied in this work is diffuse, the absorptance $\alpha(\lambda)$ and emissivity $\varepsilon(\lambda)$ are not direction-dependent, and they are equal based on Kirchhoff's law. The integration should cover the whole spectrum, however, due to the limitation in instrumentation and data, the atmosphere emittance is available from 0.9 μm to 26 μm, and the measured reflectance is up to 15 μm, beyond which both atmosphere and the surface are treated as blackbody.

As shown in Figure 5.9(a), when non-radiative heat transfer is neglected (e.g., $h_{\text{non-rad}} = 0$), the dual-layer structure with Sample A yields a day-time cooling power of 171.3 W/m^2 when $T_{\text{s}} = T_{\text{amb}}$ = 300 K. The equilibrium temperature can be obtained by setting $P_{\text{net}} = 0$, resulting in $T_{\text{s,eq}}$ = 264 K. These values are very close to the ideal emitter

that reflects all solar radiation and has an emissivity of unity at wavelengths longer than about 4 μm [78]. Note that for daytime cooling when the surface temperature is equal to or above the ambient temperature, high emittance over the entire infrared wavelength beyond the solar spectrum is desired.

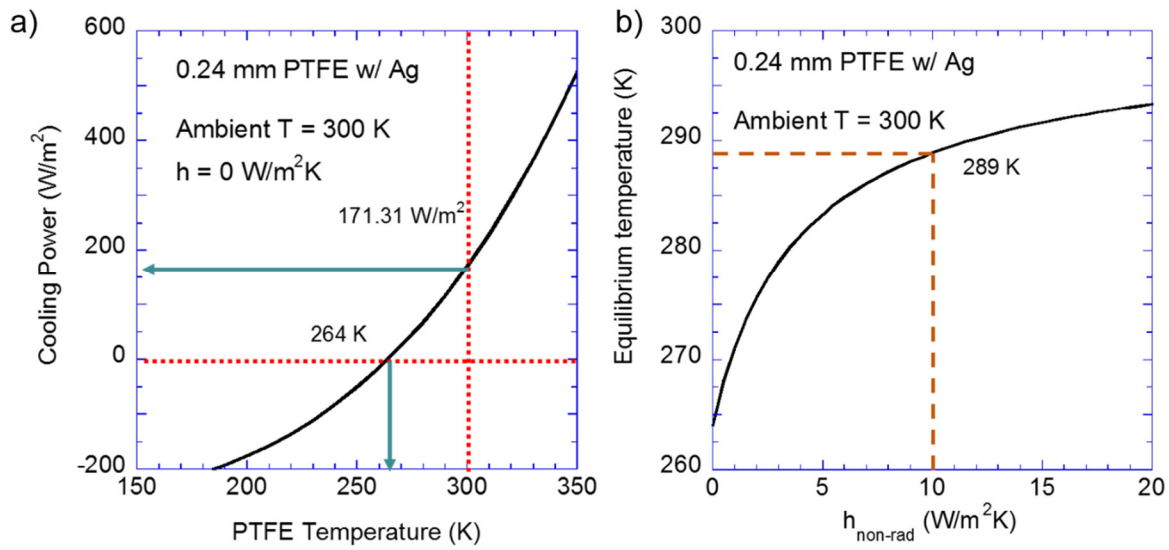

Figure 5.9 (a) Calculated cooling power of sample A at various surface temperatures, non-radiative heat transfer is neglected, and the ambient T is assumed at 300 K; (b) calculated equilibrium temperature of sample A at ambient T of 300 K, and different non-radiative heat transfer coefficients.

When considering heat transfer by conduction and convection, shown in Figure 5.9(b), the equilibrium temperature becomes 11 K lower than the ambient of 300 K with a typical value $h_{\text{non-rad}} = 10\ \text{W/m}^2 \cdot \text{K}$. As the non-radiative heat transfer coefficient increases, the equilibrium temperature increases but remain below the ambient temperature. The impressive radiative cooling capability of this structure comes from the well-designed

solar reflectance and high emittance in the atmospheric window. All three samples have similar emissivity from 8 μm ~ 13 μm, indicating that PTFE film as thin as 0.24 mm is sufficient for this high emissivity. For real-world applications, the Ag coating can be deposited on a thin polymer material, such as a polyester or polyethylene film, which can then be attached to the back side of a PTFE sheet using an epoxy resin that does not absorb solar radiation. It should be noted that the atmospheric transmittance data [117] are for observatories with high elevation and for very clear atmospheric conditions. For typical measurement locations and sky conditions, it could be much lower [118].

CHAPTER 6

NUMERICAL MODELING OF BIDIRECTIONAL RADIATIVE PROPERTIES

This chapter begins with the introduction of Monte Carlo ray tracing algorithm (MCRT) developed for simulating the volumetric scattering, inspired by the research work from Wang et al. [56] and Li et al. [57], which either treats the surface as specular reflection or neglect the mismatch of the refractive indices. Then methods for simulating the surface roughness are discussed, the focus of which will be microfacet slope method as demonstrated by Refs. [108, 119]. In previous numerical studies using MCRT, either surface scattering or volumetric scattering is modeled, both of which are in reasonable agreement with experiments. The purpose of this work is to combine these two effects and apply it to materials with both volumetric inhomogeneity and surface roughness. It will be shown that this method achieves good agreement on the dual-layer structure introduced in Chapter 5, for both directional-hemispherical radiative properties and bidirectional properties, i.e. BRDF and BTDF.

6.1 Monte Carlo Ray Tracing Algorithm

As briefly mentioned in Chapter 2, One of the methods to solve the radiative transfer equation is utilizing the Monte Carlo method. A Monte Carlo method is a stochastic model constructed in which the expected value of a certain random variable (or of a combination of several variables) is equivalent to the value of a physical quantity to be determined. This expected value is then estimated by the average of multiple

independent samples representing the random variables introduced above [120]. For the MCRT described in this work, the random variables being studied and averaged are R_{dh}, T_{dh}, BRDF and BTDF. As many as around 1×10^{7} to 1×10^{8} photons need to be simulated to have converged results. Each of the photons are modeled by certain probability distributions that governs the step size and direction of photon movement. The algorithm of the MRCT is briefly described below.

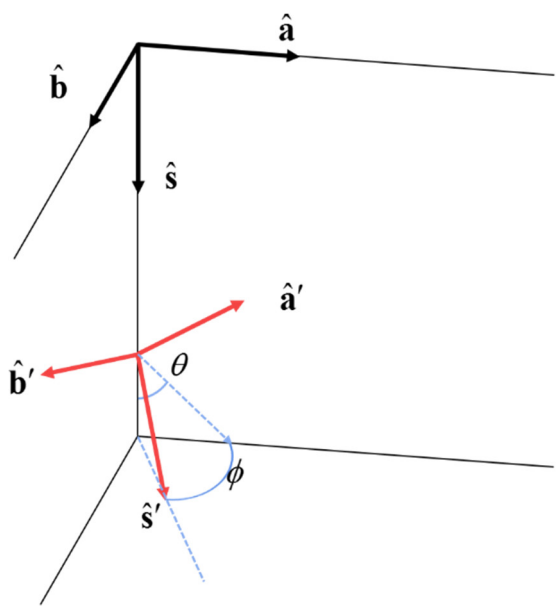

Figure 6.1. The rotation of the local coordinate system after a scattering event; the direction vector of the photon bundle after the scattering ($\hat{\mathbf{s}}$) is described by polar angle θ and the azimuth angle ϕ relative to the previous local coordinate $(\hat{\mathbf{a}},\hat{\mathbf{b}},\hat{\mathbf{s}})$.

A photon bundle is initiated with an energy E and a propagation direction vector ($\hat{\mathbf{s}}$) determined from incident direction ($\hat{\mathbf{s}} = \cos\theta_i\hat{\mathbf{x}} + \sin\theta_i\hat{\mathbf{y}}$). After it is launched, the photon will hit the surface and has a possibility of being reflected. The reflectance R at the

interface is calculated by Fresnel's coefficient considering polarization [7]. When the incident light is randomly polarized, an averaged R of the two polarization is used. Then R is compared with a random number R_1 to decide if the photon should be reflected. If $R_1 > R$, then the photon has a position vector $\hat{\mathbf{r}}$ initialized to be $(0,0,0)$, while $\hat{\mathbf{s}}$ is to be updated based on Snell's law. The propagation step is calculated as:

$$l = -\frac{1}{\sigma + \alpha}\ln(R_2) \tag{6.1}$$

where α and σ are absorption and scattering coefficients obtained from IAD method, described in Chapter 4, R_2 is another random variable between 0 and 1. The photon will experience a scattering event after propagating a length of l, which will update the propagation vector $\hat{\mathbf{s}}$ according to:

$$\begin{aligned}
\hat{\mathbf{s}}' &= \cos\theta\hat{\mathbf{s}} + \sin\theta\cos\phi\hat{\mathbf{a}} + \sin\theta\sin\phi\hat{\mathbf{b}} \\
\hat{\mathbf{a}}' &= -\sin\theta\hat{\mathbf{s}} + \cos\theta\cos\phi\hat{\mathbf{a}} + \cos\theta\sin\phi\hat{\mathbf{b}} \\
\hat{\mathbf{b}}' &= \hat{\mathbf{s}} \times \hat{\mathbf{a}}
\end{aligned} \tag{6.2}$$

where the prime denotes the updated vector, θ and ϕ are polar and azimuth angles relative to the local coordinates defined in the counterclockwise direction illustrated in Figure 6.1, $(\hat{\mathbf{s}}, \hat{\mathbf{a}}, \hat{\mathbf{b}})$ is an orthogonal basis for propagation vector. The scattering in azimuthal direction is assumed to be isotropic, thus $\phi = 2\pi R_3$ where R_3 is another random number. The scattering in the polar angle is determined from Henyey-Greenstein scattering phase function [59], written as:

$$\cos\theta = \begin{cases} \dfrac{1}{2g}\left[1+g^2-\left(\dfrac{1-g^2}{1-g+2gR_4}\right)^2\right], & \text{if } g \neq 0 \\ 2R_4 - 1, & \text{if } g = 0 \end{cases} \tag{6.3}$$

where R_4, as usual, is a uniform random variable from 0 to 1, and g is the anisotropy factor ranging from -1 to 1. The position vector $\hat{\mathbf{r}}$ can be updated once the propagation vector $\hat{\mathbf{s}}$ is updated, as $\hat{\mathbf{r}}' = \hat{\mathbf{r}} + l\hat{\mathbf{s}}'$. The energy of the photon is also updated by multiplying the scattering albedo $E' = \dfrac{\sigma}{\sigma+\alpha}E$, which accounts for the absorption loss in the medium. The process keeps on until the photon exists from either the front or the back of the medium, and the remaining energy is added to obtain either R_{sum} or T_{sum} each time. The estimated R and T value is $\dfrac{R_{\text{sum}}}{N}$ and $\dfrac{T_{\text{sum}}}{N}$, respectively, where N is the number of total photons simulated. Note that it should also be recorded when the photon is reflected from the first incidence at the boundary. The position vector $\hat{\mathbf{r}}$ helps keep track of the photon location to see if it has reached or passed the boundary. If so, it needs to be decided whether the photon is internally reflected based on the incident angle. The reflection at the inner boundary is tricky: in addition to the alteration of propagation vector due to surface roughness (to be discussed in the next section), it is also important to keep track of the remaining propagation length before the next scattering event. When the scattering coefficient is small or the thickness is greatly reduced, the photon transport is dominated by surface scattering and becomes ballistic inside the medium. Failure to notice this effect results in significant error under those conditions.

Overall, this method offers a flexible, yet rigorous approach to handle photon transport in turbid media. As to be discussed in the next section, it also allows easy

implementation of multiple scattering at the surface. However, MCRT does has its disadvantages, the most obvious of which is the computational cost due to its stochastic nature. By utilizing GPUs and parallel computing, the computation time can be reduced. Another important consideration is the applicability of the method. As one might have noticed, each scattering event is treated as independent with no phase information, which means the coherent wave-like interactions and dependent multiple scattering are neglected. Essentially, MCRT is within the geometric optics approximation (GOA) domain, which requires the characteristic length, in this case the mean free path, to be greater than the wavelength of the photons. Finally, the surface randomness is neglected here, thus when considering the BRDF, a specular peak with significantly larger value is always present at the retroreflection direction. This specular peak comes from the first strike at the interface when a certain portion of photons are reflected to an infinitely small solid angle. This issue can be resolved using the surface roughness model to be discussed in the next section.

6.2 Microfacet Slope Method

Modeling the surface roughness can be done in several different ways. The most straight forward way, rigorously solving the Maxwell's equations provides the scattered field from a rough surface. The most popular one is using boundary integral method, based on extinction theorem and Green's theorem, as discussed in Ref. [93, 121]. However, rigorous EM-wave theory is quite challenging due to the unknown nature of surface statistics and the requirement of formidable computational power, which prevents this method to be easily extended to 2D surfaces.

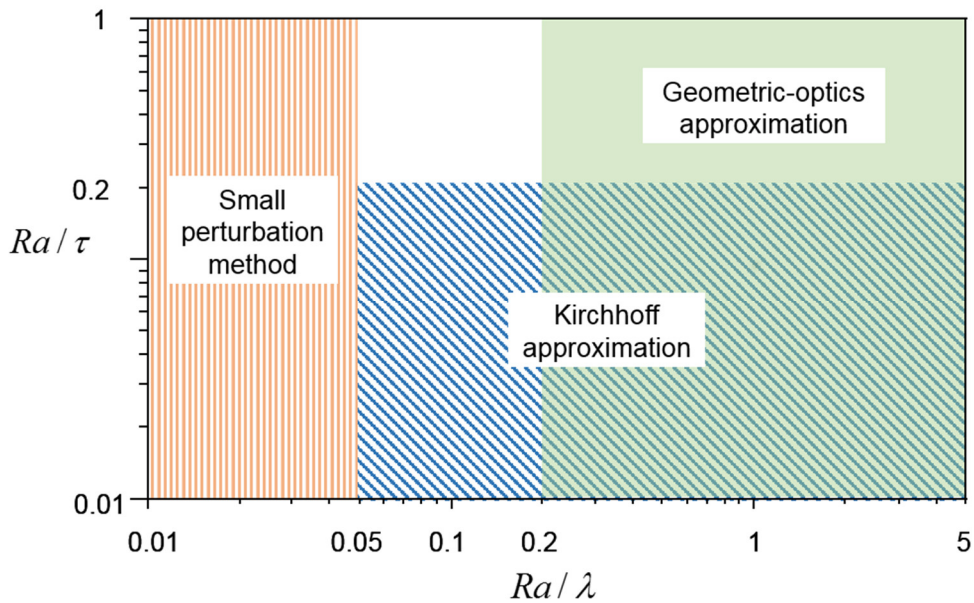

Figure 6.2. Validity domains of approximate methods. In the current study Ra/λ is on the order of 1 and Ra/τ is on the order of 0.1, thus geometric-optics approximation is used.

Approximation methods, on the other hand, not only have the advantage of being flexible and easy to be implemented, but also provide physical insight by simplifying the problem. Two fundamental approximations are: the high-frequency method known as the Kirchhoff approach (KA) and low-frequency method known as the small perturbation method (SPM) [122, 123]. While SPM is applicable for surfaces with a small rms roughness with respect to the incident wavelength, KA, also known as tangent-plane approximation, is valid for large radii of curvature or locally smooth surface, meaning that the rms roughness can be larger but the steepness should be small. KA reduces to the geometric optics approximation (GOA) in short wavelength regime. The major disadvantage of these approximation methods is the difficulty in precisely determining the

validity domains, which dependents on the surface statistics and whether it is dielectric or perfectly conducting. Figure 6.2 is provided as a rough guideline to select the appropriate approximation method in dealing with surface scattering problems. The boundary values are not precisely defined, and the details can be found in Ref. [93].

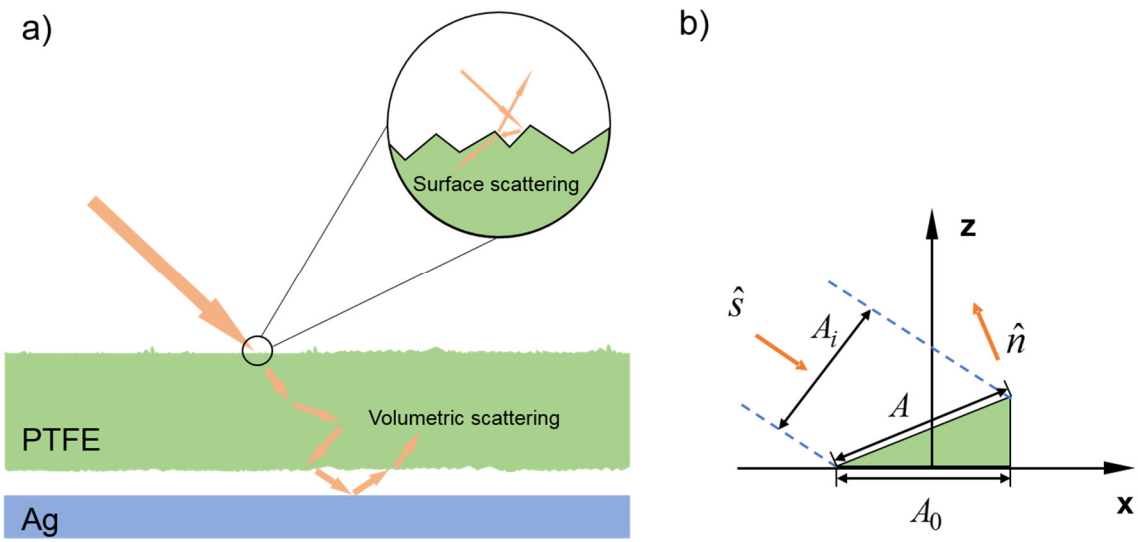

Figure 6.3. (a) Schematic of the Monte Carlo model incorporating both surface and volumetric scattering, the surface roughness is simulated using the microfacets as shown in the inset; (b) illustration of the weighted probability density function considering the effect of projected area, each microfacet is assumed to have the same projected area to the x-y plane A_0, $\hat{\mathbf{n}}$ is the surface normal and $\hat{\mathbf{s}}$ is the unit directional vector of the ray.

In the present work, GOA is adopted to incorporate surface roughness into the framework of MCRT. This method models the rough surface as an aggregate of small and mirror-like microfacets, upon which the incident light is specularly reflected from Fresnel's equations or refracted according to Snell's law, as shown in Figure 6.3(a). Although

multiple scattering and shadowing effects can be easily handled in this method, it doesn't allow the consideration of interference effects. In addition, for GOA to be valid, generally both the autocorrelation length (τ) and the root-mean-square (rms) roughness (*Ra*) should be greater than the wavelength (λ) [124, 125]. These requirements are also met by applying the MCRT, which makes the GOA an ideal candidate to model surface scattering along with the volumetric scattering. Previously, this method has been successfully applied to semitransparent materials with rough surfaces and coatings [108, 119] , which does not experience volume scattering, such as silicon/SiO_2 wafer, but not on porous sintered polymers with rough surfaces such as the PTFE sheet in this present work. To generate the microfacets in the Monte Carlo program, the surface generation method (SGM) and microfacet slope method (MSM) has been proposed. SGM requires the numerical realization of a surface, usually be much larger than the film thickness, which is not feasible for this work. The other method MSM is selected instead.

The MSM models the rough surface by generating the microfacet orientations instead of an actual surface profile, therefore both the orientation and whether the ray restrikes the surface are determined based on probability functions. The orientation is determined from a weighted probability density function (WPDF) [108],

$$p_w(\zeta_x, \zeta_y) = \frac{\eta \exp[-(\zeta_x^2 + \zeta_y^2)/2w^2]}{\iint \eta \exp[-(\zeta_x^2 + \zeta_y^2)/2w^2] d\zeta_x d\zeta_y} \tag{6.4}$$

where $\eta = A_i / A_0 = -\hat{\mathbf{n}} \cdot \hat{\mathbf{s}} / \hat{\mathbf{n}} \cdot \hat{\mathbf{z}}$ when $\hat{\mathbf{n}} \cdot \hat{\mathbf{s}} < 0$ and $\eta = 0$ when $\hat{\mathbf{n}} \cdot \hat{\mathbf{s}} \geq 0$ (shown in Figure 6.3(b)), ζ_x and ζ_y are the tangent of the inclination angle of the microfacet, w is the rms slope, equals to $\sqrt{2}Ra/\tau$ for Gaussian surfaces. Note that τ is independent of incident

direction since the surface roughness is isotropic. The rejection method is used when implementing the program to avoid the evaluation of an indefinite integral in the WPDF. Unlike previous methods which deviates from the reciprocity principle [119, 126], this WPDF considers the influence of the projected area of the microfacet, thus it is able to satisfy the reciprocity principle and agrees well with available analytical solutions [108].

Considering the effect of multiple scattering, the surface roughness not only alters the propagation direction at first strike on the surface, it also blocks some reflected photon bundles from leaving the surface by re-striking. This effect is modeled using the following shadowing function proposed by Smith [127]:

$$p_{\mathrm{re}}(\mu) = \frac{\exp(-\mu^2)}{\exp(-\mu^2) - \mu\sqrt{\pi}\,\mathrm{erfc}(\mu) + 2\mu\sqrt{\pi}} \tag{6.5}$$

where $\mu = \tan(90^\circ - \theta_{\mathrm{re}}) / \sqrt{2}w$, θ_{re} is the zenith angle of the incidence or reflectance ray and "erfc" is the complementary error function, p_{re} is the re-striking probability. If a random number is great than p_{re} , the ray will escape and contribute to either transmittance or reflectance. Otherwise it will reach the surface again and undergo stochastic events such as reflection or refraction. Note that each time when the photon bundle is incident on the interface, it should experience the same process to check if the re-striking happens on either inner or outer side of the film. To monitor the BRDF and BTDF, virtual detectors with a solid angle of 2.15×10^{-3} sr is placed in 3-deg intervals in the plane of incidence to collect the escaped bundles and report the average value afterwards. In this manner, the surface scattering can be successfully integrated into the MCRT with volumetric scattering. Note that 50 million (5×10^7) photon bundles are used, which takes approximately 3.5 hours on

a computer with four 3.2 GHz i-5 processors for a sample thickness of 500 μm. The number of photon bundles can be reduced if only R_{dh} and T_{dh} are needed. The average statistical fluctuation of BRDF is within 1%.

6.3 Modeling Results and Comparision

Modeling the d-h radiative properties of PTFE and PTFE w/ Ag structure has been covered in Chapter 5 using the two-flux model and inverse adding-doubling method. To facilitate the MCRT developed in this work, the averaged scattering and absorption coefficients retrieved using IAD are needed, plus the optical constants of PTFE and silver film [52]. Surface roughness Ra and autocorrelation length τ are also needed for the surface scattering, both of which are obtained from an Olympus LEXT OLS4000 3D laser confocal microscope. The value of w determined from the measurement is 0.1 ~ 0.2, thus two sets of simulations were run using $w = 0.1$ and $w = 0.2$ separately.

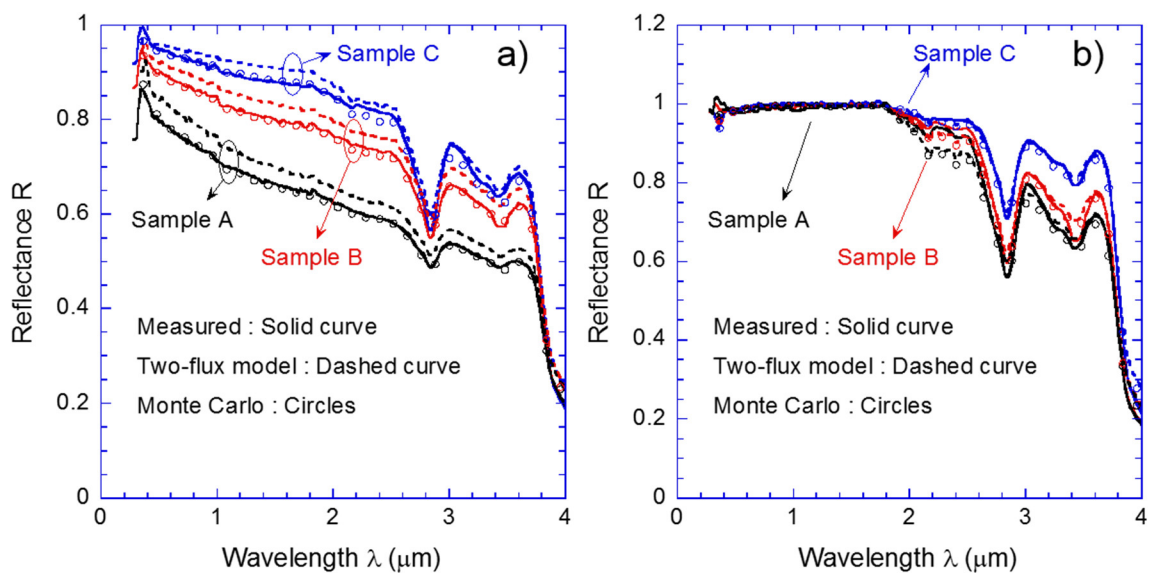

Figure 6.4. Comparison of the predicted reflectance made by MCRT and the two-flux model with measured values of (a) PTFE sheets and (b) PTFE with Ag.

Figure 6.4(a) shows the modeled d-h radiative properties compared with measurement for free-standing PTFE sheets. The MCRT simulation is carried out for 30 wavelength values from 0.36 μm to 4.0 μm using $g = 0.9$ with the averaged scattering and absorption coefficients. The MCRT prediction matches with the measurement very well for all three samples, except Sample C for $2.1\ \mu\text{m} < \lambda < 2.4\ \mu\text{m}$ and for $3.0\ \mu\text{m} < \lambda < 3.5\ \mu\text{m}$ where the difference is relatively large, which might come from sample variations. The Monte Carlo model was also compared and validated by using the adding-doubling method and should be considered reliable. On the other hand, the modified two-flux model assumes isotropic scattering with the scaled (reduced) scattering coefficient, and it tends to overpredict the reflectance by 0.02 ~ 0.03 for all samples throughout the spectral range. The reason is not clear, but it might have demonstrated the limitation of the two-flux model.

The predicted and measured reflectance spectra for the dual-layer structure are shown in Figure 6.4(b), for Samples A, B, and C, respectively. The MCRT prediction agrees with the experiment well throughout the spectral range for Sample A and up to $\lambda =$ 2 μm for Samples B and C. From 2.2 μm to 2.5 μm, the measured reflectance for Sample B and C is higher than that predicted. The underestimation of all three samples might have come from the overestimation of absorption coefficient. As explained previously, when the absorption is relatively small, due to the uncertainty in the measurements, the retrieved absorption coefficient by the IAD may be subject to a relatively large uncertainty, even though the agreement with the measurements for the free-standing PTFE is very good. The

thicker the sample, the larger the mismatch becomes due to the enhanced absorption by multiple scattering. Beyond 2.5 μm, the MCRT agrees with experiment fairly well. The two-flux model yields quite good agreement with the experiment for the dual-layer structure, except for $2.1\ \mu\text{m} < \lambda < 2.5\ \mu\text{m}$ as well as near the reflectance peaks and valleys beyond 2.5 μm. This suggests that, despite the isotropic scattering coefficient used in the two-flux model, the analytical formulation can be used for the design of dual-layer structures. Note that the results for MCRT does not incorporate the surface scattering yet, since the wavelength extends to 4 μm, which might render the GOA and MSM invalid.

For the bidirectional radiative properties, BTDF is not plotted since no transmission peaks are observed. Figure 6.5 shows the calculated BRDF compared with the measurement. When $w = 0.1$, the surface is flatter and a visible specular peak is predicted even at small incidence angles. The specular component also appears to be much larger than the experimentally observation. Overall, the calculation with $w = 0.2$ agrees better with the measurement. The model agreement could be improved with the iteration of *w*; however, due to the relatively large measurement uncertainties at large observation angles as well as the limitation of the surface microfacet model, it is difficult to obtain good fitting in all spectrums by simply tuning one parameter. At $\theta_\text{i} = 0°$ and 30°, the calculation using $w = 0.2$ shows no specular reflection, which agrees well with the measurement. At 50°, however, the calculation predicts a shifted and stronger specular reflection compared with the measurement, which has a plateau for $50° < \theta_\text{o} < 75°$. The results are similar at 70° incidence. While there may be inherent limitations, the Monte Carlo model used in the present study is capable of predicting the trend of the bidirectional radiative properties of

the inhomogeneous material with both volume scattering and surface scattering characteristics.

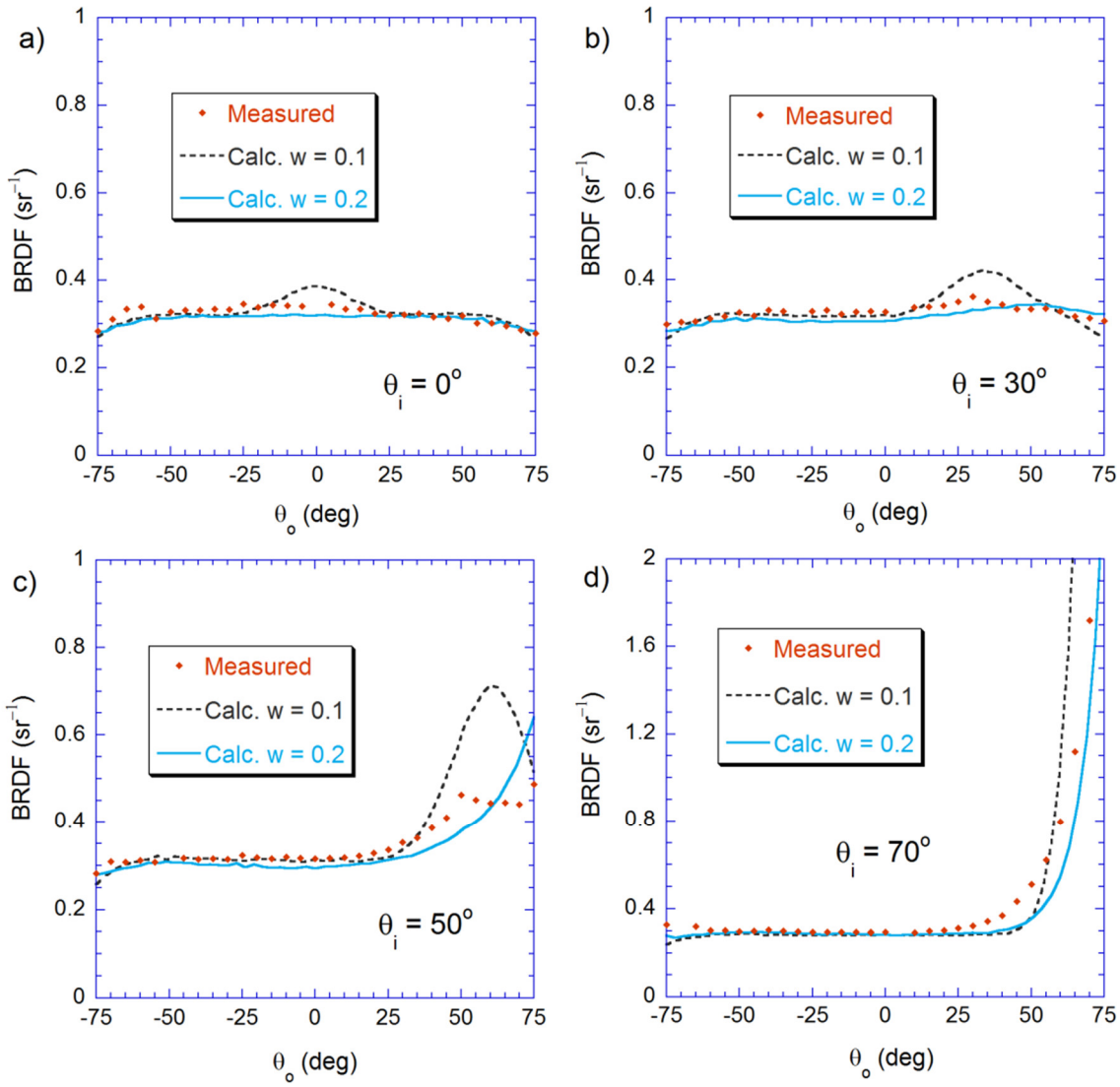

Figure 6.5: Comparison of measured BRDF with those simulated using two rms slopes w = 0.1 and 0.2 at incidence angles of (a) 0°, (b) 30°, (c) 50° and (d) 70°, respectively.

To estimate the critical thickness at which the specular reflection becomes significant, we have calculated the bidirectional radiative properties using the Monte Carlo

method by reducing the PTFE thickness. Figure 6.6 plots the calculated BTDF for free-standing PTFE sheets and BRDF of the dual-layer structure for PTFE thickness d = 200 μm, 100 μm, 50 μm, and 10 μm, respectively, at normal incidence. The scattering coefficient is set to σ = 34.4 mm^{-1} as before and the surface slope of w = 0.2 is used. The BRDF of free-standing PTFE is not shown since it remains diffuse even with d = 10 μm. Note that the specular component in the BTDF becomes visible at d = 100 μm, and significant at d = 50 μm. The BTDF values of d = 10 μm at near normal observation angle are too large to be shown in the plot with a maximum BTDF = 10.

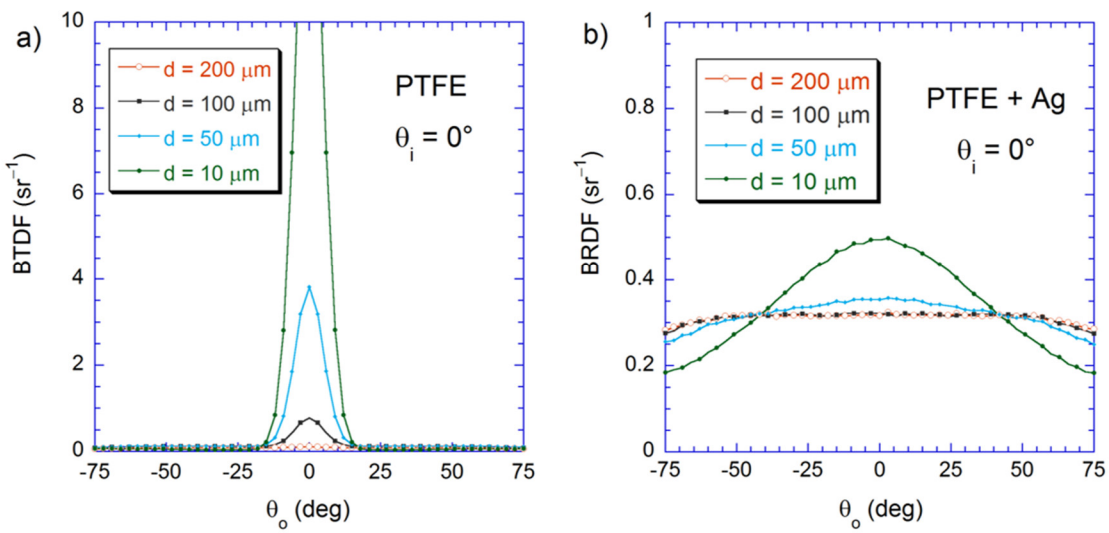

Figure 6.6: Simulated (a) BTDF of free-standing PTFE and (b) BRDF of PTFE sheet with a Ag film at normal incidence. The PTFE thickness d is treated as a variable.

It should be noted that at the specular peak, the BTDF and BRDF is very sensitive to the size of the detector or virtual detector. As a result of the significant specular transmittance, the BRDF of the dual-layer structure has a strong and broad specular lobe when the

thickness is 10 μm. At d = 50 μm, the specular component is rather weak. This suggests that the optimal thickness of the dual-layer structure should be between 50 μm and 100 μm to remain diffuse at the wavelength of 635 nm, and it should also be applicable to other wavelengths in solar spectrum. Advanced techniques may allow the fabrication of thinner PTFE sheet directly on the surface of the Ag film. Care must to be taken such that no significant absorption exists inside any adhesive layer, which may reduce the solar reflectance for daytime cooling application.

At oblique incidence, a shifted specular lobe is produced in the dual-layer structure as shown in Figure 6.7 at an incidence angle of 30°. The results are calculated by scaling the sample thickness with a factor of 0.2, setting d = 200 μm, 40 μm, and 8 μm, while keeping the surface slope parameter at w = 0.2. It can be seen from Figure 6.7(a) that BRDF of free-standing PTFE sheets decreases when the thickness decreases, but remains relatively diffuse and no specular component is observed. For the dual-layer structure shown in Figure 6.7(b), a significant specular lobe emerges at d = 40 μm and becomes dominant at d = 8 μm. This, again, demonstrates the specular reflection added by attaching the Ag film to the back of the PTFE sheet. Note that when the surface is perfectly smooth, the BRDF should approach Dirac delta function as d reduces and scattering becomes negligible. The remaining diffuse component observed in Figure 6.7(b) mainly comes from the surface roughness. Note that the thickness 8 μm is much smaller than the mean free path or penetration depth $l = 1/\sigma \approx 30$ μm. In such a case, the effect of volumetric scattering is negligible, but surface roughness can contribute to the shift of the specular lobe.

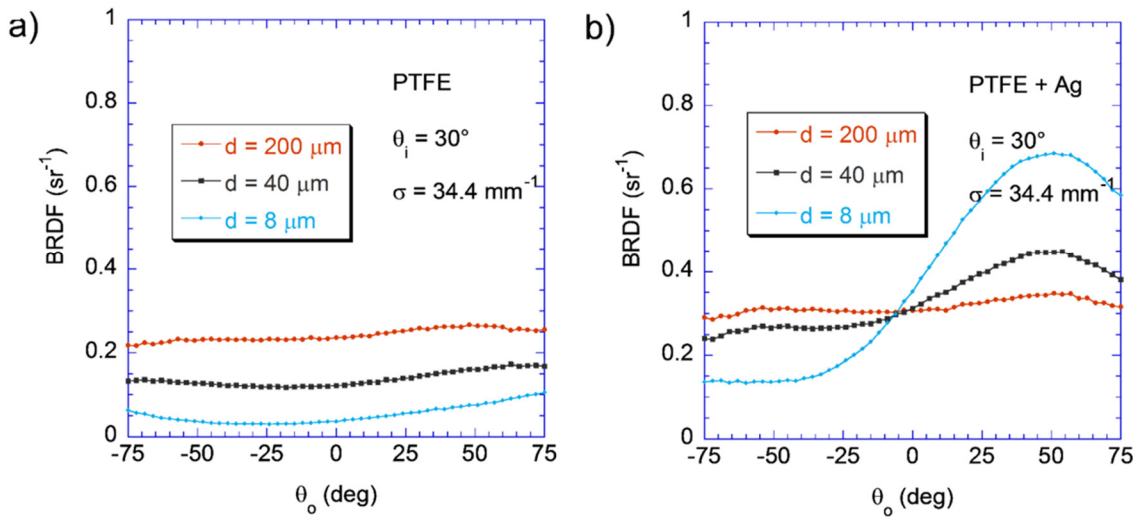

Figure 6.7: Simulated BRDF for different thicknesses at 30° incidence angle for (a) free-standing PTFE and (b) PTFE with a Ag film.

It should be noted that reducing the sample thickness d or scattering coefficient σ essentially yields the same results; this has been verified numerically. This similarity can be explained by the effect of optical depth given by $(\sigma+\alpha)d \approx \sigma d$, indicating that the product of σ and d controls the magnitude of volumetric scattering. This fact may be useful in designing paints/coatings for radiative cooling applications in order to obtain nearly diffuse surfaces with high reflectance.

CHAPTER 7

DEMONSTRATION OF MAGNETIC POLARITONS IN DEEP METAL GRATINGS

This chapter focuses on EM waves in periodic structures by experimentally demonstrates the excitation of magnetic polaritons (MPs) in deep metal gratings. The fabrication method of the samples is introduced first, along with the measurement and calibration methods. Then, the theoretical calculation using rigorous coupled wave analysis (RCWA) is introduced. Simple grating theory is used to analyze the trend of the resonance frequency of the mode. Finally, experimental results are compared with theoretical calculation, with discussions on the influence of incidence angle, plane of incidence, polarization, and the grating's geometric dimensions. This work, for the first time, measured MP in deep metal gratings, experimentally and theoretically studied the MP dispersion for off-plane layout.

7.1 Sample Fabrication and Measurement

The process flow of the fabrication of samples are shown in Figure 7.1. A 500-μm-thick silicon wafer was diced into chips of 20 mm by 20 mm for the fabrication of deep Al gratings. In the mid-infrared region, Al can excite plasmons with low loss similar to noble metals such as Au and Ag. Furthermore, it is inexpensive and can be etched vertically with the plasma etching technique. After ultrasonic cleaning, a 3-μm-thick Al film was deposited onto the chips by e-beam evaporation. The metal surface was polished to reduce the rms roughness caused by grain boundaries to below 30 nm, which was verified by subsequent measurements using atomic force microscopy (AFM) and scanning electron

microscopy (SEM). The fabrication of grating structures was achieved using state-of-the-art nanofabrication techniques. After a photoresist of thickness 800 nm to 1000 nm was spin-coated, electron-beam lithography was used to pattern the grating structure with an area of 5 mm by 5 mm near the center of the sample. Dry etching of Al thin film was then carried out with a Panasonic Dry Etcher APX300, which is capable of nearly 90° anisotropic etching of Al film, allowing the fabrication of deep Al grating with small trench width.

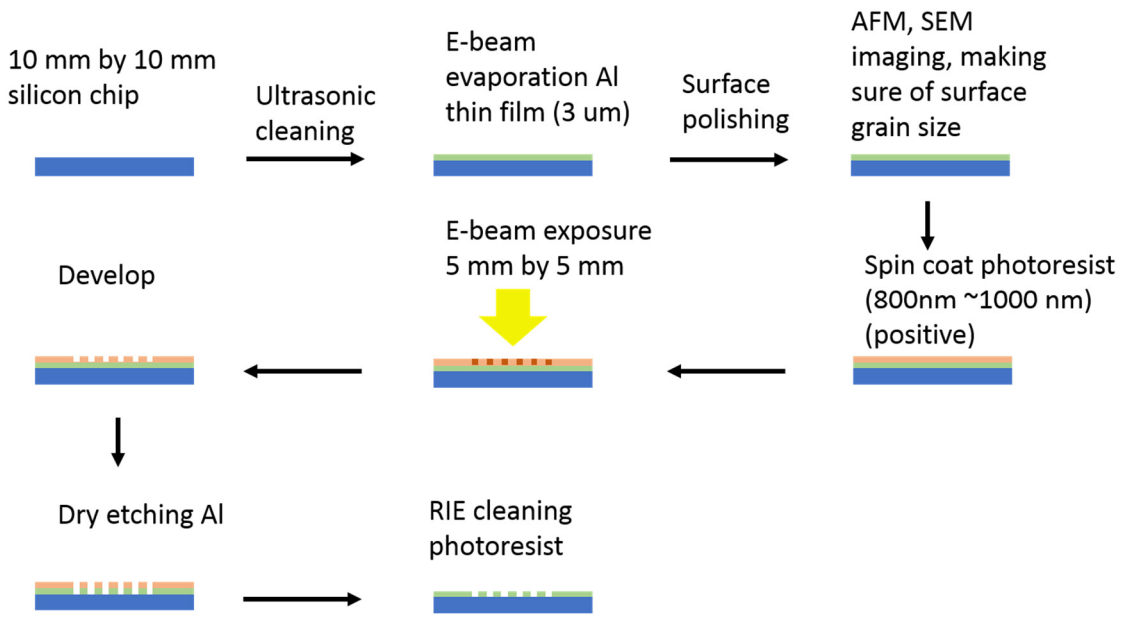

Figure 7.1. Process flow of the grating fabrication using photolithography.

Note that the trench depths range from 1.3 μm to 2 μm, such that the Al film is still opaque and no silicon surface is exposed. After anisotropic etching, the remaining photoresist was removed using reactive-ion etching (RIE). The last step in the fabrication is to remove the oxide layer on top surface by hydrochloric acid. The fabricated Al grating was then examined by SEM from the top to characterize the grating period and trench width. Three

samples were fabricated with slightly different trench depths and widths and were named as AL01, AL02 and AL03. The typical grating period is 4 μm, and the trench width is 350 nm. The details of the physical dimensions will be presented later.

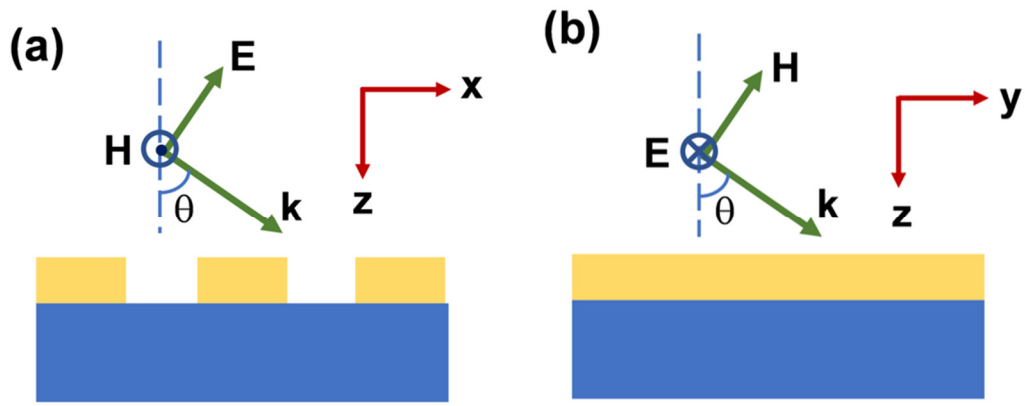

Figure 7.2. Schematic of the polarization and orientation in the FTIR measurement for (a) in-plane layout, where the plane of incidence of a TM wave is perpendicular to the grooves and (b) off-plane layout, where the plane of incidence of a TE wave is perpendicular to the grating vector which is in the x-direction.

To measure the spectral radiative properties of fabricated metal gratings, the FTIR with different specular reflectance accessories was used for incidence angles at 10°, 30° and 45°. A wire-grid IR polarizer was used to fix the incident wave to transverse electric (TM) or transverse magnetic (TE). Two configurations were used in this study. The in-plane layout illustrated in Figure 7.2(a) is the conventional configuration for diffraction diffractive gratings. The coordinate is based on the gratings such that the grating vector is in the x-direction, the grooves are parallel to the y-axis, and the surface normal is parallel to the z-axis. When the grating vector lies in the plane of incidence, all diffracted waves fall in the plane of incidence as well. SPPs or MPs can be excited only if there exists a

nonzero magnetic field component in the direction parallel to the grooves. Hence, only TM waves can excite SPPs and MPs for in-plane layout.

The off-plane layout as illustrated in Figure 7.2(b) is a special case of the conical diffraction configuration, when the incident and diffracted waves are not orthogonal to the grating grooves [128]. Here, by rotating the sample with respect to the z-axis by 90°, the plane of incidence is parallel to the grooves (i.e., in the y-z plane). It should be noted that for off-plane layout, the diffracted waves (except for the zeroth order) are not confined to the plane of incidence. The diffracted beams actually form a semi-cone. In this case, TE wave incidence is needed to excite SPPs and MPs. Because the fabricated grating area is small, 5 mm × 5 mm square, a sample holder with an aperture of 3 mm diameter was used to limit the beam spot size on the sample. Special care must be taken in placing the sample since a slight misplacement could cause a rise in the overall measured reflectance due to the contribution from the smooth Al surface component. Additionally, the orientation of the sample is also important since a slight rotation would give rise to the contribution from unwanted polarization. Note that the sample holder was coated black to avoid reflection outside the aperture, and an open beam signal was measured for each polarization/incidence angle and subtracted from the measured spectrum to eliminate the effect of residual reflection by the sample holder. The measured spectrum was averaged over 256 scans, from about 500 cm^{-1} to 6000 cm^{-1} with a resolution of 4 cm^{-1}, and the overall uncertainty was estimated to be 0.02, considering the various possible sources of error, including misalignment of sample and polarizer, mirror reflectance and beam divergence

7.2 Theoretical Calculation

The structure is modeled as a binary Al grating on top of a semi-infinite Al substrate, given that the remaining Al layer after etching is thick enough to block all infrared radiation. Theoretical analysis of deep metal gratings was performed using RCWA, which numerically solves Maxwell's equation in layered and periodic medium [83, 129]. By Fourier expansion of the space harmonics of the solution, the second-order partial differential equation could be transformed to a system of ordinary differential equations, which could be written in the form of a matrix formulism and solved as an eigenvalue problem [128]. The accuracy of the solution depends solely on the number of terms in the field space-harmonic expansion. In the present study, a total of 301 diffraction orders were used to ensure convergence for both in-plane and off-plane layouts [83]. The ratio of the total energy by all the diffraction orders propagating towards the upper hemisphere to the incident energy gives the directional-hemispherical reflectance (R). Since subwavelength gratings were used in this study, only one or a few diffraction orders are propagating waves. It should be noted that the FTIR measurement is for specular component only due to the use of the specular reflectance accessory. Hence, only the zeroth diffraction order is captured during the experiments as to be discussed later.

Although RCWA manifests itself as a well-established numerical method for solving electromagnetic waves diffraction by periodic structures, a faster and more intuitive method is desired to facilitate the design of metal gratings with tailored radiative properties. An equivalent circuit model, known as LC model, has been used to successfully predict fundamental MP resonance frequency in deep gratings [90, 130]. The LC model takes a unit cell of the structure, (e.g., gratings) and treats the trench as a dielectric capacitor. The metallic materials around the trench are treated as a conductor by neglecting the

resistance component. The inductance has two components: kinetic inductance L_k from the phase delay of induced current with respect to the external electrical field and mutual inductance L_m from the interaction of the parallel walls in the trench. The mutual inductance is given as:

$$L_m = \mu_0 \frac{hb}{l} \tag{7.1}$$

where μ_0 is the vacuum permeability, l is the length in y-direction and is set to unity for 1D gratings, and h and b are the trench depth and width, respectively. The kinetic inductance can be calculated from:

$$L_k = -\frac{2h+b}{\varepsilon_0 \omega^2 l \delta} \frac{\varepsilon'}{(\varepsilon'^2 + \varepsilon''^2)} \ . \tag{7.2}$$

Here, ε' and ε'' are the real and imaginary parts of the dielectric function (ε) of the metal, δ is the penetration depth of electric field, given as $\lambda / 2\pi\kappa$ with κ being the extinction coefficient at the corresponding wavelength. The capacitance of air in the trench can be approximated as:

$$C = c' \varepsilon_0 \frac{hl}{b} \ , \tag{7.3}$$

where ε_0 is the vacuum permittivity and c' is a numerical factor between 0 and 1 accounting for the non-uniform charge distribution along the height of the gratings. It has been suggested that c' be taken as an adjustable parameter of about 0.5 [90]. In the present study, it is taken as 0.6 by comparison with the RCWA results. The total impedance of the equivalent LC circuit can then be written as:

$$Z_{\text{tot}} = i\omega (L_k + L_m - \frac{1}{\omega^2 C}) \ . \tag{7.4}$$

Note that the resistance term is dropped since it has little impact on the resonance frequency [131]. By setting the total impedance to zero, the resonance peak in terms of wavenumber $\nu = \omega / (2\pi c_0)$ can be expressed as:

$$\nu_{\mathrm{MP1}} = \frac{1}{2\pi c_0 \sqrt{(L_k + L_m)C}} \ . \tag{7.5}$$

The above equation must be solved iteratively because the kinetic inductance L_k is frequency dependent. This allows the determination of the resonance location of the fundamental mode of MPs, i.e., MP1 (where the number indicates the harmonic sequence order). The validity of using LC model to predict MP resonance in deep metallic gratings has been extensively discussed in Ref. [90].

The SPP excitation condition is that the magnitude of the parallel wavevector equals [7, 132, 133]:

$$k_{\mathrm{SPP}} = k_0 \sqrt{\frac{\varepsilon_1 \varepsilon_2}{\varepsilon_1 + \varepsilon_2}} \tag{7.6}$$

In the above equation, $k_0 = \omega / c_0$ is the wavevector in vacuum, $\varepsilon_1 = 1$ is the dielectric function of the air, and ε_2 is the dielectric function of the second medium (aluminum). Only the real part of ε_2 is used in Eq. (7.6) and it is a negative value for metal in the visible and infrared regions. When the absolute value of $\mathrm{Re}(\varepsilon_2)$ is very large, it can be seen that $k_{\mathrm{SPP}} \approx k_0$. For the in-plane layout, k_y is always equal to zero, and parallel wavevector of the *m*th order diffracted wave is [7]:

$$k_{x,m} = k_0 \sin\theta + \frac{2\pi m}{\Lambda} \tag{7.7}$$

where Λ is the period of the grating and note that $k_x = k_0 \sin\theta$ is the parallel wavevector component of the incident wave. By setting $m = -1,\ 1,\ -2,\ 2,\ \ldots$ so that $k_{x,m} = \pm k_{\mathrm{SPP}}$, SPPs can be excited by the *m*th diffraction order.

For off-plane layout when the incidence is in the *y*-*z* plane, $k_y = k_0 \sin\theta$ for the incident and all diffracted waves [128]. Furthermore, for *m*th order diffracted wave, we have:

$$k_{x,m} = \frac{2\pi m}{\Lambda} \tag{7.8}$$

Therefore, the SPPs for positive and negative diffraction orders with the same $|m|$ coincide with each other. The condition for SPP to be excited by the *m*th diffraction order is [132, 133]:

$$\left(\frac{2\pi m}{\Lambda}\right)^2 + k_0^2 \sin^2\theta = k_{\mathrm{SPP}}^2 \tag{7.9}$$

The above equations will be used in the next section to interpret the results, especially for off-plane layout.

7.3 Results and Analysis

The dimensions of the fabricated gratings were examined with SEM before optical measurements. Figure 7.3(a) shows an SEM image of grating AL02 and the dimensions measured from the image are indicated on the figure. Measurements of several periods were taken and averaged to reduce the random uncertainty of reading. As indicated on the figure, the results are very consistent. Figure 7.3(b) is a close-up view showing measurements of a grating trench. It should be noted that the relative variation is much larger for the measured grating trench width than for the period because the boundary

between the trench and the metal surface is not well demarcated in the SEM image. The grating depth is the remaining geometric parameter, which could not be measured directly from SEM image without breaking the sample.

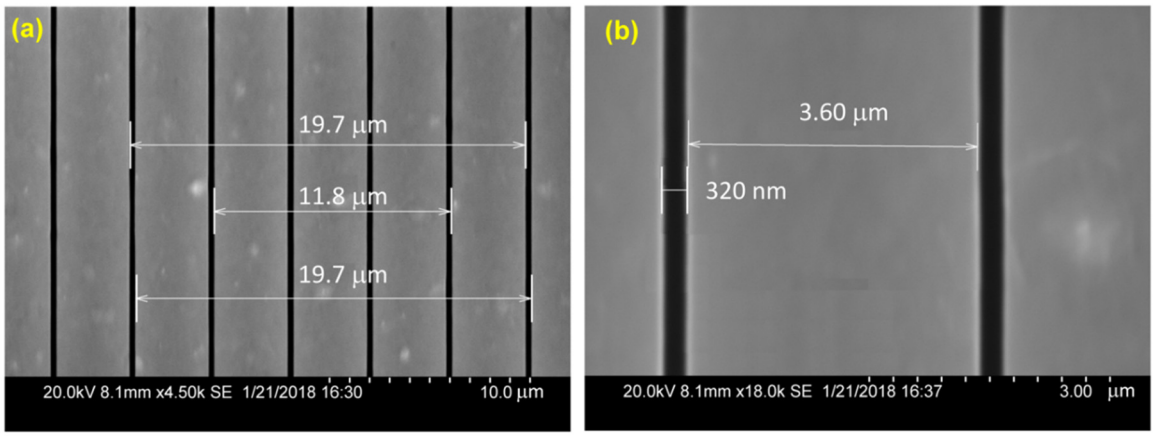

Figure 7.3. Scanning electron microscopy images of sample AL02 with indication of measurements of (a) the periods and (b) trench/ridge widths. Measurements of the period are intentionally repeated to indicate statistical variations.

Using the SEM measurement as a reference, the three geometric parameters of each sample were obtained by fitting the calculation of RCWA to the measured reflectance, at all three incidence angles from in-plane layout, from 540 cm^{-1} to 4000 cm^{-1}. A brute-force search was applied using a step size of 20 nm, followed by a finer grid of 5 nm around the minimum. At each step, the standard error of estimate (SEE) or the root-mean-square error was calculated for the specific structure and the smallest of all SEE obtained gives the best fit of each sample. The fitted sample parameters are listed in Table 7.1 along with the corresponding SEE, which is between 3% and 4%. The uncertainties of the fitting were obtained by examining the relative error compared with the smallest SEE, which is 30 nm

for both the height and trench width, and 50 nm for the grating period. After the spectroscopic measurements, two samples were cut with focus ion beam (FIB) to obtain cross-section images using SEM. The results show excellent vertical slope and uniform trench width with a deviation of less than 10 nm. The grating height measured with SEM agrees with the fitting within 10%, which could be due to uncertainties of both methods.

Table 7.1. Geometric parameters of the three grating samples AL01, AL02, and AL03.

	AL01	**AL02**	**AL03**
Height h (μm)	1.435	1.275	1.230
Period Λ (μm)	4.025	3.885	3.935
Trench width b (μm)	0.355	0.355	0.355
Filling ratio $(\Lambda - b)/\Lambda$	0.912	0.909	0.910
SEE	0.027	0.034	0.039

Figure 7.4(a) shows the measured reflectance of grating AL01 under in-plane layout, along with the calculation from RCWA from wavenumber of 500 cm^{-1} to 6000 cm^{-1}. The calculated reflectance is for the zeroth diffraction order only. The first and second order MPs (MP1 and MP2), along with three SPPs, appear as dips in the reflectance spectrum as indicated on the figure. In general, the SPP dips are broadened in the FTIR measurements due to the lack of collimation. There is an excellent agreement between the calculation and measurements for the MP1 resonance located around 1396 cm^{-1}. Note that the coupling of MP2 and SPP splits into two resonance peaks from 4000 cm^{-1} to 5000 cm^{-1}.

The split mode has been studied in detail previously [134]. Both dips due to the split mode are clearly captured in the measurement, though there is a slight shift in frequency and the measured dip due to SPP is broader than predicted.

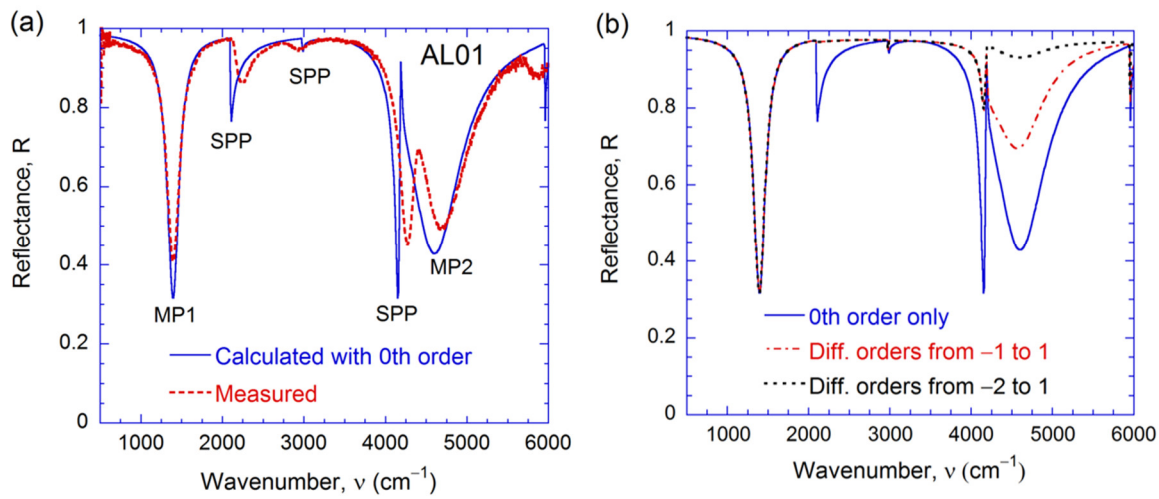

Figure 7.4. (a) Comparison of the measured spectral reflectance of sample AL01 at incidence angle of 10° for the in-plane layout with that calculated considering zeroth-order only and (b) calculated reflectance of sample AL01 considering the zeroth diffraction order plus additional few diffraction orders.

The contributions of different diffraction orders are shown in Figure 7.4(b) by comparison with the cases that include $m = 0$ only, three diffraction orders ($m = -1$, 0, and 1), and four diffraction orders ($m = -2$, -1, 0, and 1). Note that at small wavenumbers, when wavelengths are longer than the grating period, the only propagating mode is the zeroth order ($m = 0$) while all other diffraction modes are evanescent. At around 2100 cm^{-1}, there is dip due to SPP which can be predicted from Eqs. (7.6) and (7.7). When the wavenumber ν exceeds about 2100 cm^{-1}, the diffraction mode with $m = -1$ become propagating, leading to the redistribution of diffraction efficiencies. At $\nu >\approx 3000$ cm^{-1},

the mode with m = 1 becomes propagating. Each SPP mode indicates that an evanescent mode becomes propagating, which is known as Wood's anomaly. As mentioned before, for metallic gratings, the SPP dispersion curves tend to be a straight line, in approximate agreement with Wood's anomaly conditions. At $\nu >\approx$ 4000 cm^{-1}, the mode with m = –2 also becomes propagating. Due to the use of the specular reflectance accessory, only the zeroth order is collected in the measurement since it always diffracts specularly while other orders change the diffracted direction at different wavelengths. Hence, only the zeroth order is considered in the following calculations.

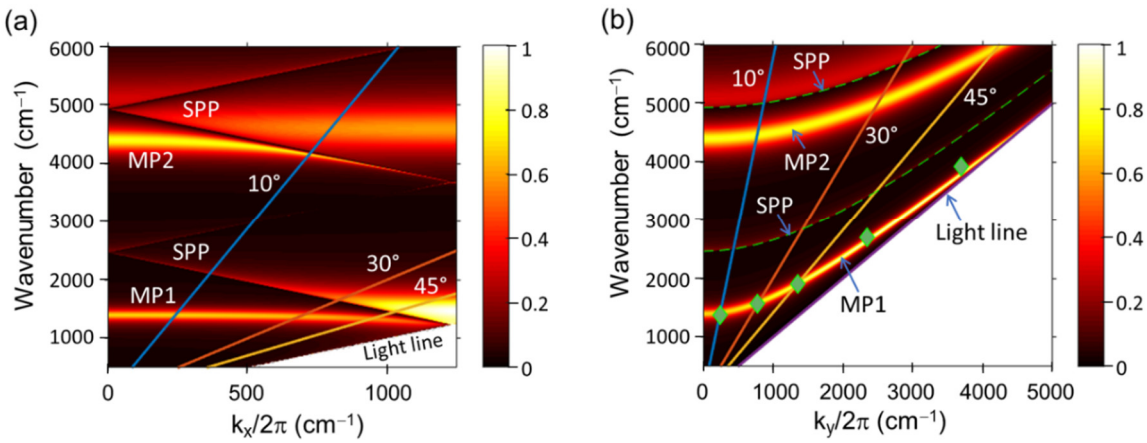

Figure 7.5. Contour plot for $1-R_0$ (where R_0 is the reflectance for the zeroth-order diffraction) for sample AL01 with respect to the wavenumber and the parallel wavevector of the incident wave: (a) in-plane layout and (b) off-plane layout.

The mode coupling and splitting phenomena could be better visualized in Figure 7.5(a), which shows the contour plot of $1-R_0$ for grating AL01 with respect to the wavenumber ν and $k_x = k_0 \sin\theta$ for a TM wave incidence. Here, R_0 stands for the zeroth-order reflectance so the bright lines represent the resonances. The light line corresponds to

$\theta = 90°$. Only the first (half) Brillouin zone is plotted so that $0 < k_x < \pi / \Lambda$, where Λ is the grating period. Since Λ is near 4 μm, the maximum $k_x / 2\pi$ is approximately 1250 cm^{-1} [7]. The inclined lines are for incidence angles at 10°, 30° and 45°. The values for $\theta = 30°$ are shown for $\nu <\approx$ 2500 cm^{-1} and that for $\theta = 45°$ are shown for $\nu <\approx$ 1770 cm^{-1} only. One could fold the line for a given incidence angle to the first Brillouin zone to identify the corresponding resonance modes in the contour plot. Note that mode splitting only happens at MP2 for incidence angle of 10° in the wavenumber range from 4000 cm^{-1} and 5000 cm^{-1}. However, since SPP is angular sensitive while MP is not, at large incidence angles, the mode coupling and splitting can also occur for MP1 because the first SPP will shift towards MP1. This will lead to a mode splitting in MP1 for 1200 cm^{-1} < ν < 1600 cm^{-1} as illustrated in Figure 7.5.

The contour plot of $1 - R_0$ for off-plane layout is shown in Figure 7.5 with respect to the wavenumber and $k_y = k_0 \sin\theta$ since the plane of incidence is the *y*-*z* plane. The incident wave is a TE wave in this case. The grating vector is along the *x*-axis as shown in Fig. 1. Since there is no periodicity in the *y* direction, there is no Brillouin zone in this case, *i.e.*, k_y is infinitely extended. Contrary to the in-plane case, the frequency of MP resonances goes up as the angle of incidence increases. Furthermore, SPP dispersion curves appear to be in parallel with these for the MP modes; hence, no mode splitting can occur. These features can be explained by considering the conical dispersion curves as discussed in the following.

From Eq. (7.9) when $k_{\mathrm{SPP}} \approx k_0$, one obtains $2\pi m / \Lambda = k_0 \cos\theta$ $= (\omega_{\mathrm{SPP}} / c_0)\cos\theta$. Hence,

$$\omega_{\mathrm{SPP}} = \frac{2\pi m c_0}{\Lambda \cos\theta} = \frac{\omega_{\mathrm{SPP},0}}{\cos\theta} \tag{7.10}$$

where $\omega_{\mathrm{SPP},0}$ is the frequency of SPP resonance at normal incidence. Eq.(7.10) provides an approximate expression of the SPP dispersion in the off-plane layout. Since $k_y = k_0 \sin\theta$, the SPP dispersion as shown in Fig. 4(b) can be described by

$$\omega_{\mathrm{SPP},m} = c_0 \sqrt{k_y^2 + \left(\frac{2\pi m}{\Lambda}\right)^2} \tag{7.11}$$

In Figure 7.5(b), the dashed curves are calculated from Eq. (7.11) and agree with the SPP dispersion curves for $m = \pm 1$ and $m = \pm 2$ very well.

It can be seen from Eq. (7.1) that $L_m \propto h$ and from Eq. (7.3) that $C \propto h$. Furthermore, if $2h >> b$, then $L_k \propto h$ according to Eq. (7.2). Therefore, based on Eq. (7.5), the MP resonance frequency (or wavenumber) ν_R is inversely proportional to *h*. If one takes the effective height of the grating for incidence angle θ as $h\cos\theta$, an approximate dispersion relation for MP can be expressed in the following:

$$\nu_{\mathrm{MP},\theta} = \frac{\nu_{\mathrm{MP},0}}{\cos\theta} \tag{7.12}$$

The MP dispersion follows the same curvature as those for SPPs given in Eqs. (7.10) and (7.11). The diamond marks indicate the MP1 resonance frequencies calculated from Eq. (7.12) at $\theta = 10°$, 30°, 45°, 60°, and 80° , using the value at $\theta = 0°$ calculated from Eq. (7.5). It can be seen that Eq. (7.12) gives a good approximation especially for $\theta \le 45°$. Unlike in the in-plane layout, the MP and SPP dispersions are nearly parallel to each other, as evidenced in Figure 7.5(b). This is a unique feature of off-plane layout that has not been

studied previously. One could also interpret the effect of angle of incidence for off-plane layout as due to the reduction of the magnetic flux with increasing θ values.

The measured and calculated reflectance spectra for the zeroth order at $\theta = 10°, 30°$, and 45° are shown in Figure 7.6 for both in-plane and off-plane layouts. Note again that the reflectance is for the zeroth diffraction order only. The incident wave is a TM wave for the in-plane cases displayed in Figure 7.6(a-c); while the incident wave is a TE wave for off-plane cases displayed Figure 7.6(d-f). The agreement between the measurements and calculation is excellent at $\nu < 3500\ \text{cm}^{-1}$, where MP1 and the first few SPP modes exist. Deviations occur at high-order resonances. Nevertheless, the general trends agree very well for both layouts. For in-plane layout at $\theta = 30°$ and 45°, MP1 is coupled with SPP and both peaks have been observed in the experiments, which agree very well with the prediction. This coupling and splitting can be seen from Figure 7.6(a) in the lower-right portion of the contour plot.

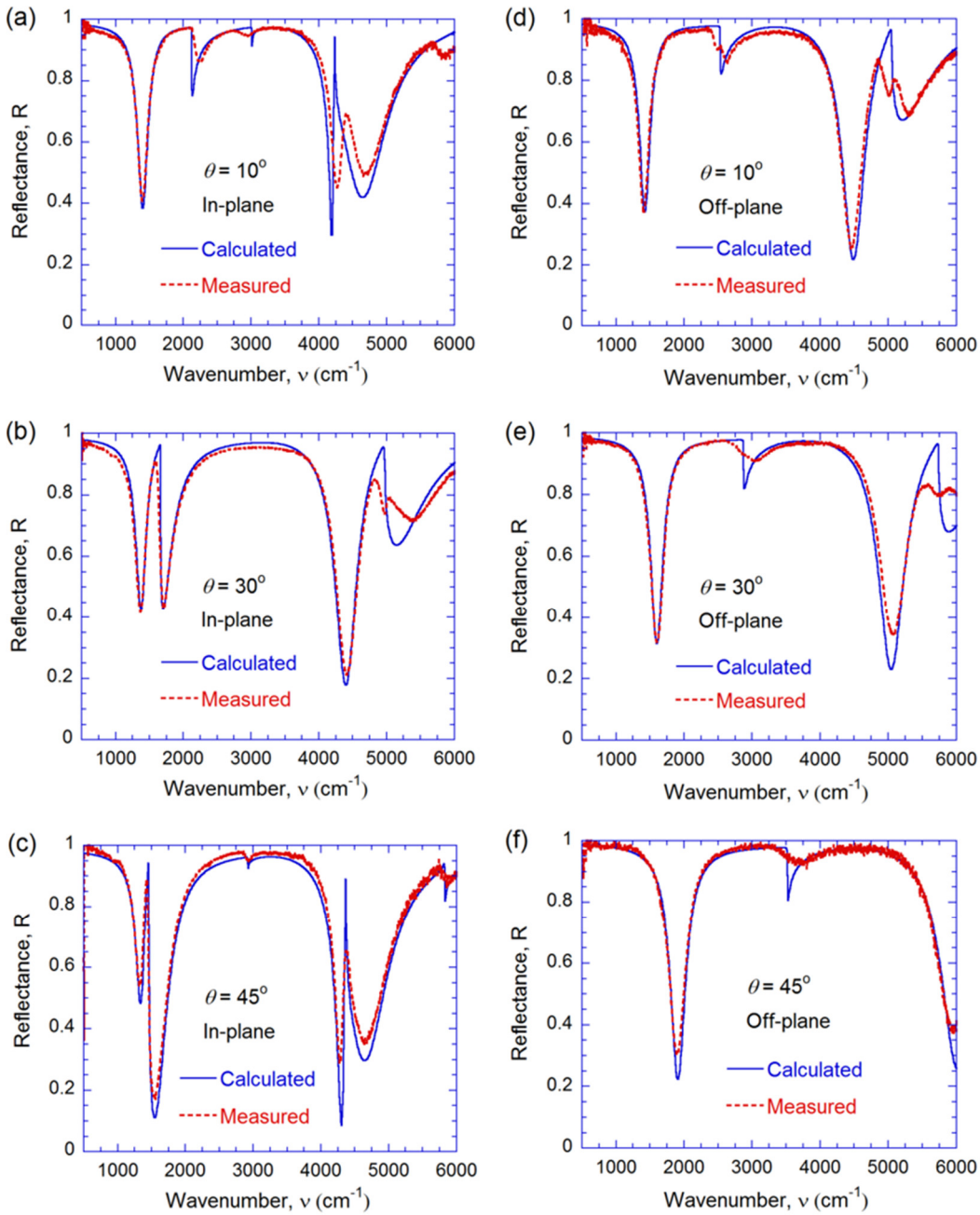

Figure 7.6. Comparison of calculated and measured reflectance of sample AL01: (a)–(c) in-plane layout with θ = 10°, 30°, and 45°, respectively, for TM wave incidence; (d)–(f) off-plane layout with θ = 10°, 30°, and 45°, respectively, for TE wave incidence.

The resonant frequencies of MP1 of all three gratings at various incidence angles are summarized in Table 7.2, for the in-plane layout, along with the calculated results from RCWA and LC-circuit model. Note that LC-circuit model does not consider the mode coupling with SPP and therefore gives the same frequency at different angles. The measured results agree well with the calculation from RCWA within 0.2% for sample AL01 at all incidence angles and within 0.4% for samples AL02 and AL03 at $\theta = 10°$. Even at $\theta = 30°$ and 45° for samples AL02 and AL03, the maximum relative difference is less than 3%.

Table 7.2. MP1 resonant frequency in (cm^{-1}) obtained from the measurement and modeling for the in-plane layout.

	AL01	**AL02**	**AL03**
Measurement			
10°	1396	1535	1582
30°	1369	1481	1504
45°	1333	1393	1404
RCWA			
10°	1396	1541	1582
30°	1372	1500	1527
45°	1332	1430	1435
LC-Circuit Model			
	1393	1589	1592

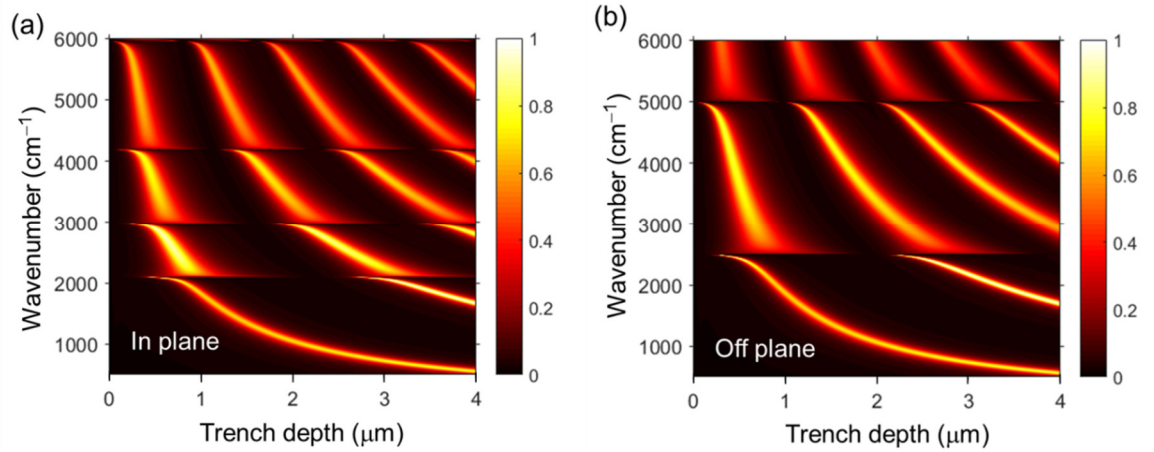

Figure 7.7. Contour plot for $1-R_0$ calculated with varying trench depth (or grating height) when the rest parameters are fixed as for AL01: (a) in-plane layout for TM wave incidence and (b) off-plane layout for TE wave incidence.

Figure 7.7 shows the contour plot of $1-R_0$ with respect to wavenumber and the trench depth for both layouts at $\theta =$ 10°. Note that the MP resonance frequency should vary inversely with h. From the left to the right, one can see MP of order 1, 2, 3, 4 and 5. These MP branches are broken at each SPP modes corresponding to m = -1, 1, -2 in Eq. (7.7) for the in-plane layout and $m = \pm 1$ and ± 2 in Eq. (7.9) for the off-plane layout. Even for the off-plane layout, if the MP and SPP are very close, mode coupling and splitting can occur. However, their branches will be two nearly parallel curves following the similar trend as shown in Figure 7.7(b). Figure 7.7 suggests that the MP resonance can occur with relatively shallow gratings at high frequencies and the resonance frequency is very sensitive to the height of the grating. Furthermore, the frequency range where R_0 is small (bright region) becomes boarder with shallower gratings.

CHAPTER 8

CONCLUSIONS AND FUTURE WORK

This dissertation investigates the thermal radiative properties of dispersed medium and periodic micro-fabricated gratings both theoretically and experimentally. The radiative properties of three dense ceramic Al_2O_3, AlN, and Si_3N_4 plates are investigated from the visible to the mid-infrared region at room temperature. In the visible and near-infrared region up to about $\lambda = 4$ μm, alumina is essentially nonabsorbing, and volume scattering dominates the radiative properties. Aluminum nitride resembles alumina but with some absorption, which increases in the infrared toward shorter wavelengths. For both of these two samples, volume scattering plays a significant role to enhance the diffuse reflectance, resulting in a high directional-hemispherical reflectance. The scattering coefficients of both of them are retrieved using inverse adding-doubling (IAD) method, which shows that Al_2O_3 has a much higher scattering coefficient than AlN, especially in the visible and near infrared. This can be explained by the finer particles (pores) with a diameter of about a quarter of a micrometer, and verified using Mie theory. The absorption coefficient of Al_2O_3 increases rapidly with wavelength in the mid-infrared region from $\lambda \approx 4$ μm. This is in quantitative agreement with the absorption edge of Al_2O_3 crystals due to lattice vibrations. For AlN, the absorption coefficient increases toward shorter wavelengths in the visible region due to bandgap absorption and toward longer wavelengths at $\lambda > 4$ μm due to phonon absorption. For the opaque silicon nitride sample, volume scattering is insignificant and only slightly increases the directional-hemispherical reflectance. The absorptance of the Si_3N_4 sample in the visible and near-infrared regions is marginally greater for the rough

side than for the smooth side. For all three samples, the measured specular reflectance of the smooth side is lower than calculated reflectance of perfectly smooth surfaces due to surface scattering, which becomes dominant at shorter wavelengths.

In the mid-infrared, phonon bands and the Christiansen effect are observed for the three ceramic materials. While the reflectance for the smooth side is similar to previously reported crystalline and ceramic Al_2O_3 as well as crystalline AlN plates, the reflectance of the Si_3N_4 sample appears to be much higher than both the existing measurements and predictions from the dielectric function models. The phonon parameters and dielectric function of the (poly)crystalline Si_3N_4 are obtained using Lorentz oscillator model. The infrared optical constants of ceramic Si_3N_4 are shown to be distinctively different from those of its amorphous counterpart that were studied by others. In the reststrahlen band, volume scattering gives rise to a diffuse reflectance component that is usually much smaller than the specular component. However, surface roughness can significantly reduce the reflectance, especially for the AlN sample. Knowledge gained from the present study may facilitate the heat transfer analysis and design in thermal systems and optoelectronic devices when these refractive ceramic materials are used.

The observed enhanced directional-hemispherical reflectance in Al_2O_3 and AlN plates, which results from volumetric scattering, has inspired the design of a solar reflector. Consisting of a submillimeter PTFE sheet atop a silver thin film, the designed reflector demonstrates a very high diffuse reflectance in the solar spectrum. The integrated reflectance of a 0.24 mm thick PTFE film with the Ag reflector is 0.991, which is the highest value reported to date for any natural or artificial materials. The scattering and absorption coefficients of PTFE are extracted using IAD and applied in the Monte Carlo

ray tracing simulation and a modified two-flux model to predict the reflectance of the PTFE with and without the Ag reflector. The theoretical analysis offers insight of the radiative properties of sintered PTFE and the underlying principles of the dual-layer design. Furthermore, the high emittance of PTFE in the mid-infrared wavelengths beyond the solar spectrum is useful for sky radiative cooling. Therefore, the dual-layer structure holds great promise to achieve daytime radiative cooling or refrigeration under direct solar irradiation for building energy saving and outdoor thermal management.

The bidirectional radiative properties of the proposed solar reflector are investigated in a follow-up study. The bidirectional reflectance and transmittance distribution functions of PTFE at various incidence angles are measured with a laser scatterometer at 635 nm wavelength. It is found that placing the Ag film on the back does not leads to a new specular peak, because the thickness of even the thinnest sample is much greater than the photon penetration depth. Nevertheless, it is observed that the reflection is nearly diffuse only when the incidence angle is small, a significant specular component is observed at oblique incidence. The surface roughness may affect the radiative properties and for a polished surface, some specular reflection is observed even at small incidence angles. The previous Monte Carlo ray-tracing algorithm is modified to incorporate both surface scattering and volumetric scattering to model the bidirectional radiative properties. Different surface roughness parameters are used to simulate the BRDF and the calculation can capture the main trend observed in the experiments. Further, the model is used to study the thickness effect by modeling PTFE sheets with much smaller thicknesses than those obtained experimentally. This allows the determination of the limiting thickness when specular reflection becomes important or even dominates. The findings of this work help

understand the bidirectional radiative properties of dispersed media, which have been used for passive radiative cooling in many recent studies. The method presented here can facilitate the design of nearly diffuse reflectors for these applications.

This dissertation also investigates the thermal radiative properties of micro-structured materials. The resonance absorption or emission by exciting MPs in deep metal gratings is experimentally demonstrated. The measured specular reflectance in the near- and mid-infrared region can be well described by the RCWA model for different incidence angles, polarizations, and grating orientations. Furthermore, the fundamental MP resonance can be predicted with the LC-circuit model. MPs in both in-plane layout and off-plane layout are measured and analyzed. The mechanism for the shift of MP resonance is attributed to mode coupling with SPP for in-plane layout, and due to change of the lateral component of magnetic field for off-plane layout. This work shows, for the first time, the nearly parallel dispersion curves of SPPs and MPs in the off-plane layout both theoretically and experimentally. The effect of trench depth is also investigated and the mode splitting at the corresponding SPP is described. This study experimentally verified the theory of MP in deep gratings and extended the discussion to the off-plane layout. The finding of this study can benefit the future design of spectrally and directionally selective thermal emitters and absorbers based on metallic gratings.

In this dissertation, detailed analysis and experimental results of thermal radiative properties of randomly dispersed medium and periodic micro gratings are presented, which could facilitate the design and application of novel materials that can hugely impact areas such energy conversion, nanophotonics, sensing, etc., with their tailored radiative properties. Following the project of the metallic grating, the next step is to study the

plasmonic coupling of gratings and 2D materials such as graphene, hBN by transferring them on top of the grating, as proposed by Zhao and Zhang [40, 92]. Gratings have been redesigned and fabricated for this purpose and preliminary results of graphene transfer are obtained. This graphene-grating structure is an ideal candidate of ultrafast optoelectronic devices due to the enhanced absorptance from MP resonance, while the resonance frequency can be tuned by the grating structure. For broadband photon absorption, which can be used in solar absorption, spectroscopy and energy harvesting, the metallic surface can be randomized with steep-edged roughness, forming a broad spectrum of resonance modes which couple with the graphene on top.

For the design of the solar reflector, it is realized that the binding of the PTFE sample with the metal film is the limiting factor. The problem can be overcome by replacing PTFE films with non-absorbing porous polymer coatings that can be sprayed onto metal surfaces. The feature size of the polymer coating should be reduced to produce higher scattering coefficient, thus reducing the coating thickness required. For mass production, the silver film can be replaced with aluminum films which has similar radiative properties in the infrared region. Outdoor testing is to be performed to experimentally demonstrate the high solar reflectance and radiative cooling effect of the designed structure.

REFERENCES

[1] S. Basu, Y.-B. Chen, Z.M. Zhang, Microscale radiation in thermophotovoltaic devices—A review, Int. J. Energ. Res., 31(6-7) (2007) 689-716.

[2] L. Zhou, Y. Tan, D. Ji, B. Zhu, P. Zhang, J. Xu, Q. Gan, Z. Yu, J. Zhu, Self-assembly of highly efficient, broadband plasmonic absorbers for solar steam generation, Sci. Adv., 2(4) (2016) e1501227.

[3] K.R. Catchpole, A. Polman, Plasmonic solar cells, Opt. Express, 16(26) (2008) 21793-21800.

[4] D. Schurig, J.J. Mock, B.J. Justice, S.A. Cummer, J.B. Pendry, A.F. Starr, D.R. Smith, Metamaterial electromagnetic cloak at microwave frequencies, Science, 314(5801) (2006) 977-980.

[5] Y. Cui, Q. Wei, H. Park, C.M. Lieber, Nanowire nanosensors for highly sensitive and selective detection of biological and chemical species, Science, 293(5533) (2001) 1289-1292.

[6] N. Fang, H. Lee, C. Sun, X. Zhang, Diffraction-limited optical imaging with a silver superlens, Science, 308(5721) (2005) 534-537.

[7] Z. Zhang, Nano/Microscale Heat Transfer, McGrawl-Hill, New York, 2007.

[8] F. Gervais, Aluminum Oxide(Al2O3), in: E.D. Palik (Ed.) Handbook of Optical Constants of Solids, Academic press, San Diego, CA, 1998, pp. 761-775.

[9] W.J. Tropf, M.E. Thomas, in: E.D. Palik (Ed.) Handbook of Optical Constants of Solids, Academic press, San Diego, CA, 1998, pp. 653-681.

[10] J. Manara, R. Caps, F. Raether, J. Fricke, Characterization of the pore structure of alumina ceramics by diffuse radiation propagation in the near infrared, Opt. Commun., 168(1) (1999) 237-250.

[11] O. Rozenbaum, D. De Sousa Meneses, P. Echegut, Texture and porosity effects on the thermal radiative behavior of alumina ceramics, Int. J. Thermophys., 30(2) (2009) 580-590.

[12] C.A. Worrell, Infrared optical constants for CO2 laser waveguide materials, J. Mater. Sci., 21(3) (1986) 781-787.

[13] R. Apetz, M.P.B. van Bruggen, Transparent alumina: a light-scattering model, J. Am. Ceram. Soc., 86(3) (2003) 480-486.

[14] A.T. Collins, E.C. Lightowlers, P.J. Dean, Lattice vibration spectra of aluminum nitride, Phys. Rev., 158(3) (1967) 833-838.

[15] W.J. Moore, J.A.F. Jr., R.T. Holm, O. Kovalenkov, V. Dmitriev, Infrared dielectric function of wurtzite aluminum nitride, Appl. Phys. Lett., 86(14) (2005) 141912.

[16] S. Loughin, R.H. French, in: E.D. Palik (Ed.) Handbook of Optical Constants of Solids, Academic press, San Diego, CA, 1998, pp. 373-401.

[17] D.J. Jones, R.H. French, H. Müllejans, S. Loughin, A.D. Dorneich, P.F. Carcia, Optical properties of AlN determined by vacuum ultraviolet spectroscopy and spectroscopic ellipsometry data, J. Mater. Res., 14(11) (2011) 4337-4344.

[18] H.R. Philipp, in: E.D. Palik (Ed.) Handbook of optical constants of solids, Academic press, San Diego, CA, 1998, pp. 771-774.

[19] M. Klanjšek Gunde, M. Maček, Infrared optical constants and dielectric response functions of silicon nitride and oxynitride films, Phys. Status Solidi A, 183(2) (2001) 439-449.

[20] G. Cataldo, J.A. Beall, H.-M. Cho, B. McAndrew, M.D. Niemack, E.J. Wollack, Infrared dielectric properties of low-stress silicon nitride, Opt. Lett., 37(20) (2012) 4200-4202.

[21] F.L. Riley, Silicon nitride and related materials, J. Am. Ceram. Soc., 83(2) (2000) 245-265.

[22] T. Flaherty, P.V. Kelly, S. Lynch, R.T. Cundill, M.O. Keeffe, G.M. Crean, in: S. Somiya (Ed.) Advanced Materials' 93: Ceramics, Powders, Corrosion and Advanced Processing, Newnes, Tokyo, Japan, 1993, pp. 937-940.

[23] J.R. Howell, M.P. Menguc, R. Siegel, Thermal Radiation Heat Transfer, CRC press, 2015.

[24] L. Novotny, B. Hecht, Principles of Nano-Optics, Cambridge University Press, 2012.

[25] L. Wang, Role of magnetic resonance and wave interference in tailoring the radiative properties of micro/nanostructures, Georgia Institute of Technology, 2011.

[26] A. Poddubny, I. Iorsh, P. Belov, Y. Kivshar, Hyperbolic metamaterials, Nat. Photonics, 7 (2013) 948.

[27] A. Alù, M.G. Silveirinha, A. Salandrino, N. Engheta, Epsilon-near-zero metamaterials and electromagnetic sources: Tailoring the radiation phase pattern, Phys. Rev. B, 75(15) (2007) 155410.

[28] J.D. Joannopoulos, S.G. Johnson, J.N. Winn, R.D. Meade, Photonic Crystals: Molding the Flow of Light, 2nd ed., Princeton University Press, New Jersey, 2011.

[29] X. Wang, Study of the radiative properties of aligned carbon nanotubes and silver nanorods, Georgia Institute of Technology, 2011.

[30] M.I. Mishchenko, Multiple scattering, radiative transfer, and weak localization in discrete random media: Unified microphysical approach, Rev. Geophys., 46(2) (2008).

[31] M.F. Modest, Radiative Heat Transfer, Academic press, Boston, 2013.

[32] J.B. Pendry, Negative refraction makes a perfect lens, Phys. Rev. Lett., 85(18) (2000) 3966-3969.

[33] C.F. Bohren, How can a particle absorb more than the light incident on it?, Am. J. Phys., 51(4) (1983) 323-327.

[34] W.L. Barnes, A. Dereux, T.W. Ebbesen, Surface plasmon subwavelength optics, Nature, 424(6950) (2003) 824-830.

[35] J.B. Pendry, A.J. Holden, D.J. Robbins, W.J. Stewart, Magnetism from conductors and enhanced nonlinear phenomena, IEEE T. Microw. Theory, 47(11) (1999) 2075-2084.

[36] B.J. Lee, L.P. Wang, Z.M. Zhang, Coherent thermal emission by excitation of magnetic polaritons between periodic strips and a metallic film, Opt. Express, 16(15) (2008) 11328-11336.

[37] L.P. Wang, Z.M. Zhang, Measurement of coherent thermal emission due to magnetic polaritons in subwavelength microstructures, J. Heat. Transf., 135(9) (2013) 091505-091505-091509.

[38] H. Liu, T. Li, Q.J. Wang, Z.H. Zhu, S.M. Wang, J.Q. Li, S.N. Zhu, Y.Y. Zhu, X. Zhang, Extraordinary optical transmission induced by excitation of a magnetic plasmon propagation mode in a diatomic chain of slit-hole resonators, Phys. Rev. B, 79(2) (2009) 024304.

[39] X.L. Liu, B. Zhao, Z.M. Zhang, Blocking-assisted infrared transmission of subwavelength metallic gratings by graphene, J. Opt., 17(3) (2015) 035004.

[40] B. Zhao, Z.M. Zhang, Strong plasmonic coupling between graphene ribbon array and metal gratings, ACS Photonics, 2(11) (2015) 1611-1618.

[41] B. Zhao, Thermal radiative properties of micro/nanostructured plasmonic metamaterials including two-dimensional materials, Georgia Institute of Technology, 2016.

[42] F.E. Nicodemus, Reflectance nomenclature and directional reflectance and emissivity, Appl. Opt., 9(6) (1970) 1474-1475.

[43] Y.J. Shen, Q.Z. Zhu, Z.M. Zhang, A scatterometer for measuring the bidirectional reflectance and transmittance of semiconductor wafers with rough surfaces, Rev. Sci. Instrum., 74(11) (2003) 4885-4892.

[44] D. Geisler-Moroder, A. Dür, A new Ward BRDF model with bounded albedo, Computer Graphics Forum, 29(4) (2010) 1391-1398.

[45] C. Donner, H.W. Jensen, Light diffusion in multi-layered translucent materials, ACM Trans. Graph., 24(3) (2005) 1032-1039.

[46] A. Ishimaru, Diffusion of light in turbid material, Appl. Opt., 28(12) (1989) 2210-2215.

[47] A. Ishimaru, Diffusion of a pulse in densely distributed scatterers, J. Opt. Soc. Am., 68(8) (1978) 1045-1050.

[48] A. Schuster, Radiation through a foggy atmosphere, Astrophys. J., 21 (1905) 1.

[49] P. Kubelka, New contributions to the optics of intensely light-scattering materials. part I, J. Opt. Soc. Am., 38(5) (1948) 448-457.

[50] Q. Li, Light scattering of semitransparent media, Georgia Institute of Technology, 2008.

[51] L. Dombrovsky, J. Randrianalisoa, D. Baillis, Modified two-flux approximation for identification of radiative properties of absorbing and scattering media from directional-hemispherical measurements, J. Opt. Soc. Am. A, 23(1) (2006) 91-98.

[52] P. Yang, C. Chen, Z.M. Zhang, A dual-layer structure with record-high solar reflectance for daytime radiative cooling, Sol. Energy, 169 (2018) 316-324.

[53] S. Chandrasekhar, Radiative Transfer, Dover Publications, New York, 1960.

[54] A. Prokhorov, Effective emissivities of isothermal blackbody cavities calculated by the Monte Carlo method using the three-component bidirectional reflectance distribution function model, Appl. Opt., 51(13) (2012) 2322-2332.

[55] A. Prokhorov, L.M. Hanssen, Numerical modeling of an integrating sphere radiation source, in: Modeling and Characterization of Light Sources, International Society for Optics and Photonics, 2002, pp. 106-119.

[56] L. Wang, S.L. Jacques, L. Zheng, MCML—Monte Carlo modeling of light transport in multi-layered tissues, Comput. Meth. Prog. Bio., 47(2) (1995) 131-146.

[57] Q. Li, B.-J. Lee, Z.M. Zhang, D.W. Allen, Light scattering of semitransparent sintered polytetrafluoroethylene films, J. Biomed. Opt., 13(5) (2008) 054064.

[58] Y. Zhao, G.H. Tang, M. Du, Numerical study of radiative properties of nanoporous silica aerogel, Int. J. Therm. Sci., 89 (2015) 110-120.

[59] H.C. van de Hulst, Multiple Light Scattering: Tables, Formulas and Applications, Academic Press, 1980.

[60] S.A. Prahl, The Adding-Doubling Method, in: A.J. Welch, M.J.C. Van Gemert (Eds.) Optical-Thermal Response of Laser-Irradiated Tissue, Springer US, Boston, MA, 1995, pp. 101-129.

[61] S.A. Prahl, M.J.C. van Gemert, A.J. Welch, Determining the optical properties of turbid media by using the adding–doubling method, Appl. Opt., 32(4) (1993) 559-568.

[62] M.I. Mishchenko, G. Videen, V.A. Babenko, N.G. Khlebtsov, T. Wriedt, T-matrix theory of electromagnetic scattering by partciles and its applications: a comprehensive reference database, J. Quant. Spectrosc. Radiat. Transf., 88(1) (2004) 357-406.

[63] C.F. Bohren, D.R. Huffman, Absorption and scattering of light by small particles, John Wiley & Sons, 2008.

[64] C.-L. Tien, B. Drolen, Thermal radiation in particulate media with dependent and independent scattering, Annu. Rev. Heat Transf., 1(1) (1987).

[65] A.W. Harrison, M.R. Walton, Radiative cooling of TiO2 white paint, Sol. Energy, 20(2) (1978) 185-188.

[66] S. Catalanotti, V. Cuomo, G. Piro, D. Ruggi, V. Silvestrini, G. Troise, The radiative cooling of selective surfaces, Sol. Energy, 17(2) (1975) 83-89.

[67] M.M. Hossain, M. Gu, Radiative cooling: principles, progress, and potentials, Adv. Sci., 3(7) (2016) 1500360.

[68] Data from Gemini Observatory, IR Trasmission Spectra, available at http://www.gemini.edu/sciops/telescopes-and-sites/observing-condition-constraints/ir-transmission-spectra, last accessed in September 9, 2017

[69] Standard Tables for Reference Solar Spectral Irradiances: Direct Normal and Hemispherical on 37° Tilted Surface, in, ASTM International, West Conshocken, PA, USA., 2012.

[70] Y. Zhai, Y. Ma, S.N. David, D. Zhao, R. Lou, G. Tan, R. Yang, X. Yin, Scalable-manufactured randomized glass-polymer hybrid metamaterial for daytime radiative cooling, Science, 355 (2017) 1062-1066.

[71] Z. Chen, L. Zhu, A. Raman, S. Fan, Radiative cooling to deep sub-freezing temperatures through a 24-h day–night cycle, Nat. Commun., 7 (2016) 13729.

[72] B. Orel, M.K. Gunde, A. Krainer, Radiative cooling efficiency of white pigmented paints, Sol. Energy, 50(6) (1993) 477-482.

[73] H. Bao, C. Yan, B. Wang, X. Fang, C.Y. Zhao, X. Ruan, Double-layer nanoparticle-based coatings for efficient terrestrial radiative cooling, Sol. Energ. Mat. Sol. C., 168(Supplement C) (2017) 78-84.

[74] T.M.J. Nilsson, G.A. Niklasson, Radiative cooling during the day: simulations and experiments on pigmented polyethylene cover foils, Sol. Energ. Mat. Sol. C., 37(1) (1995) 93-118.

[75] A.P. Raman, M.A. Anoma, L. Zhu, E. Rephaeli, S. Fan, Passive radiative cooling below ambient air temperature under direct sunlight, Nature, 515 (2014) 540.

[76] J. Mandal, Y. Fu, A.C. Overvig, M. Jia, K. Sun, N.N. Shi, H. Zhou, X. Xiao, N. Yu, Y. Yang, Hierarchically porous polymer coatings for highly efficient passive daytime radiative cooling, Science, 362(6412) (2018) 315-319.

[77] A.R. Gentle, G.B. Smith, A subambient open roof surface under the mid-summer sun, Adv. Sci., 2(9) (2015) 1500119.

[78] Z. Huang, X. Ruan, Nanoparticle embedded double-layer coating for daytime radiative cooling, Int. J. Heat. Mass. Tran., 104 (2017) 890-896.

[79] S. Atiganyanun, J.B. Plumley, S.J. Han, K. Hsu, J. Cytrynbaum, T.L. Peng, S.M. Han, S.E. Han, Effective radiative cooling by paint-format microsphere-based photonic random media, ACS Photonics, 5(4) (2018) 1181-1187.

[80] P.Y. Barnes, E.A. Early, A.C. Parr, N.I.o. Standards, Technology, NIST Measurement Services: Spectral Reflectance, National Institute of Standards and Technology, 1998.

[81] V.R. Weidner, J.J. Hsia, Reflection properties of pressed polytetrafluoroethylene powder, J. Opt. Soc. Am., 71(7) (1981) 856-861.

[82] M.G. Moharam, T.K. Gaylord, Rigorous coupled-wave analysis of planar-grating diffraction, J. Opt. Soc. Am., 71(7) (1981) 811-818.

[83] M.G. Moharam, E.B. Grann, D.A. Pommet, T.K. Gaylord, Formulation for stable and efficient implementation of the rigorous coupled-wave analysis of binary gratings, J. Opt. Soc. Am. A, 12(5) (1995) 1068-1076.

[84] L. Li, Use of Fourier series in the analysis of discontinuous periodic structures, J. Opt. Soc. Am. A, 13(9) (1996) 1870-1876.

[85] E.N. Glytsis, T.K. Gaylord, Three-dimensional (vector) rigorous coupled-wave analysis of anisotropic grating diffraction, J. Opt. Soc. Am. A, 7(8) (1990) 1399-1420.

[86] R.A. Shelby, D.R. Smith, S. Schultz, Experimental verification of a negative index of refraction, Science, 292(5514) (2001) 77-79.

[87] P. Yang, H. Ye, Z.M. Zhang, Experimental demonstration of the effect of magnetic polaritons on the radiative properties of deep aluminum gratings, J. Heat. Transf., 141(5) (2019) 052702.

[88] L.P. Wang, Z.M. Zhang, Wavelength-selective and diffuse emitter enhanced by magnetic polaritons for thermophotovoltaics, Appl. Phys. Lett., 100(6) (2012) 063902.

[89] N. Mattiucci, G. D'Aguanno, A. Alù, C. Argyropoulos, J.V. Foreman, M.J. Bloemer, Taming the thermal emissivity of metals: A metamaterial approach, Appl. Phys. Lett., 100(20) (2012) 201109.

[90] B. Zhao, Z.M. Zhang, Study of magnetic polaritons in deep gratings for thermal emission control, J. Quant. Spectrosc. Radiat. Transf., 135 (2014) 81-89.

[91] L.P. Wang, Z.M. Zhang, Resonance transmission or absorption in deep gratings explained by magnetic polaritons, Appl. Phys. Lett., 95(11) (2009) 111904.

[92] B. Zhao, Z.M. Zhang, Perfect mid-infrared absorption by hybrid phonon-plasmon polaritons in hBN/metal-grating anisotropic structures, Int. J. Heat. Mass. Tran., 106 (2017) 1025-1034.

[93] H. Lee, Radiative properties of silicon wafers with microroughness and thin-film coatings, Georgia Institute of Technology, 2006.

[94] X.J. Wang, J.D. Flicker, B.J. Lee, W.J. Ready, Z.M. Zhang, Visible and near-infrared radiative properties of vertically aligned multi-walled carbon nanotubes, Nanotechnology, 20(21) (2009) 215704.

[95] L. Hanssen, Integrating-sphere system and method for absolute measurement of transmittance, reflectance, and absorptance of specular samples, Appl. Opt., 40(19) (2001) 3196-3204.

[96] Q. Cheng, P. Yang, Z. Zhang, Radiative properties of ceramic Al_2O_3, AlN, and Si_3N_4: I. experiments, Int. J. Thermophys., 37(6) (2016) 62.

[97] P.R. Griffiths, J.A. De Haseth, Fourier Transform Infrared Spectrometry, Wiley, New York, 1986.

[98] J.E. Proctor, P. Yvonne Barnes, NIST high accuracy reference reflectometer-spectrophotometer, J. Res. Natl. Inst. Stan., 101(5) (1996) 619-627.

[99] H.J. Lee, A.C. Bryson, Z.M. Zhang, Measurement and modeling of the emittance of silicon wafers with anisotropic roughness, Int. J. Thermophys., 28(3) (2007) 918-933.

[100] X.J. Wang, J.L. Abell, Y.P. Zhao, Z.M. Zhang, Angle-resolved reflectance of obliquely aligned silver nanorods, Appl. Opt., 51(10) (2012) 1521-1531.

[101] Q.Z. Zhu, Z.M. Zhang, Anisotropic slope distribution and bidirectional reflectance of a rough silicon surface, J. Heat. Transf., 126(6) (2005) 985-993.

[102] D.W. Lynch, W.R. Hunter, Comments on the Optical Constants of Metals and an Introduction to the Data for Several Metals, in: E.D. Palik (Ed.) Handbook of Optical Constants of Solids, San Diego, CA, Academic Press, 1998, pp. 275-367.

[103] J.I. Watjen, T.J. Bright, Z.M. Zhang, C. Muratore, A.A. Voevodin, Spectral radiative properties of tungsten thin films in the infrared, Int. J. Heat. Mass. Tran., 61 (2013) 106-113.

[104] J. Kischkat, S. Peters, B. Gruska, M. Semtsiv, M. Chashnikova, M. Klinkmüller, O. Fedosenko, S. Machulik, A. Aleksandrova, G. Monastyrskyi, Mid-infrared optical properties of thin films of aluminum oxide, titanium dioxide, silicon dioxide, aluminum nitride, and silicon nitride, Appl. Opt., 51(28) (2012) 6789-6798.

[105] N. Wada, S.A. Solin, J. Wong, S. Prochazka, Raman and IR absorption spectroscopic studies on α, β, and amorphous Si3N4, J. Non-cryst. Solids, 43(1) (1981) 7-15.

[106] Y. Cai, L. Zhang, Q. Zeng, L. Cheng, Y. Xu, First-principles study of vibrational and dielectric properties of β Si3N4, Phys. Rev. B, 74(17) (2006) 174301.

[107] P. Yang, Q. Cheng, Z. Zhang, Radiative properties of ceramic Al_2O_3, AlN and Si_3N_4—II: modeling, Int. J. Thermophys., 38(8) (2017) 124.

[108] H.J. Lee, B.J. Lee, Z.M. Zhang, Modeling the radiative properties of semitransparent wafers with rough surfaces and thin-film coatings, J. Quant. Spectrosc. Radiat. Transf., 93(1) (2005) 185-194.

[109] J.P. Heather, M.H. Leonard, Z. Jinan, A.G. Thomas, BRDF measurements of graphite used in high-temperature fixed point blackbody radiators: a multi-angle study at 405 nm and 658 nm, Metrologia, 49(2) (2012) S81.

[110] K.E. Torrance, E.M. Sparrow, Theory for off-specular reflection from roughened surfaces, J. Opt. Soc. Am., 57(9) (1967) 1105-1114.

[111] H. Ehrenreich, H.R. Philipp, Optical properties of Ag and Cu, Phys. Rev., 128(4) (1962) 1622-1629.

[112] P.B. Johnson, R.W. Christy, Optical constants of the noble metals, Phys. Rev. B, 6(12) (1972) 4370-4379.

[113] S. Babar, J.H. Weaver, Optical constants of Cu, Ag, and Au revisited, Appl. Opt., 54(3) (2015) 477-481.

[114] M.K. Yang, R.H. French, E.W. Tokarsky, Optical properties of Teflon AF amorphous fluoropolymers, J. Micro-nanolith. Mem., 7(3) (2008) 033010.

[115] E.H. Korte, A. Röseler, Infrared ellipsometric determination of the optical constants of polytetrafluoroethylene, J. Mol. Struct., 661 (2003) 579-585.

[116] J. Song, J. Qin, J. Qu, Z. Song, W. Zhang, X. Xue, Y. Shi, T. Zhang, W. Ji, R. Zhang, H. Zhang, Z. Zhang, X. Wu, The effects of particle size distribution on the optical properties of titanium dioxide rutile pigments and their applications in cool non-white coatings, Sol. Energ. Mat. Sol. C., 130 (2014) 42-50.

[117] S.D. Lord, A new software tool for computing Earth's atmospheric transmission of near-and far-infrared radiation, NASA Technical Memorandum 103957 (1992).

[118] M. Martin, P. Berdahl, Summary of results from the spectral and angular sky radiation measurement program, Sol. Energy, 33(3) (1984) 241-252.

[119] Y.H. Zhou, Z.M. Zhang, Radiative properties of semitransparent silicon wafers with rough surfaces, J. Heat. Transf., 125(3) (2003) 462-470.

[120] I. Lux, L.s. Koblinger, Monte Carlo Particle Transport Methods : Neutron and Photon Calculations, CRC Press, Boca Raton, 1991.

[121] J.A. Sánchez-Gil, M. Nieto-Vesperinas, Light scattering from random rough dielectric surfaces, J. Opt. Soc. Am. A, 8(8) (1991) 1270-1286.

[122] M. Sanamzadeh, L. Tsang, J.T. Johnson, R.J. Burkholder, S. Tan, Scattering of electromagnetic waves from 3D multilayer random rough surfaces based on the second-order small perturbation method: energy conservation, reflectivity, and emissivity, J. Opt. Soc. Am. A, 34(3) (2017) 395-409.

[123] L. Tsang, J.A. Kong, Scattering of Electromagnetic Waves: Advanced Topics, John Wiley & Sons, 2004.

[124] K. Tang, R.A. Dimenna, R.O. Buckius, Regions of validity of the geometric optics approximation for angular scattering from very rough surfaces, Int. J. Heat. Mass. Tran., 40(1) (1996) 49-59.

[125] K. Tang, R.O. Buckius, A statistical model of wave scattering from random rough surfaces, Int. J. Heat. Mass. Tran., 44(21) (2001) 4059-4073.

[126] A.V. Prokhorov, L.M. Hanssen, Algorithmic model of microfacet BRDF for Monte Carlo calculation of optical radiation transfer, in: Optical Science and Technology, SPIE's 48th Annual Meeting, SPIE, 2003, pp. 17.

[127] B. Smith, Geometrical shadowing of a random rough surface, IEEE T. Antenn. Propag., 15(5) (1967) 668-671.

[128] B.J. Lee, Y.B. Chen, Z.M. Zhang, Transmission enhancement through nanoscale metallic slit arrays from the visible to mid-infrared, J. Comput. Theor. Nanos., 5(2) (2008) 201-213.

[129] Y.B. Chen, Z.M. Zhang, Design of tungsten complex gratings for thermophotovoltaic radiators, Opt. Commun., 269(2) (2007) 411-417.

[130] N. Engheta, Circuits with light at nanoscales: optical nanocircuits inspired by metamaterials, Science, 317(5845) (2007) 1698-1702.

[131] A. Sakurai, B. Zhao, Z.M. Zhang, Resonant frequency and bandwidth of metamaterial emitters and absorbers predicted by an RLC circuit model, J. Quant. Spectrosc. Radiat. Transf., 149 (2014) 33-40.

[132] F. Marquier, M. Laroche, R. Carminati, J.J. Greffet, Anisotropic polarized emission of a doped silicon lamellar grating, J. Heat. Transf., 129(1) (2006) 11-16.

[133] B. Zhao, L. Wang, Y. Shuai, Z.M. Zhang, Thermophotovoltaic emitters based on a two-dimensional grating/thin-film nanostructure, Int. J. Heat. Mass. Tran., 67 (2013) 637-645.

[134] J. Chen, P. Wang, Z.M. Zhang, Y. Lu, H. Ming, Coupling between gap plasmon polariton and magnetic polariton in a metallic-dielectric multilayer structure, Phys. Rev. E, 84(2) (2011) 026603.

VITA

PEIYAN YANG

Peiyan Yang was born in Baoding, Hebei Province, China in 1992. He attended Shanghai Jiao Tong University in 2010 and spent two years in Shanghai before going to the University of Hong Kong through a joint-degree program. He graduated with separate Bachelor's degrees from both universities in 2014 majored in mechanical engineering. Afterwards, he has been mentored by Professor Zhuomin Zhang to pursue his Doctoral degree in the George W. Woodruff School of Mechanical Engineering at the Georgia Institute of Technology. His research interests include light scattering in random materials, radiative cooling and plasmonic metamaterials. During his Ph.D., he co-authored 5 journal articles (4 of which is first authored), has given 4 conference presentations and received best technology award in 2018 ASME International Mechanical Engineering Congress & Exposition. He is also a reviewer for *Journal of Quantitative Spectroscopy and Radiative Transfer.*